

SPATIAL REGULATION OF BONE FORMATION IN FUNCTIONAL
ADAPTATION OF CANCELLOUS BONE

A Dissertation

Presented to the Faculty of the Graduate School
of Cornell University

In Partial Fulfillment of the Requirements for the Degree of
Doctor of Philosophy

by

Erin Nicole Cresswell

May 2017

© 2017 Erin Nicole Cresswell

SPATIAL REGULATION OF BONE FORMATION IN FUNCTIONAL ADAPTATION OF CANCELLOUS BONE

Erin Nicole Cresswell, Ph.D.

Cornell University 2017

Bone is a vital component of the musculoskeletal system. The morphology and material properties of bone allow our skeletons to support the loads caused from daily activity. Fractures occur when loads exceed the mechanical capacity of bone. Physical forces are a powerful anabolic stimulus that regulates bone formation, bone geometry, and bone density. Forces on whole bones cause non-uniform tissue strains throughout bone's internal structure. Bone formation is hypothesized to occur at locations of greatest tissue strains.

In this dissertation, I examined the relationship between locations of bone formation and local tissue strains in cancellous bone. The rat tail loading model was used to stimulate mechanically induced bone formation. Finite element modeling was performed to determine local tissue strains. High-resolution three-dimensional images were collected to identify osteocyte lacunae and locations of bone formation. The number of bone formation sites was greater in loaded animals than unloaded controls. The additional bone formation sites were attributed to bone adaptation at locations of greatest tissue strains. However, tissue stress and strain were only modest predictors of locations of bone formation (32-41%), and the ability to predict locations of bone formation was not improved by including the local osteocyte density.

As an example of bones adapted to high intensity loading, I examined bone microstructure in racehorses. Changes in bone morphology have been associated with increased fracture risk in racehorses. I examined the association between bone volume fraction, exercise history, and fracture incidence in the proximal sesamoid bones. Bone morphology was assessed using micro-computed tomography images of the proximal sesamoid bones in racehorses that experienced a proximal sesamoid bone fracture as well as in control racehorses. Greater bone volume fraction was associated with fracture. Additionally, animals with fractures had a history of longer periods of rest interrupted by shorter periods of high speed exercise. The ratio of the total number of weeks with high speed exercise to the number of weeks of rest (work-to-rest ratio) was less in animals that sustained a fracture.

In summary, mechanically induced bone formation occurred at regions of trabecular microarchitecture that experienced the greatest tissue strain. Locations of bone formation were regulated by the local tissue strain, independent of local osteocyte lacunar density. Whole bone density was influenced by exercise, and in the case of racehorses, greater amounts of rest was associated with greater bone volume fraction and fracture risk. Therefore, alteration of the training/racing schedule could regulate bone density and decrease fracture risk.

BIOGRAPHICAL SKETCH

Erin Nicole Litts was born in Columbus, Ohio in 1987. She grew up in the suburbs of Toledo, Ohio and Lansing, Michigan before moving to the rural town of Chardon, Ohio. She graduated Chardon High School in 2006. Erin attended college at Rochester Institute of Technology, completing a Bachelor of Science degree in Mechanical Engineering in 2011. While at RIT, Erin was a member of the RIT Honors Program, Tau Beta Pi, Engineering House, and the RIT Equestrian Team. She held leadership roles within the Equestrian Team serving as English Captain, Treasurer, Vice President, President, and Social Chair. Additionally, she also served the RIT community working as a Resident Advisor, note taker, and tutor. In 2010, she received the Outstanding Undergraduate Award. In addition to school, Erin also gained industry and research experience, working at Impact Technologies LLC in Rochester and at RIT's Fuel Cell and Microfluidics Laboratory.

After graduating from RIT, Erin continued her education at Cornell University, pursuing a doctorate degree in Mechanical Engineering under the advisement of Dr. Christopher Hernandez. In 2014, she married her best friend and changed her name to Erin Nicole Cresswell. While at Cornell, Erin served as Treasurer to the Sibley Graduates in Mechanical and Aerospace Engineering, and received a National Science Foundation Graduate Research Fellowship and American Society for Bone and Mineral Research Young Investigator Travel Award. She also pursued her love for teaching, serving as a Teaching Assistant for Mechanics and Materials, and Statics, and participated in the Center for Teaching Excellence Fellowship program.

I dedicate this work to my parents for their endless support and encouragement.

ACKNOWLEDGMENTS

I thank my advisor, Dr. Christopher Hernandez for his guidance and mentoring in directing my PhD work. I'd like to thank my committee members, Dr. Marjolein van der Meulen and Dr. Larry Bonassar, for their feedback on my work and for encouraging me to think outside the box. I'd like to thank my collaborators Dr. Glen Neibur, Dr. Thomas Metzger, and Dr. Heidi Ressink for expanding the breadth of my research.

I am also grateful for funding from the National Science Foundation that has made this work possible: grant number 1068560 (Hernandez), and NSF GRFP (Cresswell). I also would like to acknowledge the Extreme Science and Engineering Discovery Environment (XSEDE), which supported some of the computational resources required for finite element modeling.

To my lab mates whom have assisted in this work thank you. Matt, I couldn't have gotten the loading model established without your initial efforts, nor through my writing struggle without your edits and comradery. Evgeniy, thank you for taking my calls as I initially struggled to use the serial mill, even if your go to advice was to hit it with a hammer (that did work a lot of the time). Thu, thank you for being a wonderful assistant in every aspect of your lab work. You really did it all, from animal handling and surgery, embedding, sectioning, histology and image processing. I'd also like to thank all my other undergrads for their contributions: Mike Horsfield, Kristen Lee, Adrian Alepuz, Amanda Bouman, and Irene Lin.

To the Weill Animal Care staff, Stephanie Martin, Tim van Deusen, Cheryl Brown, and David Mooneyhan, thank you for always being so great to work with and so diligent looking after the animals. To the Weill Imaging center, Mark Riccio and Teresa Porri, your imaging expertise made my work possible. And to ruler of the Biomechanics Computer Lab, Kirk

Gunsallus, thank you for solving the numerous computer problems that occurred along the way and for sharing your technical knowledge.

I'd especially like to thank the mentors I found along the way in Marcia Sawyer, Judy Thoroughman, Floor Lambers and Maureen Lynch. Your sympathetic ear, understanding, and advice were invaluable.

Last but not least, I would not have survived graduate school without the support from my friends and family. Geoff, I don't think there is another human being willing to tolerate my kind of crazy, but you do it so well. Thank you for being my rock and my confidence when I lose my way. To my Rochester crew, thank you for keeping us in the inner circle. While I don't see you nearly as often as I would like to, whenever we are together it's as if we are all roommates / floor mates again. And to my Ithaca people, thank you for being fun and quirky people who have pushed me to try new things. Your energy has broken up the challenging times and made the long haul of graduate school fun.

TABLE OF CONTENTS

Biographical Sketch -----	v
Acknowledgements -----	vii
Table of Contents -----	ix
List of Figures -----	xi
List of Tables -----	xii
Chapter 1: Introduction -----	1
1.1 Motivation -----	1
1.2 Bone and Mechanical Loading -----	1
1.2.1 Composition and Architecture -----	1
1.2.2 Whole Bone Loading -----	4
1.3 Bone Remodeling -----	5
1.4 Mechanotransduction -----	6
1.5 Identifying Bone Formation -----	8
1.6 Functional Adaptation -----	10
1.7 Study Aims and Importance -----	17
Aim 1: Local Tissue Strain Regulates Bone Formation -----	19
Aim 2: Osteocytes' Role in Mechanotransduction -----	20
Aim 3: Exercise Induced Morphological Changes in Racehorses -----	21
1.8 My Contribution -----	22
Chapter 2: Local Tissue Strain Regulates Bone Formation -----	35
2.1 Introduction -----	35
2.2 Methods -----	37
In vivo Loading and Micro-Computed Tomography -----	37
Finite Element Modeling -----	38
Image Acquisition and Processing -----	40
Spatial Associations between Bone Formation and Mechanical Strain -----	40
Statistics -----	43
2.3 Results -----	43
2.4 Discussion -----	48
2.5 Supplemental Material -----	52
Chapter 3: Osteocytes' Role in Mechanotransduction -----	59
3.1 Introduction -----	59
3.2 Methods -----	62
In vivo Loading and Micro-Computed Tomography -----	62
Distribution of Mechanical Stress and Strain -----	64
Distribution of Osteocyte Lacunae -----	65
Distribution of Locations of Bone Formation -----	66
Spatial Associations between Bone Formation, Mechanical Strain, and	

Osteocyte Density -----	68
3.3 Results -----	69
3.4 Discussion -----	76
3.5 Supplemental Material -----	81
Chapter 4: Exercise Induced Morphological Changes in Racehorses -----	89
4.1 Introduction -----	89
4.2 Methods -----	92
Sample Data -----	92
Image Acquisition and Processing -----	93
History of Training and Racing Exercise -----	95
Statistics -----	96
4.3 Results -----	96
Morphological Changes -----	96
Exercise History -----	98
4.4 Discussion -----	101
Chapter 5: Conclusions and Future Directions -----	110
5.1 Summary -----	110
Aim 1 – Local Tissue Strain Regulates Bone Formation -----	110
Aim 2 – Osteocytes’ Role in Mechanotransduction -----	111
Aim 3 – Exercise Induced Morphological Changes in Racehorses -----	112
Synthesis -----	113
Strength and Limitations -----	115
5.2 Future Directions -----	116
5.2.1 Continued Research Areas -----	117
The Effect of Marrow Pressure on Functional Adaptation -----	117
The Effect of the Lacunar Canalicular Network on Functional Adaptation -----	118
Fracture Toughness in Proximal Sesamoid Bones -----	120
5.2.2 New Research Areas -----	121
Finite Element Modeling of Proximal Sesamoid Bones -----	121
The Effect of Loading Schedule on Bone Formation -----	123
Appendix A: Preliminary Loading Studies Prior to Chapter 2 -----	128
Appendix B: Preliminary Loading Studies Prior to Chapter 3 -----	130
Appendix C: Standard Operating Procedures -----	134
Appendix D: Chapter 2 Additional Data -----	143
Appendix E: Chapter 3 Additional Data -----	150
Appendix F: Chapter 4 Additional Data -----	154

LIST OF FIGURES

1.1 Hierarchical Structure of Bone -----	2
1.2 Osteocytes in Bone -----	8
1.3 Dynamic Histomorphometry -----	10
1.4 Trabecular Alignment to Principal Stress Lines -----	11
1.5 Strain Regulatory Feedback Loop -----	15
1.6 Co-localization of Bone Formation and High Tissue Strain -----	16
1.7 Outline of Study Aims -----	19
2.1 Rat Tail Loading Methods -----	39
2.2 Co-Localization of Bone Formation and High Strain Energy Density -----	41
2.3 Loading Results in 3-month old Rats -----	44
2.4 Number of Bone Formation Sites Near High Strain Energy Density -----	45
2.5 Surface Strain Energy Density Near Bone Formation -----	46
2.6 Probability of Bone Formation -----	47
2.7 Volume Based Spatial Correlations -----	48
2.8 Histogram of SED at Bone Formation and All Trabecular Surfaces -----	53
2.9 Specimen Average SED at Bone Formation and All Trabecular Surfaces -----	54
3.1 Image Acquisition Methods -----	67
3.2 Determining Sites of Mechanically Induced Bone Formation -----	68
3.3 Loading Results in 6-month old Rats -----	71
3.4 Three-Dimensional Probability of Bone Formation -----	73
3.5 Strain Energy Density at Forming Versus Non-Forming Surfaces -----	74
3.6 Distribution of Osteocyte Density and Strain Energy Density -----	75
3.7 Two-Dimensional Probability of Bone Formation -----	82
3.8 Bone Volume Fraction -----	82
4.1 Study Design -----	94
4.2 Micro-CT and Image Processing -----	94
4.3 Bone Volume Fraction -----	97
4.4 Osteophytes -----	98
4.5 Exercise History Influences Bone Volume Fraction -----	99
4.6 Consecutive Weeks of Work and Rest -----	100

LIST OF TABLES

3.1 Multiple Linear Regression of the Probability of Bone Formation -----	74
3.2 Osteocyte Lacunar Densities -----	75
4.1 Thoroughbred racehorse demographics -----	93
4.2 The number of osteophytes observed -----	98

CHAPTER 1

INTRODUCTION

1.1 Motivation

Bone is a vital component of the musculoskeletal system. The bones of the axial skeleton protect the internal organs of the body. The long bones of the appendicular skeleton act as lever arms for muscles to apply forces allowing movement of the body. Movement causes physical loading on the skeleton; however, fractures can occur when the applied loads exceed the mechanical capacity of the whole bone. In humans, age-related fracture results in decreased quality of life, increased mortality rates, and has a substantial financial burden (1). An estimated 4.3 million age-related fractures occurred between 2010 and 2011 in the US (2), and a greater number are anticipated each year (3). Fractures commonly occur in children due to traumatic overload (4), in physically fit individuals such as military recruits (5), and in the elderly population as a result of diseases such as osteoporosis. Fractures are also a challenge for veterinary care. Spontaneous fractures can occur in animals and in the horse are often fatal (6).

1.2 Bone and Mechanical Loading

1.2.1 Composition and Architecture

Bone is a composite material with organic and inorganic components. Mineral is the inorganic component of bone. Collagen and non-collagenous proteins make up

the organic component of bone. Bone tissue is 32% collagen, 45% mineral, and 25% water by volume (7). The degree of mineralization, amount of collagen crosslinking, and water content influence the material properties of bone (8). Additionally, bone is a hierarchical material and the material properties of bone are influenced by the architecture at many length scales from the nanostructure to the macrostructure.

In bone tissue at the nanoscale, collagen and mineral are arranged such that collagen fibers are impregnated with hydroxyapatite crystals (9, 10). Collagen fibers are aligned and arranged to create small sheets (3-7 μm thick) called lamella that form the sub-microstructure of bone (see Figure 1-1) (9). Whole bone also has two distinct macrostructures, cortical and cancellous bone.

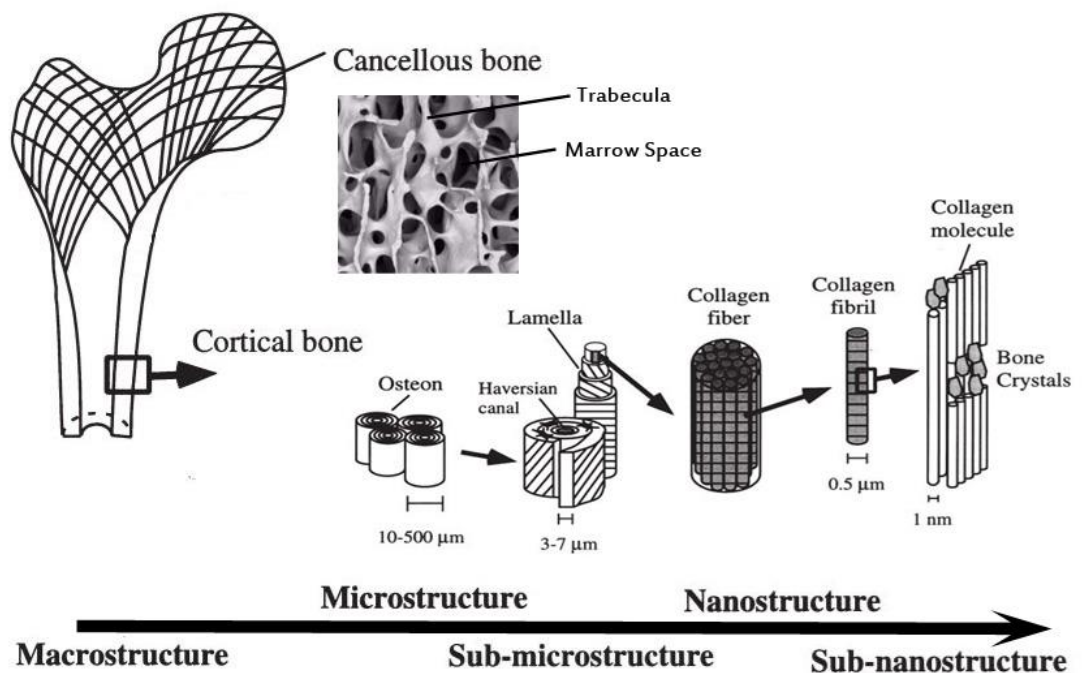


Figure 1-1: Bone is a hierarchical structure with different organization at each length scale. Figure adapted from (9).

Cortical bone is a dense tissue with low porosity (5-10% by volume) present in the diaphysis of long bones and in the outer layer of all bones. Cortical bone is composed of cylindrical osteons and interstitial lamellae. Osteons are composed of concentric rings of lamellae surrounding a Haversian canal. Blood vessels and nerves run through the Haversian canals to supply the bone with nutrients. In long bones, osteons primarily align with the axial direction contributing to the anisotropic material properties of the tissue (11).

Cancellous bone is a highly porous lattice structure (50-90% porosity), found in the distal and proximal ends of long bones near the joints and in the center of irregular bones such as the vertebrae. Cancellous bone is composed of struts known as trabeculae, which can be rod-like or plate-like in shape (see Figure 1-1) (12). Trabeculae are composed of lamellae and hemi-osteons that align to the axis of the strut (10). In terms of its material properties, cancellous bone is transversely isotropic, but the difference between the longitudinal and transverse material properties can vary depending on the arrangement and alignment of trabeculae (13, 14).

The microarchitecture of cancellous bone is a major contributor to cancellous bone material properties. The microarchitecture of cancellous bone is measured in three dimensions using the following measures: bone volume fraction (BV/TV), trabecular thickness (Tb.Th), trabecular separation (Tb.Sp), trabecular number (Tb.N), degree of anisotropy (DA), and structure model index (SMI) (15). Bone volume fraction is defined as the bone volume (BV, the volume of mineralized bone tissue) divided by the tissue volume (TV, the entire cancellous volume including marrow space). Trabecular thickness is measured in three dimensions as the diameter of the

largest sphere that will fit inside the trabecula. Trabecular thickness can be calculated at every location within cancellous bone, however, it is common to report the average trabecular thickness as a descriptor of cancellous bone morphology (16). Trabecular separation is also measured in three dimensions as the largest sphere that can fit inside the marrow spaces, and therefore also can be reported at any location with the average trabecular separation commonly reported. Trabecular number is the inverse of the trabecular separation and is used to indicate how many trabeculae are present and the amount of connectivity in cancellous bone. The degree of anisotropy indicates how highly oriented the trabeculae are within a cancellous bone volume. Structure model index is used to determine if the trabeculae in a cancellous bone region are shaped more rod-like or plate-like (17). (For a full review of bone measurements and nomenclature see (18, 19)).

1.2.2 Whole Bone Loading

Whole bones experience compressive and bending loads that induce tissue strains. Additionally, the geometry and the material properties of whole bones influence the distributions of local strain within the bone tissue.

In long bones, bending causes tensile stresses/strains on one side of the cortex and compressive stresses/strains on the opposite side of the cortex (a distance on the order of centimeters) (20, 21). Strain gauges can be applied to the smooth outer surface of cortical bone, and directly measure tissue strains.

When a whole bone is loaded, forces are distributed through the cortical shell and the cancellous regions in a complicated manner. In cancellous bone, compressive

load applied to the structure result in a variety of loading modes on individual trabeculae. A single trabecula can experience bending causing tensile to compressive stresses/strains across the trabecula (thickness $\sim 100 \mu\text{m}$) (22). Therefore, strain gradients in cancellous bone (distances of $100 \mu\text{m}$) are much more rapid than in cortical bone (over distances of millimeters).

Since cancellous bone is encased in cortical bone, measuring tissue strains directly with strain gauges becomes much more challenging (and would be inaccurate with the sharp gradients in strain). Therefore, finite element models are used to estimate the distribution of stress and strain throughout cancellous bone (for a review on finite element modeling see (23)).

1.3 Bone Remodeling

Bone undergoes turnover through a process called bone remodeling. Bone turnover is extensive; the entire volume of the skeleton is turned over every 7-10 years (24). Bone remodeling is a process of bone resorption followed by bone formation. Remodeling events occur at distinct locations in bone.

Bone remodeling is carried out by two cell types: osteoclasts and osteoblasts. At a site of bone remodeling, osteoclasts arrive to a location on the bone surface and resorb bone creating a resorption cavity. Osteoblasts are then recruited to the site and fill the cavity with new bone matrix. When osteoblasts synthesize new bone, several will become trapped in the new tissue. The trapped osteoblasts differentiate into osteocytes and live embedded in the bone tissue. Osteocytes are believed to play a role in the initiation of bone remodeling. Microcracks in bone tissue can damage the local

osteocyte's cellular processes or cell body, leading to cellular responses that can promote bone resorption and remodeling (25). Therefore, bone remodeling is a mechanism to remove microscopic tissue damage (26, 27). Remodeling also releases calcium stored in bone to be used elsewhere in the body (28).

Alterations in the rate of bone remodeling can influence bone strength and fracture risk. Increased amounts of remodeling results in an increased number of resorption cavities and an associated increase in bone porosity. The reduction in bone volume from resorption cavities can reduce bone strength (27, 29, 30). Alternatively, decreased remodeling allows microdamage to accrue and decreases bone's toughness (27, 31).

In cancellous bone, bone remodeling occurs on the surfaces of trabeculae. The resorption phase of bone remodeling rarely penetrates more than 30 μm from the bone surface. For this reason, the centers of trabeculae are rarely remodeled. Hence, while the total volume of the skeleton undergoes turnover every 7-10 years, there are regions of the bone tissue that are never remodeled and have been present in the body for a longer period of time than bone on the surfaces (22, 32). Given the high surface area to volume ratio in cancellous bone, cancellous bone microstructure is more sensitive to bone remodeling than cortical bone. Additionally, lower volume fractions in cancellous bone also means that remodeling can have a greater influence on apparent tissue strength and toughness.

1.4 Mechanotransduction

Bone can also alter its structure through a process known as bone modeling. Bone modeling involves only bone resorption or only bone formation. Modeling also occurs at distinct locations on the surfaces of bone. Modeling is believed to occur in response to the local tissue strains: locations of low tissue strain are resorbed, while locations of greatest tissue strains recruit osteoblast to form bone.

Osteocytes are the most abundant cell in bone, outnumbering osteoclasts and osteoblasts by more than a factor of 10 (33). Given the locations of osteocytes in bone tissue, they are ideally located to act as sensors of tissue stress/strain. Multiple studies have shown that osteocytes serve a mechanosensory role in bone (34, 35). Osteocytes sense mechanical stimuli through a number of different pathways including interstitial fluid flow over the cell body and between the cell process and the canalicular walls (36, 37), deformation of primary cilia in response to fluid flow (38, 39), and deformation of cell processes connected to extracellular matrix projections (40). In response to mechanical stimuli, osteocytes produce signaling factors that regulate osteoclast and osteoblast differentiation. Osteocytes up regulate prostaglandin E₂, nitric oxide, and integrin growth factor to promote bone formation by osteoblasts (41-44). Osteocytes may also increase local bone formation by down regulating production of osteoblast inhibitors such as sclerostin and DKK1 (45-47). Determining the pathway that is most influential in bone formation is of great interest as therapeutic targets to increase bone formation are desired in clinical settings (48).

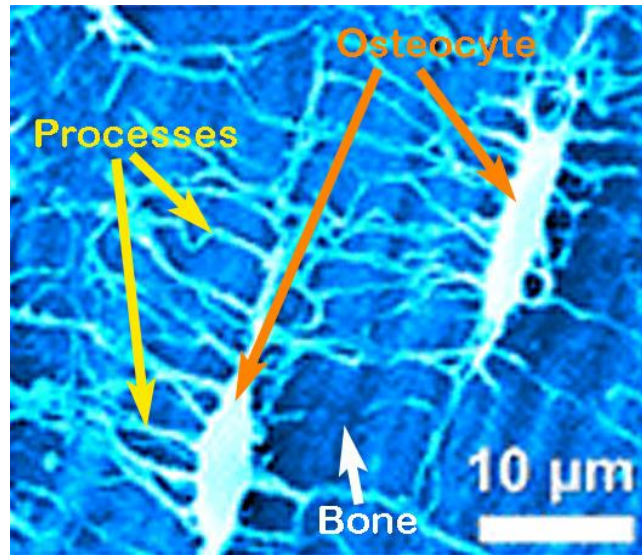


Figure 1-2: Osteocytes are embedded into bone matrix. Osteocytes have many cell processes that extend throughout bone tissue and form connections with other osteocytes. Figure adapted from (49).

1.5 Identifying Bone Formation

The standard technical approach used to measure the amount of bone formation in a specimen is dynamic histomorphometry. To perform dynamic histomorphometry, fluorescent dyes are administered to a live animal or human patient. The fluorescent dyes attach to calcium and become trapped in the new bone at locations where bone was forming at the time of the injection. When bone from a subject is examined, the formation markers appear as fluorescent lines in the bone tissue indicating the locations of bone formation at the time of injection. In dynamic histomorphometry, two markers are applied a few days apart and the distance between the markers in a histology slide is indicative of the rate of bone formation at that location. Under the microscope, bone formation markers can be traced and a series of measurements can be made. Single label surface (sLS) is the measure of bone surfaces

with only one bone formation marker present. Locations within bone with two parallel fluorescent markers are double label surfaces (dLS). Mineralizing surface is calculated as the sum of double labelled surface and one half the single labeled surfaces. To compare across samples, mineralizing surface is normalized by the total bone surface and reported as mineralizing surface per bone surface (MS/BS). Locations with double labelled surfaces make it possible to measure the rate in which new bone was formed. Mineral apposition rate (MAR) is calculated as the distance between the double labels divided by the length of time between administration of the two fluorescent markers. Bone formation rate (BFR) is calculated as the product of mineral apposition rate and mineralizing surface. Although the approach is commonly performed in two dimensional sections, three-dimensional measurements can be made from samples imaged with serial milling. Three-dimensional dynamic bone histomorphometry makes it possible to measure the volume of each individual bone formation event as well as the number of bone formation events in a volume of bone. (For a full review of bone measurements and nomenclature see (19)).

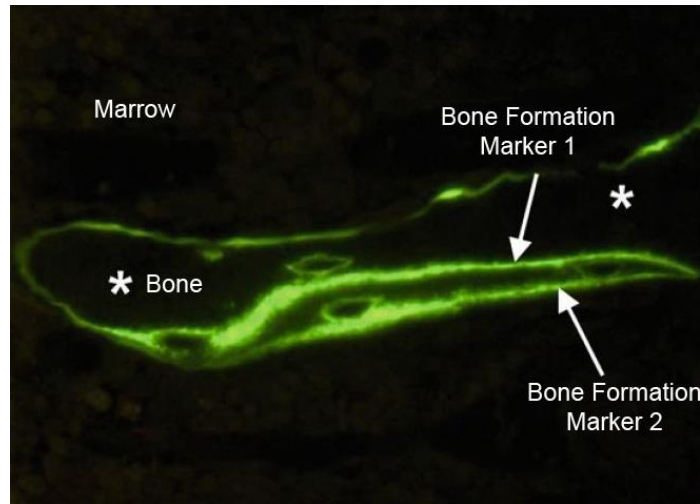


Figure 1-3: Bone formation markers identify the locations of new bone formation. In this image two bone formation markers were administered several days apart. The volume between the two markers is new bone. * indicates the original trabecular bone. Figure adapted from (50).

1.6 Functional Adaptation

In the 1800's, an anatomist named Georg Hermann von Meyer studied the architecture of trabecular bone in the human femoral neck. At the same time, a structural engineer named Karl Culmann designed and analyzed the principal stress directions of the Fairbairn crane. At the gathering of the Society for Natural Science in 1866, the two discussed the similarities in the architecture of trabecular bone and the principal stress lines in the Fairbairn crane (a crane with similar outer shape to the proximal femur) (51). The similarity in patterns between trabeculae and principal stresses inspired a concept commonly referred to as Wolff's Law. Wolff's Law is the idea that the internal structure of bone follows patterns related to internal stress distributions according to mathematical laws (52). Roux additionally proposed that there must be a self-regulating mechanism in bone capable of sensing and responding

to the mechanical environment (53). The concept that the skeleton senses and adapts to the loading it experiences is now known as functional adaptation.

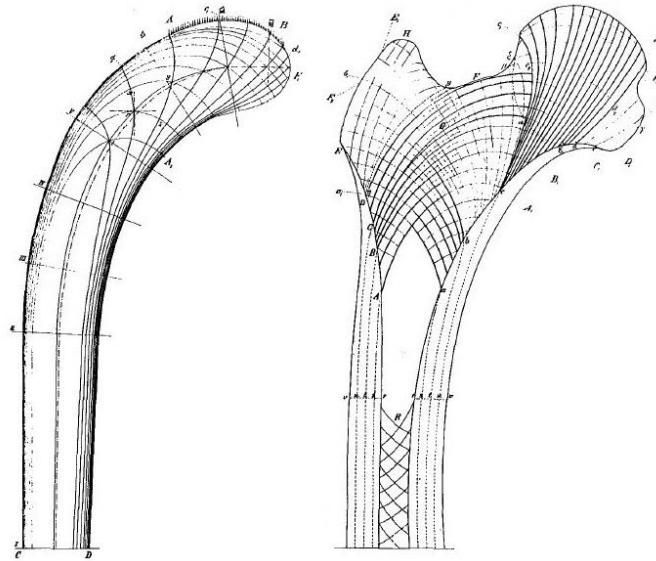


Figure 1-4: Culmann's crane with principal stress trajectories (left) and von Meyer's sketch of trabecular architecture in the human femur (right) inspired the idea that bone structure can adapt to the mechanical environment. Figure adapted from (52).

Functional adaptation has been observed in extreme athletes. In adults, bones that experience increased habitual loading adapt and increase in size and mass. For example, tennis players and professional baseball pitchers have a larger diaphyseal cross-sectional area in their playing (54) or throwing arm (55). Additionally, heavyweight lifters have larger bones than the rest of the population (56). Bone also responds to decreased habitual loading in adults. Patients undergoing prolonged bedrest (57) or astronauts experience prolonged microgravity (58) develop decreased bone mass.

Determining the habitual loading experienced by bone is complex as many different activities or movements could be performed by a human or animal in a day. Carter developed a scalar estimate of the relative amount of habitual loading as a summation of all loading activity which he called the daily stress stimulus. The contribution of each loading activity to the daily stress stimulus depends on the applied stress magnitude and the number of loading cycles (59). The amount of daily stress stimulus influences the net rate of bone resorption or formation. When the daily stress stimulus is greater than normal, the rate of bone formation increases while the rate of bone resorption decreases and causes a net increase in bone formation. Less than normal daily stimulus causes a net bone resorption. At an intermediary level of loading, no net change in bone mass occurs (60).

Many in vivo loading models have been developed to study the response of bone to a controlled mechanical stimulus. Some of the first animal models used surgical techniques to increase stress and strain on a bone and measured functional adaptation as the resulting changes in cross sectional area. Removal of a piece of the ulna increased loads on the radius in pigs (61) and sheep (62) and caused the radius to increase in cross sectional area. To apply a more controlled load, pins were surgically inserted into the proximal and distal metaphysis of long bones and an estimated stress magnitude was applied. Churches et al. found that the cross sectional area of new bone was proportional to the applied stress (63), while Rubin et al found the percent increase in area to be proportional to the applied strain (64). To study the effects of loading uncomplicated by surgical intervention, Turner et al established a noninvasive four point bending model of the rat tibia (65), which was later replaced by a model

that applied an axial compressive load to the rat ulna (20). Studies using these noninvasive models found the largest amount of bone formation to occur at locations of the periosteum that experienced the greatest strains (20, 21). The animal models mentioned so far were used primarily to study functional adaptation of cortical bone.

A number of animal models have established to study functional adaptation in cancellous bone. Goldstein et al. applied load directly to cancellous bone of the dog femur by boring a hole in the cortical shell (66). This model was later adapted to the rabbit (67). Loads directly applied to cancellous bone caused an increase in bone volume fraction and the degree of anisotropy due to increased alignment of trabeculae in the direction of loading (66, 67). Another invasive model for studying cancellous bone is the rat tail loading model (68). In this model, pins are surgically inserted in the caudal seventh and caudal ninth vertebrae. Compressive loads are applied to the caudal eighth vertebrae through the pins in neighboring bones. The bone formation response in cancellous bone was related to load magnitude and number of loading cycles (69). Almost 15 years later, the rat tail loading model was adapted to be used in the mouse (70). Although useful, the rodent tail loading model requires surgery. The mouse tibia loading was established as a means of applying loads to a region of cancellous bone without surgery (71, 72). In this model the knee is supported, and the foot sits in a support that can be moved to apply compressive loading to the tibia. This model has advantages over many of the other animal models, as it has both cancellous and cortical bone, loading is physiologically relevant to the bone, and the contralateral limb can serve as an internal control.

The application of cyclic loads to the bones of live animals leads to increases in bone formation in both cortical (20, 61, 62, 70, 72, 73) and cancellous bone (66-68, 70, 73). In cancellous bone, applied loading improved cancellous microarchitecture by increasing bone volume fraction and trabecular thickness (67, 73-75). The anabolic effect of mechanical loading is influenced by peak strain (63, 64), strain rate (76), load frequency (77), rest insertion (78-80) and number of loading cycles (81).

Whole bone mass and architecture is clearly affected by mechanical loading as has been shown by animal models. Loading of whole bones causes a distribution of tissue stress and strain throughout bone tissue. Strain gages attached to the periosteal surfaces of live animals and humans have provided surprising information about the tissue strains experienced during locomotion. Interestingly, the recorded strains were common across many different species. For example, trotting induced $-2800 \mu\epsilon$ on the horse radius, running caused $-2350 \mu\epsilon$ on the turkey tibia, and $-2200 \mu\epsilon$ was measured in the femur of trotting sheep. In a survey of many more animals, tissue strains fell in the range of $2000-3000\mu\epsilon$ in compression for normal exertion (82). The observation that the maximum tissue strain in bone was similar in many animals led to the suggestion that there is a set point, or ideal strain environment in bone. If an ideal strain exists then bone tissue must be able to regulate the tissue strain. A process for regulating strain was proposed (Figure 1-5) (82). When habitual loading on a bone is increased the tissue strains also increase. Bone responds to the increased strains by forming more tissue which reduces the strains experienced by the bone tissue during subsequent loading. When habitual loading on a bone is reduced, tissue strains drop

and bone resorption occurs. The remaining bone tissue must carry more load and therefore tissue strains will increase back to the ideal strain environment.

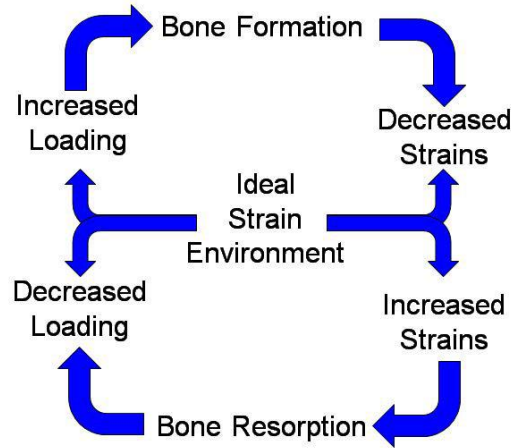


Figure 1-5: A negative feedback loop controls the tissue strains in bone.

As strains are not uniform in bone, adaptation in the form of bone resorption or bone formation should occur at specific locations in bone. Bone resorption should occur at locations with lesser tissue strains while bone formation should occur at locations with greater tissue strains. Bending of the rat ulna caused large amounts of bone formation at the locations of greatest compressive and tensile strains with little to no bone formation near the neutral surface where strains are lowest (20, 21, 83). Therefore, to the best of our knowledge, functional adaptation on the periosteal surfaces of cortical bone does occur based on the local tissue strains.

Less is known about the adaptation of bone to the local stresses and strains in cancellous bone on individual trabeculae. The rodent tail loading model has been used to study the relationship between locations of bone formation and the local tissue strain. The rodent tail loading model is advantageous because the whole bone is relatively small which reduces the computational expense of models used to determine

the distribution of local tissue strain. Additionally, the assumption that the boundary conditions applied to the vertebrae are a uniform across the surface is reasonable and again provides confidence in the ability to accurately determine the distribution of local tissue strain. Studies of the mouse caudal vertebrae, have used whole bone finite element models to determine local tissue strains represented as strain energy density (84). After four weeks of loading tissue strain energy density was higher at locations of bone formation. However, the ability of local tissue strain energy density to predict locations of bone formation was limited and did not exceed 47% predictive capability, even at the locations of greatest strain energy density (84).

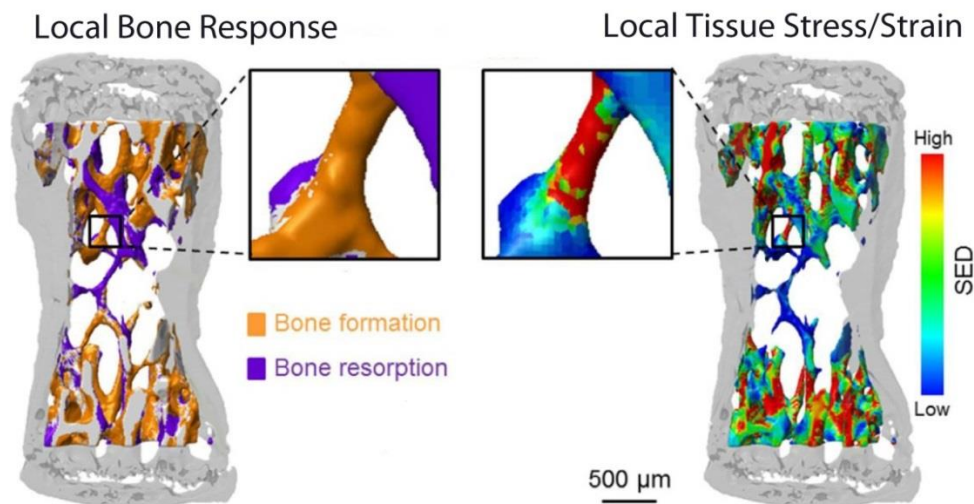


Figure 1-6: (Left) Bone formation and bone resorption are assessed from time lapsed in vivo micro-CT imaging. Whole bone finite element models determined the strain energy density (Right). A highly-strained trabecula was a site of bone formation. Figure adapted from (84).

Osteocytes are believed to be the primary cells responsible for detecting local tissue stress and strain and signaling osteoclasts and osteoblasts. Osteocytes are embedded in bone tissue making them ideal sensors of mechanical stress and strain

(34, 35). In vitro investigations have shown that osteocytes can sense bone tissue strains and interstitial fluid flow (36-40). In response to mechanical stimuli, osteocytes produce signaling factors that regulate osteoblasts (41-47). Since osteocytes respond to mechanical stimuli, regions of bone tissue with greater osteocyte density are expected to be more sensitive to increases in tissue stress and strain. Consistent with this idea, computational models simulating bone mechanoadaptation that have included osteocyte distribution successfully generate trabecular bone-like structures (85-87).

Prior to this dissertation, the only in vivo evidence in cancellous bone that bone formed at the locations of greatest tissue strains were studies in the rodent tail loading model over a long period of loading (4 weeks) (84). However, bone responds to loading at much shorter time scales altering gene expression 3 and 24 hours after mechanical loading (88), and increasing protein secretion at 72 hours after mechanical loading (89). Therefore, evaluating the short-term adaptation of bone to mechanical stimuli is necessary for understanding mechanotransduction. Identifying signaling pathways that are most influential in bone formation could help identify the most attractive therapeutic targets (48).

1.7 Study Aims and Importance

Many in vivo loading experiments have expanded our understanding of functional adaptation in bone. Bone formation has been shown to occur at locations of greatest tissue strain in cortical bone (20, 21, 83). Recent investigations into functional adaptation in cancellous bone also suggested that the tissue strains (represented by strain energy density) are greater at locations that led to bone formation (84).

However, the spatial association between bone formation and local tissue strain energy density in cancellous bone has only been investigated over long periods of adaptation (4 weeks)(84), yet bone responds to loading at much shorter time scales altering the gene expression in a matter of hours (88), and increasing protein secretion and forming osteoid in a matter of days (89). The spatial association between bone formation and local tissue mechanical stimuli in cancellous bone has not been investigated at shorter time scales. Therefore, evaluating the short-term adaptation of bone to mechanical stimuli is necessary for identifying the pathways that are most influential in bone functional adaptation and therefore attractive for therapeutic targets (48). Prior to this dissertation, the spatial association of bone formation and local tissue mechanical stimuli after short-term loading was not known in cancellous bone. Osteocytes are the primary cells responsible for sensing mechanical stimuli in bone and regulating the formation and resorption of bone by osteoblasts and osteoclasts (35, 41-47). Locations within bone that have greater osteocyte density should therefore be more sensitive to the mechanical environment in bone tissue. By incorporating the spatial distribution of osteocytes and local mechanical stimuli on locations of bone formation, the mechanotransduction pathways can be investigated in further detail.

Exercise has also been associated with functional adaptation. Racehorses have been a useful model of high impact exercise. Exercise associated with race training of horses has been shown to cause an increase in bone density of many bones in the limbs such as the proximal sesamoid bones, third metacarpal, third carpal, and radial carpal bones (90-94). Recently, increases in bone volume fraction in the proximal sesamoid bones have been associated with spontaneous fracture (95-97). Therefore, in

this dissertation I explored details of exercise history associated with changes in bone volume fraction. Determining the influence of training and racing exercise and schedules on bone volume fraction could inform future training practices to decrease fracture risk in racehorses.

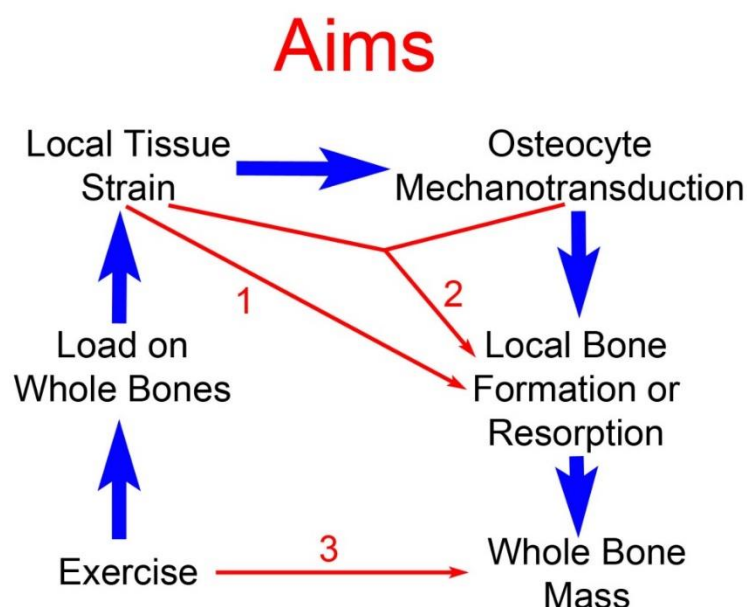


Figure 1-7: Mechanics of the whole bone influences mechanics of smaller length scales. Signaling works up the length scales to influence tissue adaptation. In this dissertation, aim 1 studies the effect of tissue mechanics on locations of tissue adaptation. Aim 2 studies tissue mechanics combined with the osteocyte density to determine the effect on tissue adaptation. Aim 3 evaluates the role of exercise history on regulating bone volume fraction. Figure adapted from (98).

1.7.1 Aim 1- Local Tissue Strain Regulates Bone Formation

While in vivo mechanical loading has been shown to increase the density of cancellous bone (67, 73-75, 99), theoretical models suggest that tissue level changes result from adaptation at the scale of individual trabeculae (100). Bone formation after weeks of adaptation has been shown to form at locations of greater tissue stress/strain (84). However, it is unclear if bone formation preferentially forms at locations of

greatest tissue stress/strain immediately following an acute mechanical stimulus. It is also unclear if the locations of bone formation can be predicted from the local tissue stress/strain after an acute mechanical stimulus. In this aim, locations of bone formation one week following mechanical loading were determined. Three bouts of cyclic loading (300 cycles/day on 3 consecutive days) were applied to caudal vertebrae of female rats (n=7). Bone formation was determined using three-dimensional images of fluorescent markers of bone formation (0.7 x 0.7 x 5.0 μ m) and local tissue stress/strain was determined using high-resolution finite element models. The mineralizing surface, number of bone formation sites, and size of formation sites were assessed in three-dimensions. The spatial relationship between bone formation and local tissue stress/strain was determined (101).

1.7.2 Aim 2 – Osteocytes' Role in Mechanotransduction

Osteocytes play an integral role in bone functional adaptation by sensing mechanical stimuli and responding through the release of signaling factors that regulate bone formation (35, 41-47). The mechanosensory role of osteocytes suggests that bone functional adaptation is influenced by osteocyte populations i.e. regions of bone tissue with greater osteocyte populations may be more responsive to mechanical stimuli (85). The purpose of this aim was to determine the effects of the osteocyte population on bone functional adaptation. Mechanical loads were applied to the 8th caudal vertebra of skeletally mature (6 months of age) female rats (n=8 loaded, n=8 sham controls). The distribution of tissue stress and strain within cancellous bone was determined using high resolution finite element models, the osteocyte distribution was

determined using nano-computed tomography, and locations of bone formation were determined using three-dimensional images of fluorescent bone formation markers. Bone formation markers were administered prior to and after loading making it possible to identify background bone formation, from mechanically induced bone formation. Spatial correlation techniques were used determine relationships between site of mechanically induced bone formation and local tissue stress/strain and local osteocyte density.

1.7.3 Aim 3 - Exercise Induced Morphological Changes in Racehorses

Fracture of the proximal sesamoid bones is the most common musculoskeletal injury leading to death in racehorses (102-104). Determining bone morphology that predisposes a racehorse to fracture of the proximal sesamoid bone would be useful for assessing fracture risk. Morphological changes in the proximal sesamoid bones of racehorses that sustain a fracture have been observed and compared to racehorses that do not fracture the proximal sesamoid bones. The most significant morphological change observed has been increased bone density (95-97). Aspects of racing and training history have also been associated with increased fracture risk (105-107). However, differences in racing and training history leading to increased bone density and then increased fracture risk is not understood. Determining how the pathology develops could lead to effective preventive interventions. Therefore, I hypothesized that more rigorous racing and training histories, with larger total distances run would be associated with increased bone density and fracture. In this study, I examined the proximal sesamoid bones of Thoroughbred racehorses that suffered a proximal

sesamoid bone fracture in one or both sesamoid bones of a front limb, and compared them to sex and age matched controls (n=4 animals per group). Micro-computed tomography images of all proximal sesamoid bones (voxel size 50 x 50 x 50 μ m) were used to determine bone volume fraction and tissue mineral density. High speed exercise during training and racing was recorded and differences in exercise history between groups were determined. Morphological changes were correlated to exercise history to determine if exercise routines could be modified to control bone volume fraction, and therefore, mediate fracture risk in racehorses.

1.8 My Contributions

Aim 1 was published in the Journal of Biomechanics and was presented at the 2014 annual meeting of the Orthopaedic Research Society.

- Cresswell, E.N.; Goff, M.G.; Nguyen, T.M.; Lee, W.X.; Hernandez, C.J. Spatial Relationships between Bone Formation and Mechanical Stress within Cancellous Bone. *Journal of Biomechanics* 49(2):222-228, 2016.
- Litts, E.N.; Goff, M.G.; Nguyen, T.M.; Lee, W.X.; Hernandez, C.J. Tissue-level Mechanotransduction in Cancellous Bone Submitted to Mechanical Overload in Vivo. Podium Presentation at the Orthopaedic Research Society Conference, 2015.

Results from aim 2 were presented during the plenary poster session at the American Society of Bone and Mineral Research annual meeting in 2016 and a manuscript is under preparation for submission to BONE.

- Cresswell, E.N.; Nguyen, T.M.; Horsfield, M.W.; Alepuz, A.J.; Metzger, T.A.; Niebur, G.L.; Hernandez, C.J. Mechanically Induced Bone Formation is not Sensitive to Local Osteocyte Density. BONE.
- Cresswell, E.N.; Nguyen, T.M.; Horsfield, M.W.; Alepuz, A.J.; Metzger, T.A.; Niebur, G.L.; Hernandez, C.J. Osteocyte Distribution does not Influence Locations of Mechanically Induced Bone Formation in Cancellous Bone. Plenary Poster at the American Society of Bone and Mineral Research Conference, 2016.

Results from aim 3 will be presented at the 2017 annual meeting of the Orthopaedic Research Society. Aim 3 as presented in this dissertation represents a preliminary study. After increasing the sample size, a manuscript for submission to the Equine Veterinarian Journal will be prepared.

- Cresswell, E.N.; McDonough, S.P.; Palmer, S.E.; Hernandez, C.J.; Reesink, H.L. Catastrophic Failure in Proximal Sesamoid Bones of Racehorses is Associated with Increased Bone Density. Poster Presentation at the Orthopaedic Research Society Conference, 2017.

During my doctoral studies, I also contributed to a review article explaining the clinical relevance of finite element models in determining bone strength. Additionally, I contributed data to another publication that establishes spatial correlation techniques as well as validates finite element models of rat caudal vertebrae.

- Hernandez CJ, Cresswell EN. Understanding Bone Strength from Finite Element Models: Concepts for Non-engineers. *Clinical Reviews in Bone and Mineral Metabolism*. 2016;14(3):161-6.
- Goff, M.G.; Chang, K.L.; Litts, E.N.; Hernandez, C.J. The effects of misalignment during in vivo loading of bone: techniques to detect the proximity of objects in three-dimensional models. *Journal of Biomechanics* 47(12):3156-3161, 2014.

REFERENCES

1. Johnell O, Kanis JA. An estimate of the worldwide prevalence and disability associated with osteoporotic fractures. *Osteoporos Int.* 2006;17(12):1726-33.
2. Watkins-Castillo SI, Wright NC. Prevalence of Fragility Fractures. Rosemont, IL: United States Bone and Joint Initiative; 2014 [cited 2016 12/10/2016]; Third Edition. Available from: <http://www.boneandjointburden.org/2014-report/vb1/prevalence-fragility-fractures>.
3. Burge R, Dawson-Hughes B, Solomon DH, Wong JB, King A, Tosteson A. Incidence and economic burden of osteoporosis-related fractures in the United States, 2005-2025. *J Bone Miner Res.* 2007;22(3):465-75.
4. Alffram P-A, Bauer GCH. Epidemiology of Fractures of the Forearm. A Biomechanical Investigation of Bone Strength. 1962;44(1):105-14.
5. Milgrom C, Giladi M, Stein M, Kashtan H, Margulies J, Chisin R, et al. Stress fractures in military recruits. A prospective study showing an unusually high incidence. *Journal of Bone & Joint Surgery, British Volume.* 1985;67-B(5):732-5.
6. Parkin TD. Epidemiology of racetrack injuries in racehorses. *Vet Clin North Am Equine Pract.* 2008;24:1.
7. Robinson RA, Elliott SR. The Water Content of Bone: The Mass of Water, Inorganic Crystals, Organic Matrin, and CO₂ Space Components in a Unit Volume of Dog Bone. *The Journal of Bone and Joint Surgery.* 1957;39(1):167-88.
8. Currey JD. The mechanical consequences of variation in the mineral content of bone. *Journal of Biomechanics.* 1969;2(1):1-11.
9. Rho JY, Kuhn-Spearing L, Zioupos P. Mechanical properties and the hierarchical structure of bone. *Medical Engineering and Physics.* 1998;20(2):92-102.
10. Cowin S, editor. *Bone Mechanics Handbook.* 2 ed. Boca Raton: CRC Press; 2001.
11. Dempster WT, Liddicoat RT. Compact bone as a non-isotropic material. *American Journal of Anatomy.* 1952;91(3):331-62.

12. Currey JD. *Bones: Structure and Mechanics*. Princeton, NJ, USA: Princeton University Press; 2002.
13. Williams JL, Lewis JL. Properties and an anisotropic model of cancellous bone from the proximal tibial epiphysis. *Journal of Biomedical Engineering*. 1982;104:50-6.
14. Townsend PR, Raux P, Rose RM, Miegel RE, Radin EL. The distribution and anisotropy of the stiffness of cancellous bone in the human patella. *Journal of Biomechanics*. 1975;8(6):363-7.
15. Odgaard A. Three-dimensional methods for quantification of cancellous bone architecture. *Bone*. 1997;20(4):315-28.
16. Bouxsein ML, Boyd SK, Christiansen BA, Guldberg RE, Jepsen KJ, Muller R. Guidelines for assessment of bone microstructure in rodents using micro-computed tomography. *J Bone Miner Res*. 2010;25(7):1468-86.
17. Hildebrand T, Ruegsegger P. Quantification of Bone Microarchitecture with the Structure Model Index. *Comput Methods Biomech Biomed Engin*. 1997;1(1):15-23.
18. Parfitt AM, Drezner MK, Glorieux FH, Kanis JA, Malluche H, Meunier PJ, et al. Bone histomorphometry: standardization of nomenclature, symbols, and units. Report of the ASBMR Histomorphometry Nomenclature Committee. *J Bone Miner Res*. 1987;2(6):595-610.
19. Dempster DW, Compston JE, Drezner MK, Glorieux FH, Kanis JA, Malluche H, et al. Standardized nomenclature, symbols, and units for bone histomorphometry: A 2012 update of the report of the ASBMR Histomorphometry Nomenclature Committee. *Journal of bone and mineral research : the official journal of the American Society for Bone and Mineral Research*. 2013;28(1):2-17.
20. Torrance AG, Mosley JR, Suswillo RF, Lanyon LE. Noninvasive loading of the rat ulna in vivo induces a strain-related modeling response uncomplicated by trauma or periosteal pressure. *Calcified Tissue International*. 1994;54(3):241-7.
21. Kotha SP, Hsieh YF, Strigel RM, Muller R, Silva MJ. Experimental and finite element analysis of the rat ulnar loading model-correlations between strain and bone formation following fatigue loading. *Journal of Biomechanics*. 2004;37(4):541-8.

22. Mulder L, Koolstra JH, den Toonder JMJ, van Eijden TMGJ. Intratrabecular distribution of tissue stiffness and mineralization in developing trabecular bone. *Bone*. 2007;41(2):256-65.
23. Hernandez CJ, Cresswell EN. Understanding Bone Strength from Finite Element Models: Concepts for Non-engineers. *Clinical Reviews in Bone and Mineral Metabolism*. 2016;14(3):161-6.
24. Manolagas SC. Birth and Death of Bone Cells: Basic Regulatory Mechanisms and Implications for the Pathogenesis and Treatment of Osteoporosis. *Endocrine Reviews*. 2000;21(2):115-37.
25. Verborgt O, Gibson GJ, Schaffler MB. Loss of osteocyte integrity in association with microdamage and bone remodeling after fatigue in vivo. *J Bone Miner Res*. 2000;15(1):60-7.
26. Henriksen K, Neutzsky-Wulff AV, Bonewald LF, Karsdal MA. Local communication on and within bone controls bone remodeling. *Bone*. 2009;44(6):1026-33.
27. Schaffler MB. Role of bone turnover in microdamage. *Osteoporos Int*. 2003;14 Suppl 5:S73-7; discussion S7-80.
28. Hadjidakis DJ, Androulakis II. Bone Remodeling. *Annals of the New York Academy of Sciences*. 2006;1092(1):385-96.
29. Schaffler MB, Radin EL, Burr DB. Long-term fatigue behavior of compact bone at low strain magnitude and rate. *Bone*. 1990;11(5):321-6.
30. Martin B. A theory of fatigue damage accumulation and repair in cortical bone. *Journal of Orthopaedic Research*. 1992;10(6):818-25.
31. Mashiba T, Hirano T, Turner CH, Forwood MR, Johnston CC, Burr DB. Suppressed bone turnover by bisphosphonates increases microdamage accumulation and reduces some biomechanical properties in dog rib. *J Bone Miner Res*. 2000;15(4):613-20.
32. Burket JC, Brooks DJ, MacLeay JM, Baker SP, Boskey AL, van der Meulen MCH. Variations in nanomechanical properties and tissue composition within trabeculae from an ovine model of osteoporosis and treatment. *Bone*. 2013;52(1):326-36.
33. Parfitt AM, editor. *Bone-forming cells in clinical conditions*. Boca Raton, FL: Telford Press and CRC Press; 1990.

34. Schaffler MB, Kennedy OD. Osteocyte signaling in bone. *Current osteoporosis reports*. 2012;10(2):118-25.
35. Bonewald LF. The amazing osteocyte. *Journal of Bone and Mineral Research*. 2011;26(2):229-38.
36. Weinbaum S, Cowin SC, Zeng Y. A model for the excitation of osteocytes by mechanical loading-induced bone fluid shear stresses. *Journal of Biomechanics*. 1994;27(3):339-60.
37. You J, Yellowley CE, Donahue HJ, Zhang Y, Chen Q, Jacobs CR. Substrate deformation levels associated with routine physical activity are less stimulatory to bone cells relative to load-induced oscillatory fluid flow. *Journal of Biomechanical Engineering*. 2000;122:387-93.
38. Temiyasathit S, Jacobs CR. The osteocyte primary cilium and its role in bone mechanotransduction. *Annals of the New York Academy of Sciences*. 2010;1192:422-8.
39. Coughlin TR, Voisin M, Schaffler MB, Niebur GL, McNamara LM. Primary Cilia Exist in a Small Fraction of Cells in Trabecular Bone and Marrow. *Calcified Tissue International*. 2015;96(1):65-72.
40. McNamara LM, Majeska RJ, Weinbaum S, Friedrich V, Schaffler MB. Attachment of Osteocyte Cell Processes to the Bone Matrix. *The Anatomical Record: Advances in Integrative Anatomy and Evolutionary Biology*. 2009;292(3):355-63.
41. McGarry JG, Klein-Nulend, Jenneke, Prendergast, Patrick J. The effect of cytoskeletal disruption on pulsatile fluid flow-induced nitric oxide and prostaglandin E2 release in osteocytes and osteoblasts. *Biochemical and Biophysical Research Communications*. 2005;330(1):341-8.
42. Ponik SM, Triplett, Jason W., Pavalko, Fredrick M. Osteoblasts and osteocytes respond differently to oscillatory and unidirectional fluid flow profiles. *Journal of Cellular Biochemistry*. 2007;100(3):794-807.
43. Vatsa A, Smit TH, Klein-Nulend J. Extracellular NO signalling from a mechanically stimulated osteocyte. *J Biomech*. 2007;40, Supplement 1:S89-S95.
44. Bacabac RG, Mizuno, Daisuke, Schmidt, Christoph F., MacKintosh, Fred C., Van Loon, Jack J. W. A., Klein-Nulend, Jenneke, Smit, Theo H. Round versus flat: Bone cell morphology, elasticity, and mechanosensing. *Journal of Biomechanics*. 2008;41(7):1590-8.

45. Li X, Zhange, Y., Kang, H., Lui, W., Lui, P., Zhang, J., Harris, S. E., Wu, D. Sclerostin Binds to LRP5/6 and Antagonizes Canonical Wnt Signaling. *Journal of Biological Chemistry*. 2005;280:19883-7.
46. Li J, Sarosi, Ildiko, Cattley, Russell C., Pretorius, James, Asuncion, Frank, Grisanti, Mario, Morony, Sean, Adamu, Stephen, Geng, Zhaopo, Qiu, Wanrong, Kostenuik, Paul, Lacey, David L., Simonet, W. Scott, Bolon, Brad, Qian, Xueming, Shalhoub, Victoria, Ominsky, Michael S., Zhu Ke, Hua, Li, Xiaodong, Richards, William G. Dkk1-mediated inhibition of Wnt signaling in bone results in osteopenia. *Bone*. 2006;39(4):754-66.
47. Robling AG, Niziolek, P. J., Baldrige, L. A., Condon, K. W., Allen, M. R., Alam, I., Mantila, S. M., Gluhak-Heinrich, J., Bellido, T. M., Harris, S. E., Turner, C. H. Mechanical Stimulation of Bone in vivo Reduces Osteocyte Expression of Sost/Sclerostin. *Journal of Biological Chemistry*. 2008;283:5866-75.
48. Plotkin LI, Bellido T. Osteocytic signalling pathways as therapeutic targets for bone fragility. *Nat Rev Endocrinol*. 2016;12(10):593-605.
49. Milovanovic P, Zimmermann EA, Hahn M, Djonic D, Püschel K, Djuric M, et al. Osteocytic Canalicular Networks: Morphological Implications for Altered Mechanosensitivity. *ACS Nano*. 2013;7(9):7542-51.
50. Erben RG. Bone-labeling techniques. In: An YH, Martin KL, editors. *Handbook of Histology Methods for Bone and Cartilage*. Totowa, NJ, USA: Humana Press; 2003. p. 99-117.
51. Skedros JG, Brand RA. Biographical Sketch. *Clinical Orthopaedics and Related Research* 2011;469(11):3072-6.
52. Cowin SC. Wolff's Law of trabecular architecture at remodeling equilibrium. *Journal of Biomechanical Engineering*. 1986;108:83-8.
53. Roesler H. The History of some Fundamental Concepts in Bone Biomechanics. *Journal of Biomechanics*. 1987;20(11):1025-34.
54. Jones HH, Priest JD, Hayes WC, Tichenor CC, Nagel DA. Humeral hypertrophy in response to exercise. *J Bone Joint Surg*. 1977;59:204-8.
55. King J, Breslford H, Tullos H. Analysis of the Pitching Arm of the Professional Baseball Pitcher. *Clin Orthop Relat Res*. 1969;67:116-23.

56. Karlsson MK, Johnell O, Obrant KJ. Bone mineral density in weight lifters. *Calcified Tissue International*. 1993;52(3):212-5.
57. Donaldson CL, Hulley SB, Vogel JM, Hattner RS, Bayers JH, McMillan DE. Effect of Prolonged Bed Rest on Bone Mineral. *Metabolism*. 1970;19(12):1071-84.
58. Vico L, Collet P, Guignandon A, Lafage-Proust MH, Thomas T, Rehalia M, et al. Effects of long-term microgravity exposure on cancellous and cortical weight-bearing bones of cosmonauts. *The Lancet*. 2000;355:1607-11.
59. Fyhrie DP, Carter DR. A unifying principle relating stress to trabecular bone morphology. *J Orthop Res*. 1986;4(3):304-17.
60. Carter DR. The Relationship Between in vivo Strains and Cortical Remodeling. *Crit Rev Biomed Eng*. 1982;8(1):1-28.
61. Goodship AE, Lanyon LE, McFie H. Functional adaptation of bone to increased stress. An experimental study. *The Journal of Bone and Joint Surgery*. 1979;61(4):539-46.
62. Lanyon LE, Goodship AE, Pye C, McFie H. Mechanically adaptive bone remodeling: a quantitative study on functional adaptation in the radius following ulna osteotomy in sheep. *Journal of Biomechanics*. 1982;15:141-54.
63. Churches AEH, C. R. . Functional Adaptation of Bone in Response to Sinusoidally Varying Controlled Compressive Loading of the Ovine Metacarpus. *Clinical Orthopaedics & Related Research*. 1982;168:265-80.
64. Rubin CT, Lanyon LE. Regulation of bone mass by mechanical strain magnitude. *Calcif Tissue Int*. 1985;37(4):411-7.
65. Turner CH, Akhter MP, Raab DM, Kimmel DB, Recker RR. A noninvasive, in vivo model for studying strain adaptive bone modeling. *Bone*. 1991;12(2):73-9.
66. Goldstein SA, Matthews LS, Kuhn JL, Hollister SJ. Trabecular bone remodeling: an experimental model. *Journal of Biomechanics*. 1991;1(135):135-50.
67. van der Meulen MC, Morgan TG, Yang X, Baldini TH, Myers ER, Wright TM, et al. Cancellous bone adaptation to in vivo loading in a rabbit model. *Bone*. 2006;38(6):871-7.

68. Chambers TJ, Evans M, Gardner TN, Turner-Smith A, Chow JW. Induction of bone formation in rat tail vertebrae by mechanical loading. *Bone Miner.* 1993;20(2):167-78.
69. Chow JW, Jagger CJ, Chambers TJ. Characterization of osteogenic response to mechanical stimulation in cancellous bone of rat caudal vertebrae. *American Journal of Physiology.* 1993;265(2 Pt 1):E340-7.
70. Webster DJ, Morley PL, van Lenthe GH, Muller R. A novel in vivo mouse model for mechanically stimulated bone adaptation--a combined experimental and computational validation study. *Computer Methods in Biomechanics and Biomedical Engineering.* 2008;11(5):435-41.
71. Fritton JC, Meyers ER, van der Meulen MC, Bostrom MP, Wright TM, editors. Validation of a loading apparatus: Characterization of murine tibial surface strains in vivo. *Trans ORS*; 2001; San Francisco, CA, USA.
72. De Souza RL, Matsuura M, Eckstein F, Rawlinson SC, Lanyon LE, Pitsillides AA. Non-invasive axial loading of mouse tibiae increases cortical bone formation and modifies trabecular organization: a new model to study cortical and cancellous compartments in a single loaded element. *Bone.* 2005;37(6):810-8.
73. Fritton JC, Myers ER, Wright TM, van der Meulen MC. Loading induces site-specific increases in mineral content assessed by microcomputed tomography of the mouse tibia. *Bone.* 2005;36(6):1030-8.
74. Lambers FM, Schulte FA, Kuhn G, Webster DJ, Muller R. Mouse tail vertebrae adapt to cyclic mechanical loading by increasing bone formation rate and decreasing bone resorption rate as shown by time-lapsed in vivo imaging of dynamic bone morphometry. *Bone.* 2011;49(6):1340-50.
75. Webster D, Wasserman E, Ehrbar M, Weber F, Bab I, Muller R. Mechanical loading of mouse caudal vertebrae increases trabecular and cortical bone mass-dependence on dose and genotype. *Biomechanics and Modeling in Mechanobiology.* 2010.
76. Turner CH, Owan I, Takano Y. Mechanotransduction in bone: role of strain rate. *Am J Physiol.* 1995;269(3 Pt 1):E438-42.
77. Hsieh Y, Turner CH. Effects of loading frequency on mechanically induced bone formation. *Journal of Bone and Mineral Research.* 2001;16(5):918-24.

78. Robling AG, Burr DB, Turner CH. Partitioning a Daily Mechanical Stimulus into Discrete Loading Bouts Improves the Osteogenic Response to Loading. *Journal of Bone and Mineral Research*. 2000;15(8):1596-602.
79. Saxon LK, Robling AG, Alam I, Turner CH. Mechanosensitivity of the rat skeleton decreases after a long period of loading, but is improved with time off. *Bone*. 2005;36(3):454-64.
80. Robling AG, Hinant FM, Burr DB, Turner CH. Improved Bone Structure and Strength After Long-Term Mechanical Loading Is Greatest if Loading Is Separated Into Short Bouts. *Journal of Bone and Mineral Research*. 2002;17(8):1545-54.
81. Rubin CT, Lanyon LE. Regulation of bone formation by applied dynamic loads. *Journal of Bone and Joint Surgery American Volume*. 1984;66-A:397-402.
82. Rubin CT, Lanyon LE. Dynamic Strain Similarities In Vertebrates; An Alternative to Allometric Limb Bone Scaling. *Journal of Theoretical Biology*. 1984;107(2):321-7.
83. Webster D, Wirth A, van Lenthe GH, Muller R. Experimental and finite element analysis of the mouse caudal vertebrae loading model: prediction of cortical and trabecular bone adaptation. *Biomechanics and Modeling in Mechanobiology*. 2012;11(1-2):221-30.
84. Schulte FA, Ruffoni, D., Lambers, F. M., Christen, D., Webster, D. J., Kuhn, G., Muller, R. Local mechanical stimuli regulate bone formation and resorption in mice at the tissue level. *PloS one*. 2013;8(4):e62172.
85. Huiskes R, Ruimerman R, van Lenthe GH, Janssen JD. Effects of mechanical forces on maintenance and adaptation of form in trabecular bone. *Nature*. 2000;405(6787):704-6.
86. Mullender MG, Huiskes R, Weinans H. A physiological approach to the simulation of bone remodeling as a self-organizational control process. *Journal of Biomechanics*. 1994;27(11):1389-94.
87. Mullender MG, Huiskes R. Proposal for the regulatory mechanism of Wolff's law. *Journal of Orthopaedic Research*. 1995;13(4):503-12.
88. Kelly NH, Schimenti JC, Ross FP, van der Meulen MCH. Transcriptional profiling of cortical versus cancellous bone from mechanically-loaded murine tibiae reveals differential gene expression. *Bone*. 2016;86:22-9.

89. Lean JM, Jagger, C. J., Chambers, T.J., Chow, J. W. Increased insulin-like growth factor I mRNA expression in response to mechanical stimulation. *Am J Physiol.* 1995;268(2 Pt 1):E318-27.
90. Firth EC, Delahunt J, Wichtel JW, Birch HL, Goodship AE. Galloping exercise induces regional changes in bone density within the third and radial carpal bones of Thoroughbred horses. *Equine Veterinary Journal.* 1999;31(2):111-5.
91. Young DR, Nunamaker DM, Markel MD. Quantitative evaluation of the remodeling response of the proximal sesamoid bones to training-related stimuli in Thoroughbreds. *Am J Vet Res.* 1991;52:1350.
92. Poulos PW. Radiographic and histologic assessment of proximal sesamoid bone changes in young and working horses, in *Proceedings. 35th Annu Conv Am Assoc Equine Pract.* 1989;34:347.
93. McCarthy RN, Jeffcott LB. Effects of treadmill exercise on cortical bone in the third metacarpus of young horses. *Res Vet Sci.* 1992;52(1):28-37.
94. Cornelissen BPM, van Weeren PR, Ederveen AGH, Barneveld A. Influence of exercise on bone mineral density of immature cortical and trabecular bone of the equine metacarpus and proximal sesamoid bone. *Equine Veterinary Journal.* 1999;31(S31):79-85.
95. Anthenill LA, Gardner IA, Pool RR. Comparison of macrostructural and microstructural bone features in Thoroughbred racehorses with and without midbody fracture of the proximal sesamoid bone. *Am J Vet Res.* 2010;71:755.
96. Anthenill LA, Stover SM, Gardner IA. Association between findings on palmarodorsal radiographic images and detection of a fracture in the proximal sesamoid bones of forelimbs obtained from cadavers of racing Thoroughbreds. *Am J Vet Res.* 2006;67:858.
97. Peloso JG, Vogler Iii JB, Cohen ND, Marquis P, Hilt L. Association of catastrophic biaxial fracture of the proximal sesamoid bones with bony changes of the metacarpophalangeal joint identified by standing magnetic resonance imaging in cadaveric forelimbs of Thoroughbred racehorses. *Journal of the American Veterinary Medical Association.* 2015;246(6):661-73.
98. Jacobs CR, Temiyasathit S, Castillo AB. Osteocyte mechanobiology and pericellular mechanics. *Annual Review of Biomedical Engineering.* 2010;12:369-400.

99. Morgan TG, Bostrom MPG, van der Meulen MCH. Tissue-level remodeling simulations of cancellous bone capture effects of in vivo loading in a rabbit model. *Journal of Biomechanics*. 2015;48(5):875-82.
100. Carter DR. The relationship between in vivo strains and cortical bone remodeling. *Critical Reviews in Biomedical Engineering*. 1982;8(1):1-28.
101. Goff MG, Chang KL, Litts EN, Hernandez CJ, editors. Strain Distributions in Cancellous Bone Are Insensitive to Small Off-axis Loads in the Rodent Tail Loading Model. 59th Annual Trans Orthop Res Society; 2013; San Antonio, TX, USA.
102. Johnson BJ, Stover SM, Daft BM, Kinde H, Read DH, Barr BC, et al. Causes of death in racehorses over a 2 year period. *Equine Veterinary Journal*. 1994;26(4):327-30.
103. Stover SM, Murray A. The California Postmortem Program: Leading the Way. *Veterinary Clinics of North America: Equine Practice*. 2008;24(1):21-36.
104. Sarrafian TL, Case JT, Kinde H, Daft BM, Read DH, Moore JD, et al. Fatal musculoskeletal injuries of Quarter Horse racehorses: 314 cases (1990–2007). *Journal of the American Veterinary Medical Association*. 2012;241(7):935-42.
105. Verheyen K, Price J, Lanyon L, Wood J. Exercise distance and speed affect the risk of fracture in racehorses. *Bone*. 2006;39(6):1322-30.
106. Cohen ND, Berry SM, Peloso JG, Mundy GD, Howard IC. Association of high-speed exercise with racing injury in thoroughbreds. *J Am Vet Med Assoc*. 2000;216(8):1273-8.
107. Anthenill LA, Stover SM, Gardner IA. Risk factors for proximal sesamoid bone fractures associated with exercise history and horseshoe characteristics in Thoroughbred racehorses. *Am J Vet Res*. 2007;68:760.

CHAPTER 2

LOCAL TISSUE STRAIN REGULATES BONE FORMATION

The following chapter is published in the Journal of Biomechanics and reprinted here with permission. The reference to the published work is:

- Cresswell, E.N.; Goff, M.G.; Nguyen, T.M.; Lee, W.X.; Hernandez, C.J. Spatial Relationships between Bone Formation and Mechanical Stress within Cancellous Bone. *Journal of Biomechanics* 49(2):222-228, 2016.

2.1 Introduction

The idea that bone adapts to habitual mechanical stimulation originated over 150 years ago and was based on observations that the alignment of cancellous bone microarchitecture matches the orientation of principal stresses (see (108) for a thorough review). The degree to which bone density and internal and external morphology is altered in response to mechanical stimuli is key to understanding the potential of biophysical stimuli to improve bone microstructure and is also useful for the interpretation of trabecular bone alignment in rare specimens from the fossil record (109).

Experimental application of controlled mechanical loads to the bones of live animals has provided a wealth of information on bone functional adaptation (110). In cortical bone, in vivo mechanical loading leads to increases in periosteal bone formation at the locations of greatest tensile and compressive strains (20). In cancellous bone, in vivo loading has been shown to result in increases in bone density and bone volume fraction (67, 73-75, 99). The vast majority of

studies examining in vivo mechanical loading of cancellous bone have addressed changes at the regional level (regions of cancellous bone 1-5 mm in size), yet theoretical analysis suggests that functional adaptation in bone occurs at the local level (as close as 10-100 micrometers)(100). In cortical bone, new bone formation after an acute mechanical stimulus has been correlated with local periosteal stresses and strains (21). In cancellous bone, local mechanical stress and strain associated with long-term loading (stimulus 5 days per week for 4 or more weeks) has been shown to be moderately predictive of locations of new bone formation (conditional probability no better than 45%) (84).

While the relationship between local tissue stress and strain and new bone formation has been established in cancellous bone for long-term loading (4 weeks or more of regular loading) (83, 84) it is not known how well local mechanical stimulus is associated with new bone formation over shorter time periods. Determining the spatial associations between mechanical stress/strain and new bone formation at the level of individual trabeculae immediately following an acute stimulus has the potential to provide a more direct evaluation of mechanosensory mechanisms. While stress and strain in mineralized tissue are believed to be the primary stimulus, there is evidence that fluid flow within the lacunar canalicular network (98) and fluid flow and pressure in the marrow space have been associated with bone formation (111-115). The ability to assess the spatial association between bone formation and mechanical stress and strain is necessary to differentiate among mechanosensory mechanisms, particularly if such measures are made soon after loading.

The long term goal of this line of investigation is to determine the mechanotransduction mechanisms in cancellous bone. Here we examine the spatial relationship between local mechanical stress/strain and bone formation in the first week after a mechanical loading

stimulus. Specifically, we determine the relationship between tissue stress and strain within cancellous bone and individual locations of bone formation stimulated by mechanical loading.

2.2 Methods

2.2.1 In vivo Loading and Micro-Computed Tomography

Three month old, female Sprague Dawley rats were used in this study (n=14). Animals were housed individually in a 12-hour light 12-hour dark cycle and fed standard rat chow ad libitum. Animal use was approved by the local IACUC.

Mechanical stimulus was applied to regions of cancellous bone using the rat tail loading model (69, 116). The animals were anesthetized using isoflurane inhalation and threaded Kirschner wires (K-wire, dia. = 1.6 mm, Zimmer, Warsaw, IN) were inserted into the seventh (Cd7) and ninth caudal vertebra (Cd9). K-wire positioning was ensured using digital radiographs (Preva, Progeny, Lincolnshire, IL). Following surgical implantation, K-wires were secured in a single piece aluminum external fixator to prevent displacement and rotation of the K-wires relative to one another, thereby unloading the eighth caudal vertebrae (Fig 2-1A,B). Animals were returned to normal cage activity for 3 weeks to allow healing around the implants.

Three weeks after surgery, animals were anesthetized, K-wires were removed from the external fixator, and micro-computed tomography images (CT-120, GE Healthcare, Little Chalfont, Buckinghamshire, United Kingdom) of the eighth caudal vertebrae were acquired (25µm voxel size, 80kVp, 32mA, 1200 projections, 100ms integration time). Immediately following image acquisition, the K-wires were secured into custom fixtures within a materials testing device (Bose EnduraTech LM1 test bench, Bose Corporation, Minnetonka, MN). Animals were divided into two groups, a loaded and pinned not loaded control (n=7 per group).

Animals in the loaded group were anesthetized through isoflurane inhalation and compressive loading was applied through the two K-wires onto the eighth caudal vertebra. Loading was applied first in a ramp from 0N to 25N at 1N/sec, followed by cyclic sinusoidal compressive loading from 25N to 100N at 0.5Hz for 300 cycles. Preliminary assessment with strain gages indicated that the maximum applied load of 100N was associated with surface strains of $2141 \pm 644 \mu\epsilon$ on the dorsal and $771 \pm 534 \mu\epsilon$ (mean \pm SD, n=5) on the ventral surfaces (117). Animals in the pinned not loaded control group were anesthetized and had K-wires secured into the custom loading fixtures for the same length of time but no load was applied. The protocol was repeated once per day for 3 consecutive days and K-wires were secured in the external fixators between loading sessions. Bone formation markers were administered via intraperitoneal injection at 2 days (90mg xylene orange/ kg body weight) and 7 days (10mg calcein/ kg body weight) after loading. Animals were euthanized 11 days post loading and bones were collected for analysis.

2.2.2 Finite Element Modeling

The distribution of tissue stress/strain within the eighth caudal vertebrae during loading was determined using high resolution finite element models generated from micro-computed tomography images (micro-CT) collected prior to loading. Following the application of a Gaussian filter (radius = 1 voxel) the bone was segmented using a locally adaptive threshold based on edge detection (118). Finite element (FE) models were created by converting each voxel into 8 node linear brick elements using custom software (119) (element size $25 \mu\text{m}$ which has been shown to be sufficient for modeling cancellous bone microstructure (120, 121)). Bone tissue was assigned a Young's modulus consistent with surface strains achieved in preliminary experiments ($E = 9.4 \text{GPa}$) (117) and Poisson's ratio $\nu = 0.3$. The intervertebral discs were

included in the model as cylindrical discs attached at the ends of the bones with a diameter of 3 mm and height of 0.5 mm. Discs were modeled with $E = 4.0\text{MPa}$ and $\nu=0.3$ (122). The peak load applied to the bone in vivo was simulated by applying a compressive load of 100N across the caudal discs and constraining axial displacement at the distal disc (Fig 2-1C). The finite element models were implemented with ABAQUS (Version 6, Waltham, MA) on the Gordon supercomputer (XSEDE, vSMP node, for ~140 total computing hours)(123). Models consisted of 3.85 ± 0.25 million elements (mean \pm SD). Strain energy density (SED), maximum principal strain, and von Mises stress within each element was used to evaluate local mechanical stimuli. Similar trends were found with all 3 assays of local mechanical stimuli so only SED is reported for consistency with other work (74, 84, 124). Finite element models were performed for the pinned not loaded controls to provide a null control for SED distributions.

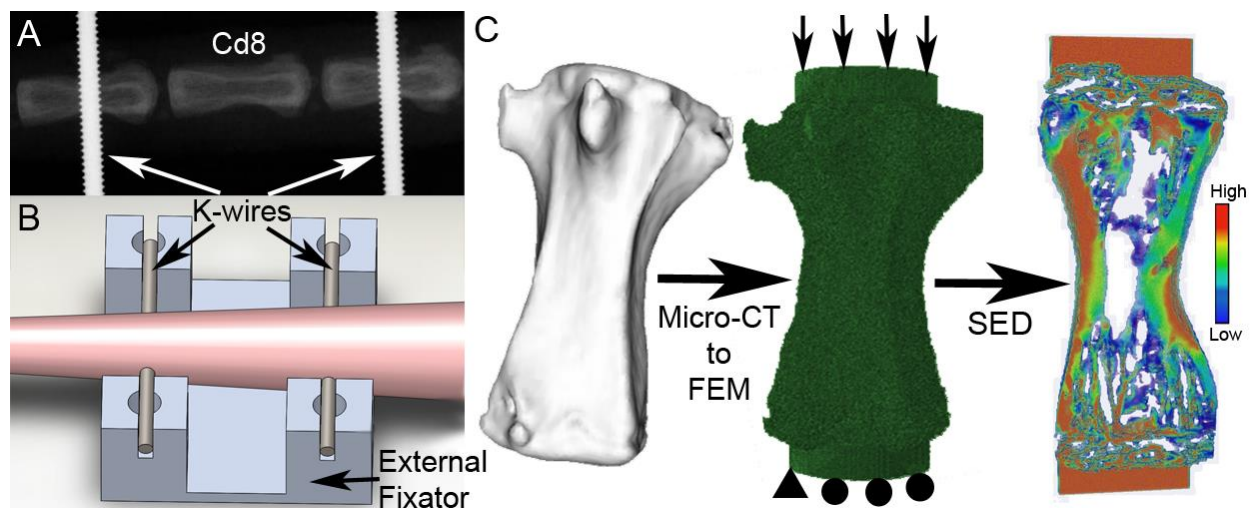


Figure 2-1: (A) K-wires were inserted into the Cd7 and Cd9. (B) K-wires were secured into an external fixator between loading sessions. (C) Micro-CT images were converted to finite element models with intervertebral discs and boundary conditions as shown.

2.2.3 Image Acquisition and Processing

The eighth caudal vertebrae were collected and soft tissue was removed. The endplates were cut away with a low speed diamond saw (Isomet, Beuhler, Lake Bluff, IL) and marrow was removed using a low pressure water jet and short periods of ultrasonication. Specimens were fixed in 70% ethanol for 48 hours, dehydrated in increasing concentrations of ethanol and embedded undecalcified in methyl methacrylate made opaque by the addition of sudan black dye in preparation for image acquisition with serial milling (125). Serial milling is a destructive imaging technique that results in a three-dimensional image of the bone and two different fluorescent markers with a voxel size of $0.7 \times 0.7 \times 5.0\mu\text{m}$ (126) (please see Supplementary Materials for a more detailed description of the technique). Following image reconstruction, three-dimensional dynamic bone histomorphometry was performed to measure three-dimensional mineralizing surface per bone surface (3D MS/BS), the number of bone formation sites, and the volume of bone formed during the experiment (FV/BV, formation volume fraction).

2.2.4 Spatial Associations between Bone Formation and Mechanical Strain

Images collected using serial milling were registered to finite element models using commercial software (AffineRegistration, AMIRA, v5.3.3, Visage Imaging, San Diego, CA) which includes some downsampling of serial milling images and upsampling of FE models for registration (Fig. 2-2). Regions of cancellous bone were segmented manually by a trained observer. The central region of each specimen contained negligible amounts of trabecular bone and was removed from analysis (74). The region of each bone analyzed therefore comprised of

two regions of cancellous bone, each 1.4 mm in height located 1 mm away from each growth plate.

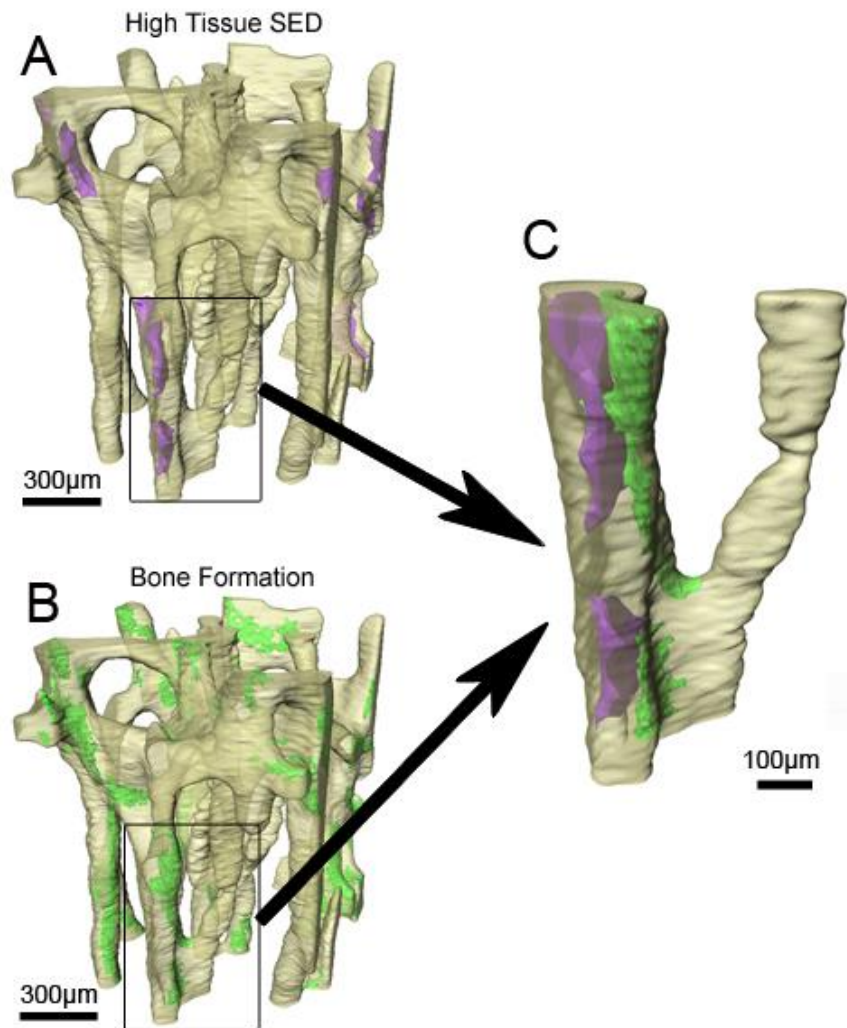


Figure 2-2: (A) A region of cancellous bone with locations of high SED indicated in purple is shown. (B) Three-dimensional images of fluorescent markers of bone formation (green) were used to identify regions of bone formation that occurred in the week after loading.

Four different techniques were used to test the idea that bone formation was preferentially located at regions of increased tissue stress/strain: an object number-based spatial correlation approach, a volume-based spatial correlation approach (117), measuring SED at

locations of bone formation vs. SED at all bone surfaces, and assessing the probability of observing bone formation as a function of local tissue stress/strain (84).

The object number-based spatial correlation tests the idea that two types of objects are preferentially near one another. We tested the idea that bone formation events were near locations of high SED and also considered the converse questions that locations of high SED were near bone formation events. High SED was defined as the 80th percentile of SED within each specimen (a preliminary parametric analysis revealed that our conclusions were not altered by the numerical value of this choice for a range of 70th to 95th percentile).

The volume-based spatial correlation tests the idea that the volumes occupied by two different types of objects in a three-dimensional image are preferentially near one another (117). In this case we test the idea that the formation volumes were preferentially near locations of high SED and the converse question that high SED volume was near bone formation. The volume-based spatial correlation is determined as the volume of newly formed bone near tissue experiencing high SED divided by the volume of bone tissue selected at random that is near tissue experiencing high SED. A value greater than one indicates a positive correlation (new bone formation and tissue with high SED are near one another) while a value equal to one indicates no spatial correlation (new bone formation is not preferentially near or far from tissue experiencing high SED). The volume based spatial correlation was determined at distances ranging from 25 μ m to 100 μ m (the average trabecular thickness).

The average SED (calculated as the geometric mean) was determined for all bone surface voxels and bone surfaces within 25 microns of bone formation. A ratio of SED near bone formation to the SED at all bone surfaces was determined per specimen and compared to 1.0. A

ratio greater than 1.0 indicates that SED is higher than average surface SED near locations of bone formation.

The probability of observing bone formation was determined as the percentage of newly formed bone tissue at each value of SED (84). Locations of SED in the probability analysis were confined to the surface voxels of the bone.

2.2.5 Statistics

Measures of bone formation were compared between loaded and control groups using a student's t-test. A t-test was used to determine if the ratios describing the volume-based spatial correlation and differences in SED differed from 1.0 (no difference).

2.3 Results

The three-dimensional mineralizing surface in loaded animals ($17.68 \pm 2.17\%$, mean \pm SD) was greater than that observed in pinned not loaded controls ($9.05 \pm 3.20\%$) (Fig. 2-3A). The volume of bone formed between the formation labels in loaded animals was more than four times greater than that in pinned not loaded controls (loaded: $7.09 \pm 1.97\%$; control: $1.44 \pm 0.50\%$; Fig. 2-3B). Although only 3 days of load had been applied, BV/TV was slightly greater in loaded animals ($p = 0.09$, Fig. 2-3C). The increase in bone formation in loaded specimens was a result of an increase in the number of bone formation sites as well as larger formation sites (Fig. 2-3D, 2-3E). Regions of new bone formation in the cancellous envelope were lamellar, but each of the loaded specimens showed regions of woven bone on the periosteal surfaces (no periosteal woven bone was observed in pinned not loaded control animals).

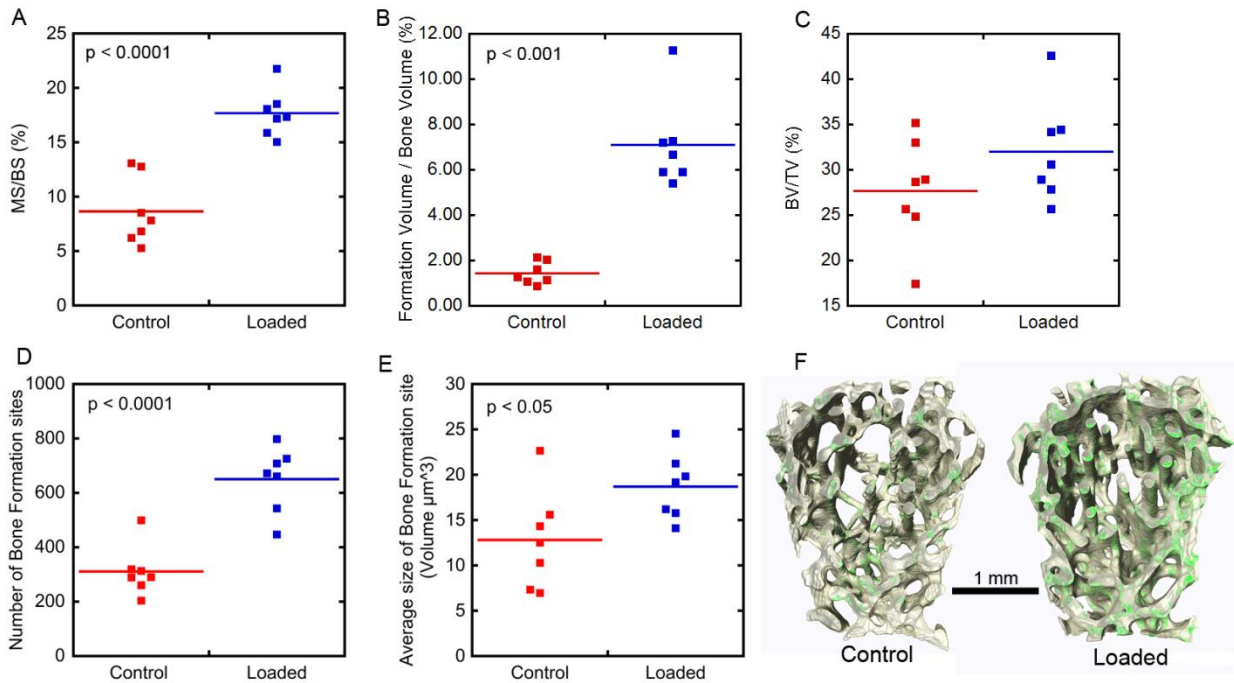


Figure 2-3: (A) Mineralizing surface was twice as large in the loaded group as compared to controls. (B) In loaded animals, the volume of bone formed in the week after loading was greater than in pinned not loaded controls. (C) Bone volume fraction was not significantly increased. (D) The number of bone formation sites increased due to loading. (E) The volume of each bone formation site was larger in loaded specimens as compared to unloaded controls. (F) Three-dimensional images of bone (tan) and bone formation (green) are shown for a control and loaded specimen.

There were, on average, more than twice as many sites of bone formation in the loaded animals than in the pinned not loaded controls (loaded: 650.71 ± 118.54 ; control: 310.71 ± 91.55 ; Fig. 2-4). However, in the loaded animals, half of the bone formation sites were near regions of high SED (within $25\mu\text{m}$). Hence in loaded animals, the increase in the number of bone formation sites was caused by formation associated with high SED. As many as $46.74 \pm 7.37\%$ of the locations of high SED were near regions of bone formation in loaded animals (as compared to $16.80 \pm 3.58\%$ in controls).

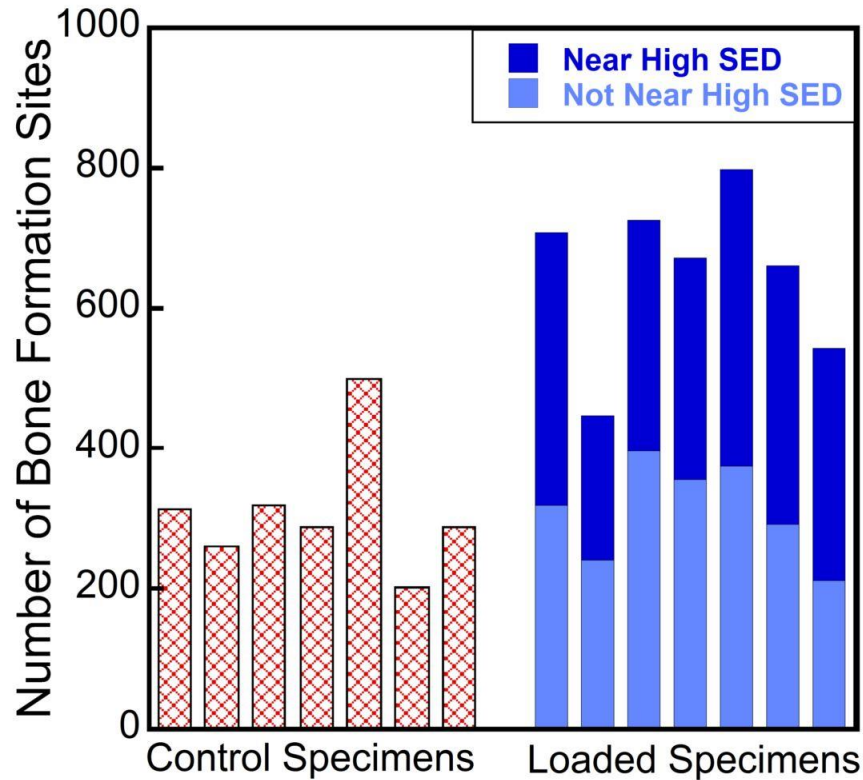


Figure 2-4: The number of bone formation sites in the control group is shown for each of the specimens. The number of bone formation sites in loaded specimens near locations of high SED (within 25 μm) and not near high SED is indicated. The number of bone formation sites near locations of high SED in loaded specimens is similar to the number of formation sites observed in pinned not loaded control animals.

The ratio of SED near bone formation to SED at all bone surfaces was greater in loaded specimen (Fig 2-5). Average SED was found to be 7.96 ± 2.49 kPa (geometric mean \pm SD) with a 95% confidence interval of 5.66 to 10.27 kPa. (See also supplementary material).

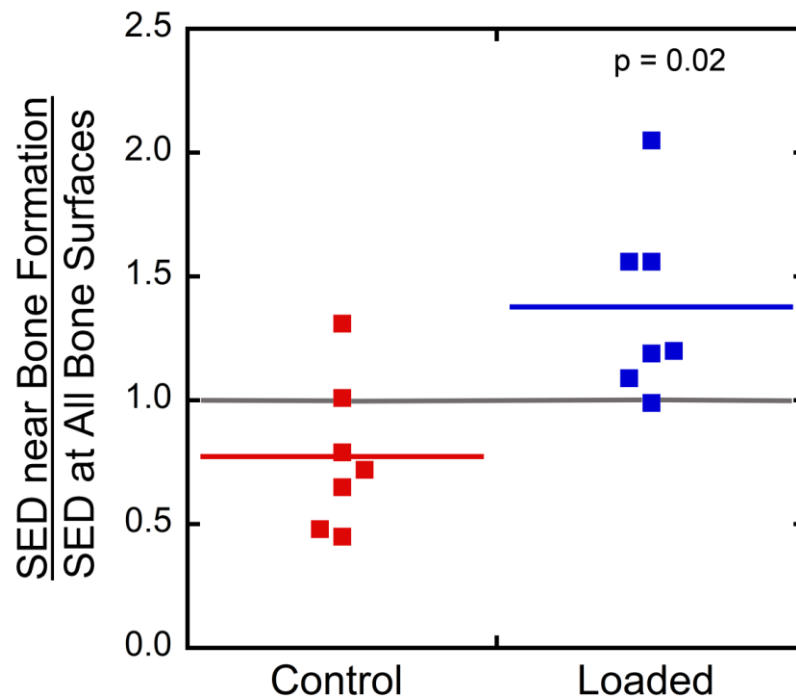


Figure 2-5: The ratio of mean SED near bone formation (within 25 μm) to SED at all bone surfaces is greater than 1.0 ($p=0.02$) in loaded specimens, therefore SED is greater at locations of bone formation than elsewhere. The ratio in control specimens is not greater than 1.0.

In loaded specimens, the probability of observing bone formation at a location in the microstructure was greater at regions experiencing greater SED (Fig 2-6). In controls there was no relationship between the probability of observing bone formation and tissue SED and the probability of observing bone formation was lower than that in loaded specimens. Volume based spatial correlations did not indicate a correlation between the volume of tissue experiencing high SED and the volume of bone formation (Fig. 2-7).

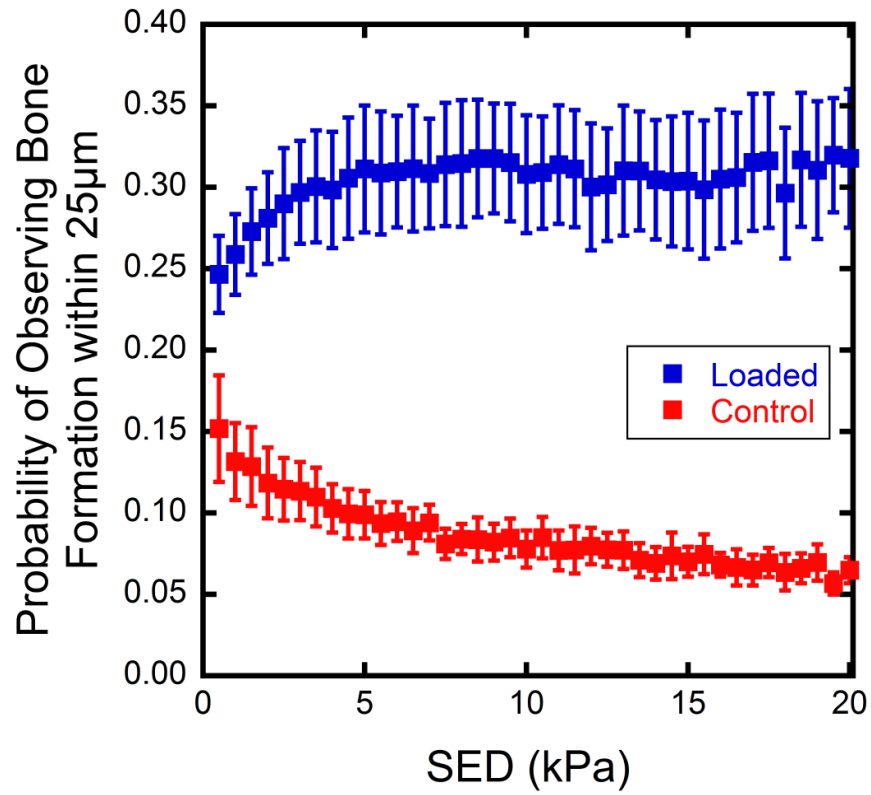


Figure 2-6: The probability of observing bone formation within 25 µm of a given SED range increases in loaded specimen and decreases in controls. Locations of SED values were constrained to the surface of bone. Error bars are standard error.

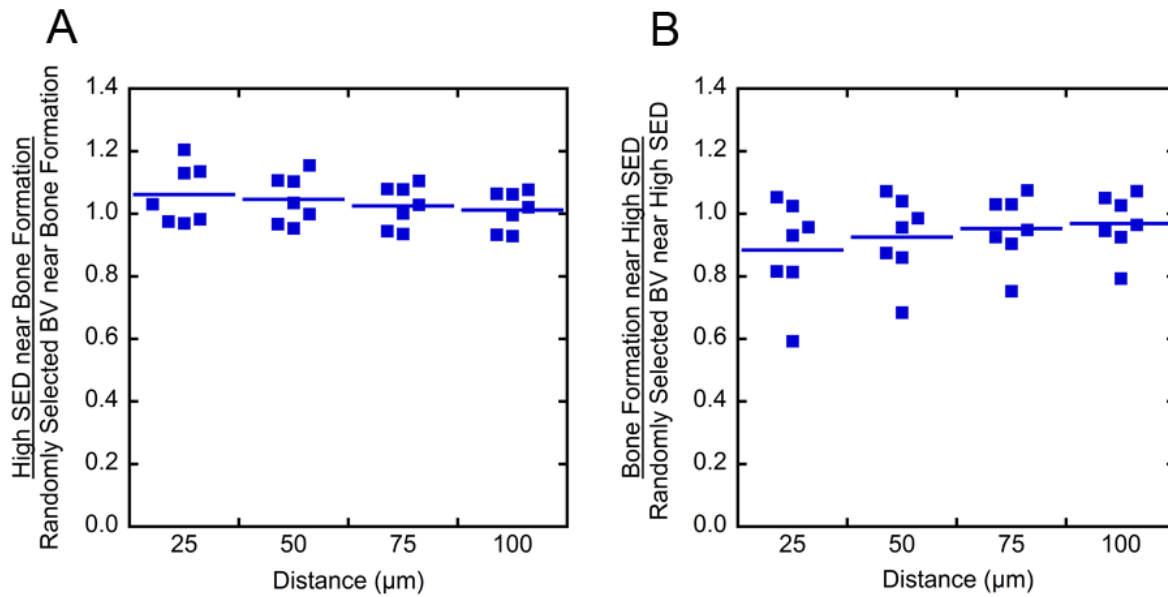


Figure 2-7: The volume based spatial correlation of loaded specimens is shown. (A) The likelihood of bone formation near regions of high SED is shown and (B) the likelihood of high SED near regions of bone formation is shown. A ratio greater than 1.0 indicates bone formation is preferentially near high SED. When the ratio is less than 1.0 bone formation is preferentially distant from high SED.

2.4 Discussion

The objective of this study was to determine the spatial relationship between local mechanical stress/strain and bone formation in the week after a short-term mechanical loading stimulus. We found a spatial correlation between bone formation stimulated by mechanical loading and the tissue stress/strain environment at the scale of 25 micrometers. Hence, even early functional adaptation responses in bone within a week of a short-term stimulus are associated with local tissue stress/strain.

The use of four different assays of the spatial association between bone formation and high SED provides a full picture of the association between bone formation and tissue stress and strain. The increase in number of bone formation sites caused by loading was due to formation sites near tissue experiencing high SED. Strain energy density was greater near bone formation

than the average on all bone surfaces. The probability of observing bone formation increased at greater SED magnitudes. Therefore, three measures indicated a spatial association between bone formation and tissue stress and strain. However, the volume-based spatial correlation did not observe an association between newly formed bone and bone volume experiencing high SED. We interpret these results as indicating that many new formation sites appeared near regions of the tissue experiencing high SED, but a large proportion of the bone volume formed was due to expansion of bone remodeling events that were ongoing prior to mechanical stimulus.

The probability of observing new bone formation at the regions of greatest SED may seem small (32%) but is similar in magnitude to the largest probability (45%) reported using the mouse tail loading model that involved 4 weeks of daily loading and higher resolution finite element models (10.5 μm elements) (84). As we expect larger amounts of bone formed over 4 weeks to be associated with mechanical loading, we consider our findings after 3 days of loading to be consistent with that of Schulte and colleagues. Given the consistency in our measure, it is unlikely that improvements in finite element resolution would improve our predictive capabilities. We feel that it is more likely that variation in material properties and the osteocyte network could improve prediction.

There are several strengths to the current work. First, we have shown that small misalignments during experimental loading will not alter the locations of high SED identified by finite element models (117), providing confidence that the localization of mechanical stress and strain was accurate. Second, the use of serial milling makes it possible to directly measure small amounts of bone formation in three-dimensions. The serial milling approach has some advantages over the more commonly used sequential in vivo micro-computed tomography technique for assessing bone formation (127-129). Serial milling, as we have performed, has a

higher resolution (1-5 μm voxels) than existing in vivo micro-computed tomography systems (10.5 μm voxels), making it possible to measure bone formation over periods as short as a week. Additionally, measures of bone formation using serial milling are based on fluorescent markers of bone formation, which are the gold standard for assessment of bone formation and, due to the increased resolution have smaller image registration/segmentation errors. For example, when using sequential micro-computed tomography imaging, small errors in image registration and partial volume effects on bone surfaces can influence measures of bone formation and resorption (130). To avoid registration error some practitioners disregard the outer layer of voxels on bone formation and resorption surfaces (131), limiting the accuracy of measures of the number and size of formation and resorption events. An important limitation of serial milling is that it is a destructive imaging approach and cannot be performed in vivo. Sequential micro-CT imaging provides accurate measures of net changes in bone volume and microarchitecture between scans and is therefore a useful method of measuring changes in microarchitecture over longer time periods.

A limitation of the current work is the presence of woven bone on the periosteum of loaded vertebra. The presence of woven bone on the surfaces has the potential to influence physiological processes in the endosteal and cancellous bone envelopes. However, bone formation on the endosteal surface and in cancellous regions remained lamellar and the probability of observing bone formation at regions of high tissue SED (largest value 32%) was similar to that reported by others following 4 weeks of loading (45%, see below (84)), hence it is unlikely that the presence of woven bone on the periosteal surfaces influenced our conclusions regarding the spatial association of bone formation and tissue stress and strain.

It is useful to consider the current work in the context of prior investigations. Chow et al. showed that as little as one loading session of 300 cycles is capable of increasing bone formation rate through increases in both double labeled surface and mineral apposition rate (69). A series of recent investigations using tail loading in the mouse and sequential micro-CT imaging, demonstrated that long-term mechanical loading (4 weeks or more, 5 days/week) resulted in noticeable alterations in cancellous bone microarchitecture that could be explained, to some degree by tissue strain energy density (84). Another difference between our work and prior investigations is related to the external fixation and disuse present prior to applied loading bouts. In the current study we used a one piece external fixator resulting in unloading of the eighth caudal vertebra in the three weeks between pin placement and mechanical stimulus. Recent work using the mouse tail loading system did not utilize external fixation, presumably maintaining habitual activity (70, 74, 84) and the resulting probability of observing bone formation in the microstructure showed some relationship to SED even in the pinned not loaded control animals (84).

While increases in mechanical stimuli lead to new bone formation, the mechanosensory mechanisms are complicated. Determining the spatial correlation between bone formation and tissue stress/strain immediately following an acute stimulus has the potential to allow more direct identification of mechanosensory mechanisms. For example, although tissue stress/strain is believed to be the primary mechanical stimulus, one group has reported that fluid pressure in the marrow space was more strongly associated with the locations of bone formation ($R^2 = 0.83$) than strain energy density within mineralized tissues ($R^2 = 0.55$) (115). Gene expression in the marrow differs from that in cancellous bone as well as that in cortical bone (132). Hence,

identifying the most compelling the spatial correlations between formation and mechanical stress/strain will identify which material to isolate to identify signaling processes.

In conclusion, we demonstrated that bone formation within the first week after a mechanical stimulus is spatially associated with regions of increased tissue stress/strain within cancellous bone.

2.5 Supplemental Material

2.5.1 Supplementary Methods: Serial Milling

Embedded specimens were subjected to three-dimensional imaging using serial milling. Serial milling is a fully automated technique that involves repeatedly milling away $5\mu\text{m}$ from the top of the specimen and imaging the newly exposed specimen surface (125). Images were collected with a voxel size of $0.7 \times 0.7 \times 5.0\mu\text{m}$. Images were collected using three different fluorescent filter sets, one filter set to observe bone (350/420 nm Excitation/Emission, to image bone autofluorescence) and two different filter sets for each of the bone formation markers (545/620 nm for xylenol orange, and 470/525 nm for calcein) (133). Raw images of each specimen required 1200 slices with a 4×4 mosaic per slice of 16-bit grayscale images resulting in ~485 GB of data (7 days of image acquisition per specimen).

Image processing was used to correct for non-uniform illumination, tile the mosaics, and adjust for fluorescent signal originating below the optical plane (133). Bone was segmented using an iterative threshold approach (for detailed information on image processing see (133)). Each of the two bone formation markers were segmented using global thresholds identified manually by a trained observer. After segmentation, bone and the two images of bone formation markers were resampled to $5 \times 5\mu\text{m}$ in-plane using the Lanczos method (imresize, Matlab 2010a, Mathworks,

Natick MA, USA), smoothing the global threshold. Three-dimensional closing using a spherical structuring element was applied to combine pairs of bone formation markers, thereby directly identifying the volume of bone formed at each formation event during the 5 day period between application of the formation markers. A bone formation event with volume less than $10,000 \mu\text{m}^3$ was classified as noise and removed from the image (such small objects are similar in size to the volume of 14 osteoblasts and occupied less than 0.5% of the formation volume)(125).

2.5.2 Supplementary Figures

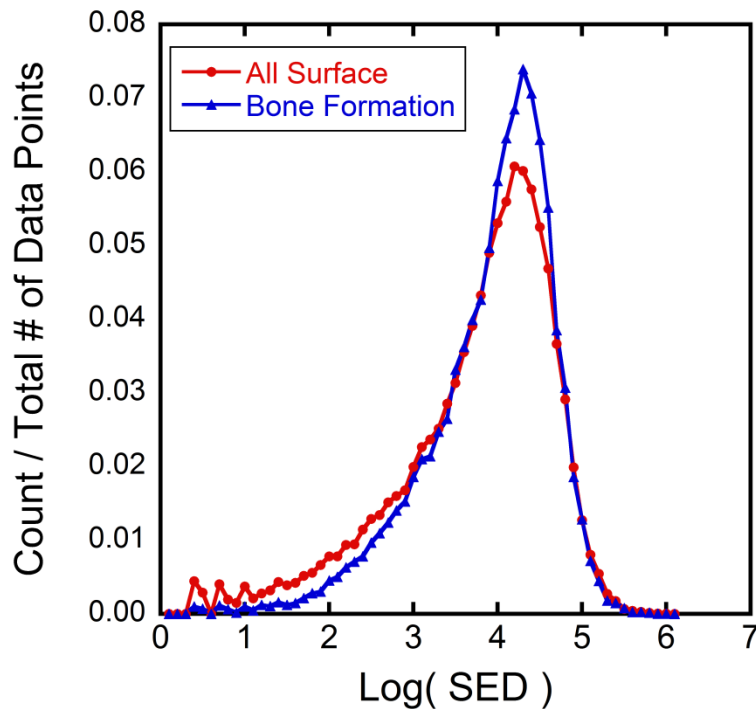


Figure 2-8: The histogram of the log transform of the SED distribution of a single loaded specimen is displayed. The distribution of SED near bone formation surfaces is shown separately from the SED distribution of all bone surfaces. Histograms were normalized by the total number of data points per histogram so that the area under the curve of each histogram sums to 1.0. SED ranged from 1Pa to 0.5MPa with the majority of the data in between 1 kPa to 100 kPa. There is a shift in the distribution of SED near bone formation to higher values of SED as compared to the SED distribution of all bone surfaces.

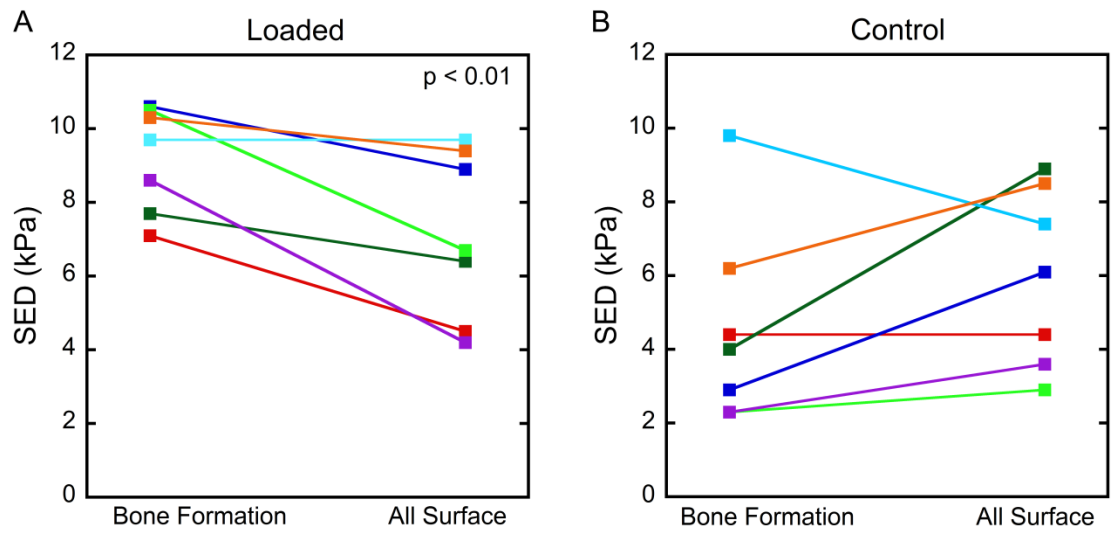


Figure 2-9: The average SED per specimen is shown at locations near bone formation and at all bone surfaces. Lines indicate findings from the same specimens. In loaded specimens the average SED is greater near bone formation than at all bone surfaces. Differences in mean SED were observed in the loaded group ($p < 0.01$, paired t-test).

REFERENCES

20. Torrance AG, Mosley JR, Suswillo RF, Lanyon LE. Noninvasive loading of the rat ulna in vivo induces a strain-related modeling response uncomplicated by trauma or periosteal pressure. *Calcified Tissue International*. 1994;54(3):241-7.
21. Kotha SP, Hsieh YF, Strigel RM, Muller R, Silva MJ. Experimental and finite element analysis of the rat ulnar loading model--correlations between strain and bone formation following fatigue loading. *Journal of Biomechanics*. 2004;37(4):541-8.
67. van der Meulen MC, Morgan TG, Yang X, Baldini TH, Myers ER, Wright TM, et al. Cancellous bone adaptation to in vivo loading in a rabbit model. *Bone*. 2006;38(6):871-7.
69. Chow JW, Jagger CJ, Chambers TJ. Characterization of osteogenic response to mechanical stimulation in cancellous bone of rat caudal vertebrae. *American Journal of Physiology*. 1993;265(2 Pt 1):E340-7.
70. Webster DJ, Morley PL, van Lenthe GH, Muller R. A novel in vivo mouse model for mechanically stimulated bone adaptation--a combined experimental and computational validation study. *Computer Methods in Biomechanics and Biomedical Engineering*. 2008;11(5):435-41.
73. Fritton JC, Myers ER, Wright TM, van der Meulen MC. Loading induces site-specific increases in mineral content assessed by microcomputed tomography of the mouse tibia. *Bone*. 2005;36(6):1030-8.
74. Lambers FM, Schulte FA, Kuhn G, Webster DJ, Muller R. Mouse tail vertebrae adapt to cyclic mechanical loading by increasing bone formation rate and decreasing bone resorption rate as shown by time-lapsed in vivo imaging of dynamic bone morphometry. *Bone*. 2011;49(6):1340-50.
75. Webster D, Wasserman E, Ehrbar M, Weber F, Bab I, Muller R. Mechanical loading of mouse caudal vertebrae increases trabecular and cortical bone mass--dependence on dose and genotype. *Biomechanics and Modeling in Mechanobiology*. 2010.
83. Webster D, Wirth A, van Lenthe GH, Muller R. Experimental and finite element analysis of the mouse caudal vertebrae loading model: prediction of cortical and trabecular bone adaptation. *Biomechanics and Modeling in Mechanobiology*. 2012;11(1-2):221-30.

84. Schulte FA, Ruffoni, D., Lambers, F. M., Christen, D., Webster, D. J., Kuhn, G., Muller, R. Local mechanical stimuli regulate bone formation and resorption in mice at the tissue level. *PloS one*. 2013;8(4):e62172.
98. Jacobs CR, Temiyasathit S, Castillo AB. Osteocyte mechanobiology and pericellular mechanics. *Annual Review of Biomedical Engineering*. 2010;12:369-400.
99. Morgan TG, Bostrom MPG, van der Meulen MCH. Tissue-level remodeling simulations of cancellous bone capture effects of in vivo loading in a rabbit model. *Journal of Biomechanics*. 2015;48(5):875-82.
100. Carter DR. The relationship between in vivo strains and cortical bone remodeling. *Critical Reviews in Biomedical Engineering*. 1982;8(1):1-28.
108. Cowin SC. The false premise in Wolff's law. In: Cowin SC, editor. *Bone Mechanics Handbook*. Boca Raton: CRC Press; 2001.
109. Ryan TM, Ketcham RA. Femoral head trabecular bone structure in two omomyid primates. *Journal of Human Evolution*. 2002;43(2):241-63.
110. van der Meulen MC, Hernandez CJ. Adaptation of Skeletal Structure to Mechanical Loading. In: Marcus R, Feldman D, Dempster D, Cauley J, Luckey M, editors. *Osteoporosis*. 4th Edition ed. San Diego, CA, USA: Academic Press; 2013.
111. Metzger TA, Kreipke TC, Vaughan TJ, McNamara LM, Niebur GL. The In Situ Mechanics of Trabecular Bone Marrow: The Potential for Mechanobiological Response. *Journal of Biomechanical Engineering*. 2015;137(1):011006-.
112. Qin Y-X, Kaplan T, Saldanha A, Rubin C. Fluid pressure gradients, arising from oscillations in intramedullary pressure, is correlated with the formation of bone and inhibition of intracortical porosity. *Journal of Biomechanics*. 2003;36(10):1427-37.
113. Kwon RY, Meays DR, Tang WJ, Frangos JA. Microfluidic enhancement of intramedullary pressure increases interstitial fluid flow and inhibits bone loss in hindlimb suspended mice. *Journal of Bone and Mineral Research* 2010;25(8):1798-807.
114. Hu M, Cheng J, Qin Y-X. Dynamic hydraulic flow stimulation on mitigation of trabecular bone loss in a rat functional disuse model. *Bone*. 2012;51(4):819-25.
115. Webster D, Schulte FA, Lambers FM, Kuhn G, Müller R. Strain energy density gradients in bone marrow predict osteoblast and osteoclast activity: A finite element study. *Journal of Biomechanics*. 2015;48(5):866-74.
116. Guo XE, Eichler MJ, Takai E, Kim CH. Quantification of a rat tail vertebra model for trabecular bone adaptation studies. *Journal of Biomechanics* 2002;35(3):363-8.

117. Goff MG, Chang KL, Litts EN, Hernandez CJ. The effects of misalignment during in vivo loading of bone: techniques to detect the proximity of objects in three-dimensional models. *Journal of Biomechanics*. 2014;47(12):3156-61.
118. Waarsing JH, Day JS, Weinans H. An Improved Segmentation Method for In Vivo μ CT Imaging. *Journal of Bone and Mineral Research*. 2004;19(10):1640-50.
119. Lynch ME, Main RP, Xu Q, Walsh DJ, Schaffler MB, Wright TM, et al. Cancellous bone adaptation to tibial compression is not sex dependent in growing mice. *Journal of Applied Physiology*. 2010;109:685-91.
120. Guldberg RE, Hollister SJ, Charras GT. The accuracy of digital image-based finite element models. *Journal of Biomechanical Engineering*. 1998;120(4):289-95.
121. Niebur GL, Yuen JC, Hsia AC, Keaveny TM. Convergence behavior of high-resolution finite element models of trabecular bone. *Journal of Biomechanical Engineering*. 1999;121(6):629-35.
122. Elliott AM, Sarver JJ. Validation of the Mouse and Rat Disc as Mechanical Models of the Human Lumbar Disc. *SPINE*. 2004;29(7):713-22.
123. Ray JT, Cockerill T, Dahan M, Foster I, Gaither K, Grimshaw A, et al. XSEDE: Accelerating Scientific Discovery. *Computing in Science and Engineering*. 2014;16(5):62-74.
124. Huiskes R. Effects of mechanical forces on maintenance and adaptation of form in trabecular bone. *Nature*. 2000;405:704-6.
125. Slyfield CR, Tkachenko EV, Wilson DL, Hernandez CJ. Three-dimensional dynamic bone histomorphometry. *Journal of Bone and Mineral Research*. 2012;27(2):486-95.
126. Slyfield CR, Niemeyer KE, Tkachenko EV, Tomlinson RE, Steyer GG, Patthanacharoenphon CG, et al. Three-dimensional surface texture visualization of bone tissue through epifluorescence-based serial block face imaging. *Journal of Microscopy*. 2009;236(1):52-9.
127. Liu S, Broucek J, Viridi AS, Sumner DR. Limitations of using micro-computed tomography to predict bone-implant contact and mechanical fixation. *Journal of microscopy*. 2012;245(1):34-42.
128. Schulte FA, Lambers FM, Mueller TL, Stauber M, Müller R. Image interpolation allows accurate quantitative bone morphometry in registered micro-computed tomography scans. *Computer Methods in Biomechanics and Biomedical Engineering*. 2012;17(5):539-48.

129. Kohler T, Beyeler M, Webster D, Müller R. Compartmental Bone Morphometry in the Mouse Femur: Reproducibility and Resolution Dependence of Microtomographic Measurements. *Calcified Tissue International*. 2005;77(5):281-90.
130. Lan S, Luo S, Huh BK, Chandra A, Altman AR, Qin L, et al. 3D image registration is critical to ensure accurate detection of longitudinal changes in trabecular bone density, microstructure, and stiffness measurements in rat tibiae by in vivo microcomputed tomography (μ CT). *Bone*. 2013;56(1):83-90.
131. de Bakker CMJ, Altman AR, Tseng W-J, Tribble MB, Li C, Chandra A, et al. μ CT-based, in vivo dynamic bone histomorphometry allows 3D evaluation of the early responses of bone resorption and formation to PTH and alendronate combination therapy. *Bone*. 2015;73:198-207.
132. Kelly NH, Schimenti JC, Patrick Ross F, van der Meulen MCH. A method for isolating high quality RNA from mouse cortical and cancellous bone. *Bone*. 2014;68:1-5.
133. Slyfield CR, Jr., Niemeyer KE, Tkachenko EV, Tomlinson RE, Steyer GG, Patthanacharoenphon CG, et al. Three-dimensional surface texture visualization of bone tissue through epifluorescence-based serial block face imaging. *Journal of microscopy*. 2009;236(1):52-9.

CHAPTER 3

OSTEOCYTES' ROLE IN MECHANOTRANSDUCTION

The following chapter is under preparation for publication to BONE. The author list and title is as follows:

- Cresswell, E.N.; Nguyen, T.M.; Horsfield, M.W.; Alepuz, A.J.; Metzger, T.A.; Niebur, G.L.; Hernandez, C.J. Mechanically Induced Bone Formation is not Sensitive to Local Osteocyte Density. BONE.

3.1 Introduction

Mechanical loads are a powerful anabolic stimulus for bone, and can cause increases in bone shape and bone density. The ability of bone to respond to mechanical stimuli is attributed to osteocytes, the bone cells that reside within the bone matrix and sense and respond to their mechanical environment. Improved understanding of the links between loads experienced by bones, mechanical stresses and strains in bone tissue and the resulting response by osteocytes will help to identify the mechanosensory and mechanotransduction pathways that are most influential in bone and therefore the most attractive therapeutic targets (48).

The ability of bone to respond to mechanical stimulus has been known for some time (54) and demonstrated experimentally by applying loads to the bones of live animals. The application of cyclic loads to the bones of live animals stimulates increases in bone formation in both cortical (20, 61, 62, 70, 72, 73) and cancellous

(66-68, 70, 73) bone leading to increased whole bone size and density. The anabolic effect of mechanical loading is influenced by load magnitude (63, 64, 69), load frequency (including rest periods) (77, 78) and circulating hormones (134, 135). While the effects of mechanical loading on whole bones are well documented, less is known about how stress and strain at the tissue level dictate mechanically-induced bone formation. A relationship between tissue stress and strain and mechanically-induced bone formation has been shown on the periosteal surfaces of bones (20, 21, 83). The periosteum, however, is a highly osteogenic microenvironment in and it is unclear how well mechanical adaptation on periosteal cortical bone describes processes in other envelopes (endosteum, cancellous bone, intracortical bone). Furthermore, recent investigations have shown that mechanically induced changes in gene expression in cancellous bone are different from those in cortical bone (88) suggesting that mechanotransduction mechanisms in cortical bone may be very different from those elsewhere in the skeleton.

Cancellous bone microarchitecture is preferentially aligned with habitual loads and is therefore often cited as evidence of bone functional adaptation (136). However, loads applied to cancellous bone result in a complex distribution of tissue stress and strain (10). Tissue stress in cancellous bone is highly variable; trabeculae submitted to bending loads experience tissue stresses varying from compressive to tensile over a very short distance (~ 100 micrometer trabecular thickness). In a series of experiments examining the relationship between tissue stress and strain and bone formation, Müller and colleagues used the rodent tail loading model with serial *in vivo* micro-computed tomography imaging to observe longitudinal changes in cancellous bone

microarchitecture caused by regular mechanical stimuli (3 days of cyclic loading/week). After 4-6 weeks of mechanical loading bone density increased and locations of new bone formation were shown to be at regions of bone tissue experiencing larger tissue stresses (83, 84, 115, 137). Recently, our group associated tissue stress and strain in cancellous bone with regions of bone formation over an even shorter time period (seven days after loading) (138). While these studies associate bone formation with greater tissue stress and strain, the ability of tissue stress and strain to predict the locations of bone formation was more modest; the probability of observing mechanically induced bone formation at a location did not exceed 32-47%, even at locations experiencing the greatest tissue stress and strain (84, 138). One possible explanation for these findings is that the studies did not account for variation in the population of osteocytes.

Osteocytes are, by far, the most abundant bone cell, outnumbering osteoclasts and osteoblasts by more than a factor of 10 (33). Mechanosensory mechanisms in osteocytes include fluid shear stress on the cell body or cell processes and bending of primary cilia (35). In response to mechanical stimuli osteocytes produce factors that can promote bone formation by osteoblasts including prostaglandin E2, nitric oxide, and insulin-like growth factor (41-44). Osteocytes may also increase local bone formation by down regulating production of osteoblastic negative regulators such as sclerostin and DKK1 (45-47). The well-established ability of osteocytes to respond to mechanical stimuli suggests that regions of bone tissue with greater osteocyte density would be more sensitive to increases in tissue stress and strain. Consistent with this

idea, computational models simulating bone mechanoadaptation that have included osteocyte distribution successfully generate trabecular bone-like structures (85).

While work to date is consistent with the concept that increased tissue stress and strain lead to local bone formation, the degree to which local osteocyte populations modulate mechanically induced bone formation is not known. Improved understanding of the relationship between tissue stress and strain, osteocytes, and mechanically induced bone formation may lead to the identification of new therapeutic targets. The long-term goal of this line of investigation is to understand functional adaptation in bone. In this study we determine the effect of osteocyte density on the relationship between local tissue stress and strain and regions of mechanically induced bone formation.

3.2 Methods

3.2.1 In vivo Loading and Micro-Computed Tomography

Six month old, female Sprague Dawley rats were used in this study (n=16). Animals were housed individually in a 12-hour light 12-hour dark cycle and fed standard rat chow ad libitum. Animal use was approved by the local IACUC.

The rat tail loading model was used to provide mechanical stimulus in vivo (69, 116, 138). Animals were anesthetized using isoflurane inhalation and threaded Kirschner wires (K-wire, dia. = 1.6 mm, Zimmer, Warsaw, IN) were inserted into the seventh (Cd7) and ninth caudal vertebra (Cd9). K-wire positioning was ensured using custom clamps holding the tail and confirmed using digital radiographs (Preva, Progeny, Lincolnshire, IL). After surgical insertion and cleaning of the wounds the K-

wires were secured in a single piece aluminum external fixator to prevent displacement and rotation of the K-wires relative to one another, thereby unloading the eighth caudal vertebrae. Animals were returned to normal cage activity for 21 days to allow complete integration of the K-wires in bone.

Prior to loading, animals were anesthetized and K-wires were removed from the external fixator and secured into custom fixtures within a materials testing device (Bose EnduraTech LM1 test bench, Bose Corporation, Minnetonka, MN). Animals were divided into two groups (n=8 per group), loaded and control (pinned not loaded). Animals in the loaded group experienced compressive loading through the two K-wires onto the eighth caudal vertebra (Cd8). Loading was applied first in a ramp from 0N to 25N at 1N/sec, followed by cyclic sinusoidal compressive loading from 25N to 75N at 0.5Hz for 300 cycles. Preliminary assessment with strain gages indicated that the maximum applied compressive load of 75N was associated with compressive strains of $935.3 \pm 32.0\mu\epsilon$ on the dorsal surface and $738.5 \pm 27.1\mu\epsilon$ on ventral surfaces (mean \pm SD). Animals in the control group were anesthetized and had K-wires secured into the custom loading fixtures for the same length of time as the loaded group but no load was applied. The procedure was repeated once per day for 3 consecutive days. The K-wires were secured in the external fixators between loading sessions.

Three days prior to loading, animals received intraperitoneal injections of a bone formation marker (20mg oxytetracycline/kg body weight) to label locations of active bone formation prior to applied mechanical loading. A different bone formation marker (10mg calcein/kg body weight) was administered via intraperitoneal injection at 2 and 7 days after loading completed. Animals were euthanized 11 days after the

start of loading and bones were dissected free from soft tissue for analysis in vitro. Each specimen was examined using three methods: high resolution finite element modeling (22 μ m voxel size) to determine the distribution of tissue stress and strain, nano-computed tomography (1.5 μ m voxel size) to identify the locations of osteocyte lacunae, and three-dimensional fluorescence based serial milling (0.7 X 0.7 X 5 μ m voxel size) to identify individual locations of bone formation (Fig. 3-1).

3.2.2 Distribution of Mechanical Stress and Strain

Images of the eighth caudal vertebrae were collected in vitro using micro-computed tomography (100kV, 9W, 0.7-1s exposure time, 1801 projections, 11 μ m voxel size). Bone was identified using a global threshold. High-resolution finite element models of the entire caudal vertebra were created from the micro-CT images by converting each voxel to a linear elastic hexahedral element (121). To reduce computational time, the finite element model was resampled to 22 μ m element size. Bone tissue was assigned a Young's modulus ($E = 9.4\text{GPa}$) and Poisson's ratio ($\nu = 0.3$) based on strain gage measurements/finite element models made in preliminary studies (117). The intervertebral discs were modeled as cylindrical discs attached at the ends of the bones with a diameter of 3 mm and height of 0.5 mm. Discs were assigned material properties of $E = 4.0\text{MPa}$ and $\nu=0.3$ (122). The peak load applied to the bone in vivo was simulated by applying a compressive displacement across the proximal disc while constraining axial displacement at the distal disc. The applied displacement resulted in a reaction force corresponding to the load magnitude applied in vivo (75N). Simulations were implemented using a custom parallelized finite

element code (121). Models consisted of 7.6 ± 0.5 million elements (mean \pm SD). The three principal strains and strain energy density in each element were determined.

3.2.3 Distribution of Osteocyte Lacunae

Images of each specimen were collected using nano-computed tomography (voxel size of $1.5\mu\text{m}$) to determine the locations of osteocyte lacunae in the proximal metaphysis (a volume of interest of 1.5 mm in height and diameter). Nano-computed tomography images were collected with 120V, 10W, 6s exposure time, and 3201 projections (Xradia Versa XRM-520, Zeiss, Dublin, CA). To improve image contrast, specimens were prepared by first removing the endplates, washing out marrow using centrifugation (6000rpm for 2 minutes followed by 8000rpm for 3 minutes at room temperature, Fisher Scientific accuSpin Micro R) and embedding in methyl methacrylate (see (125) for a complete embedding protocol).

Identification of individual lacunae in the three-dimensional images was performed using a local adaptive threshold (voxels with intensity 1.5 standard deviations below the mean were identified as possible lacunae) and followed by a size filter to remove objects too small ($< 27 \mu\text{m}^3$, 8 voxels) or too large ($> 1350 \mu\text{m}^3$, 400 voxels, a volume ~ 3.5 times larger than the volume of a lacunae) to be an osteocyte lacuna. Automated identification of osteocyte lacunae was validated by comparison to manual identification and achieved 92.9% true positives, 7.6% false positives, and 7.2% false negatives.

3.2.4 Distribution of Locations of Bone Formation

Regions of fluorescent bone formation markers were identified in three-dimensional fluorescent images obtained using serial milling. Serial milling is a fully automated, destructive imaging approach that involves repeatedly milling away 5 μ m from the top of the specimen and collecting images of the newly exposed specimen surface (125). Images were collected with a voxel size of 0.7 \times 0.7 \times 5.0 μ m, using three different fluorescent filter sets enabling examination of bone and two different bone formation markers. Bone was detected using a 350/420 nm excitation/emission filter set. Oxytetracycline was detected using a 390/560 nm excitation/emission filter set and calcein was detected using a 470/525 nm excitation/emission filter set. Image preprocessing and visualization was performed as described in prior publications (125). The use of two fluorescent markers made it possible to specify locations of bone formation initiating after applied mechanical loads. Oxytetracycline was applied immediately prior to mechanical stimulus and therefore indicates regions of bone formation that were active before in vivo mechanical loading. Calcein labels were applied after loading had initiated. Regions displaying calcein labels with neighboring oxytetracycline label indicate locations where bone formation had been ongoing prior to the applied mechanical stimulus and are referred to here as “background bone formation.” Locations of calcein label without neighboring oxytetracycline labels indicate bone formed only after mechanical stimulus and are referred to here as “mechanically-induced bone formation” (Fig. 3-2). Three-dimensional dynamic bone histomorphometry was performed to measure three-dimensional mineralizing surface (3D MS/BS), the number of bone formation sites, and the volume of bone formed after loading (FV/BV, formation volume fraction) (Fig. 3-3).

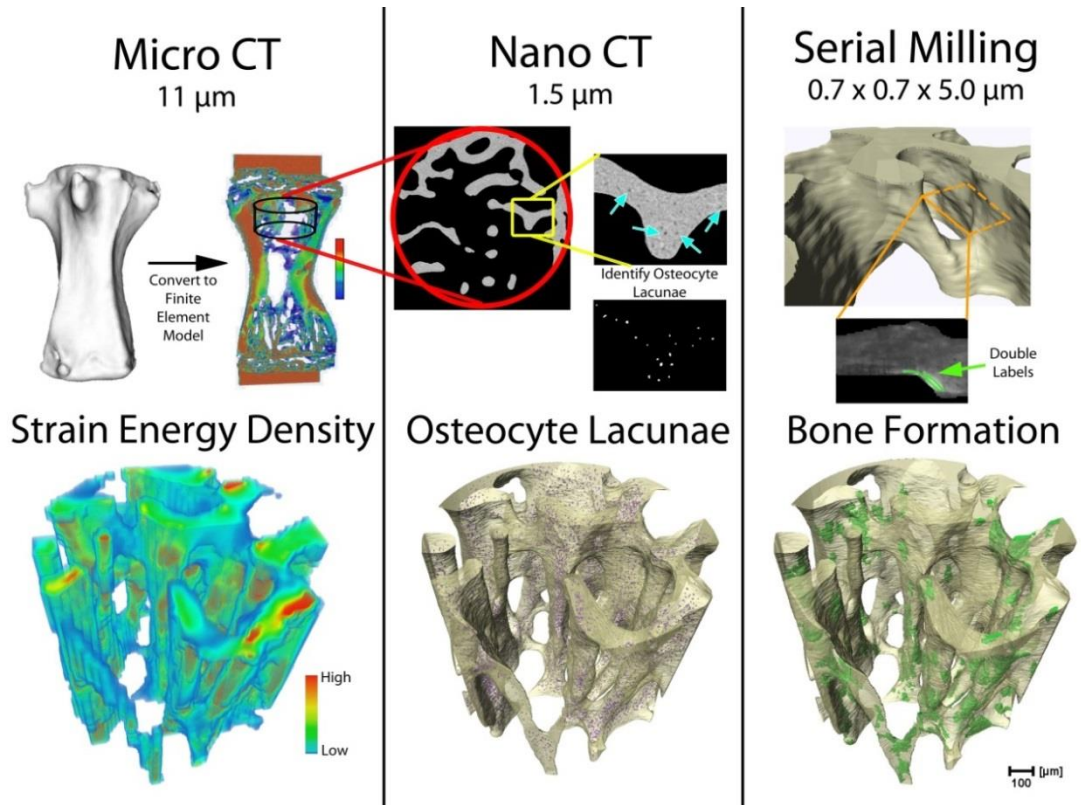


Figure 3-1: Three different imaging modalities were used to determine the local tissue stress and strain (shown here as strain energy density), the local cell density (osteocyte lacunar density), and the locations of bone formation.

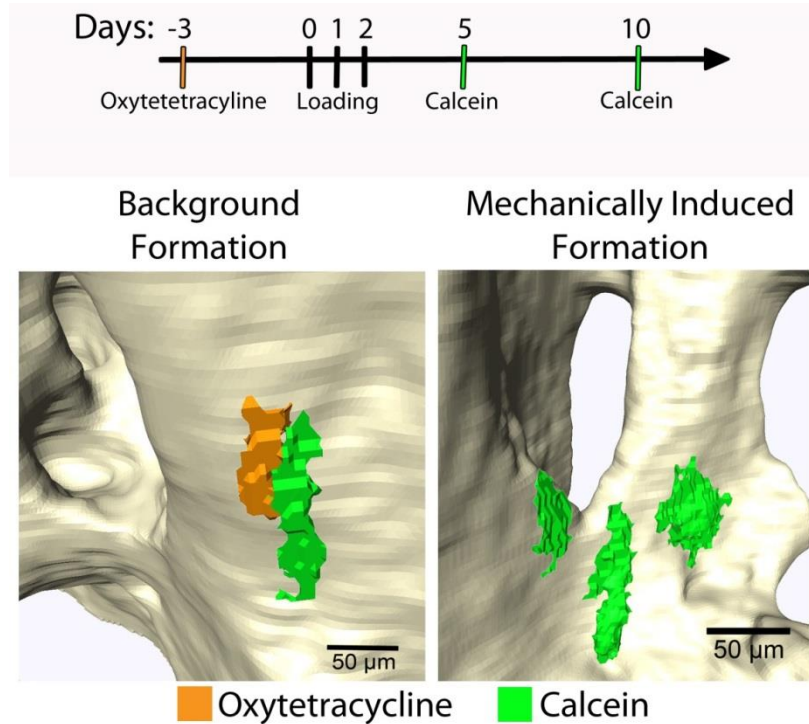


Figure 3-2: Oxytetracycline labels were administered prior to loading while calcein was applied after loading. Locations of bone formation that have both oxytetracycline and calcein are classified as background bone formation, as these sites were actively forming bone prior to mechanical loading. Sites of bone formation that show only calcein labeling are characterized as mechanically induced bone formation.

3.2.5 Spatial Associations between Bone Formation, Mechanical Strain, and Osteocyte Density

Three-dimensional representations of tissue stress/strain, osteocyte lacunae, and fluorescent markers of bone formation were registered using commercial software (AffineRegistration, AMIRA, v5.3.3, Visage Imaging, San Diego, CA). A region of interest present in all three imaging modalities (finite element model, nano-CT, and serial milling) was selected. The region consisted of a cylinder 1 mm in diameter and 1 mm in height and was located at least 1 mm away from the proximal growth plate.

Osteocyte lacunar density (Lc.Dn, $\#/mm^3$) was determined within each element of the finite element model.

We determined the probability of observing bone formation as a function of local tissue stress/strain (evaluated as strain energy density) and local osteocyte lacunar density. Probability of observing bone formation was determined as the number of bone surface voxels near a region of bone formation (within $22\mu m$, or one finite element) divided by the total number of bone surface voxels (84, 138). The probability of observing bone formation in each specimen was determined at 63 different combinations of strain energy density (SED) and osteocyte lacunar density spanning the range of SED and osteocyte lacunar density. Each assessment of the probability of observing bone formation used 40-500 surface voxels (8542 ± 1845 surface voxels per specimen, mean \pm SD). The relationship between probability of observing bone formation, tissue SED and osteocyte density was determined by fitting a three dimensional spline (n=8 data points per SED/osteocyte lacunar density combination). Multiple linear regression models were used to assess SED, osteocyte density and synergy between the two as a predictor of the probability of observing bone formation.

3.3 Results

Mechanical loading caused an increase in bone formation in cancellous bone. The volume of mechanically induced bone formed in the week after loading was 2-4 times greater in the loaded group than the control group (Fig. 3-3A-C). The amount of background bone formation (locations of bone formation active prior to application of

load) did not differ between loaded and control groups (Fig. 3-3D-F). Loading increased the number of sites of bone formation, but the size of formation sites was similar in loaded and control groups. Hence, the increase in bone formed after loading was primarily a result of an increase in the number of bone formation sites in loaded specimen (Fig. 3-3H). Bone volume fraction was slightly increased in the loaded group as compared to controls ($p = 0.09$).

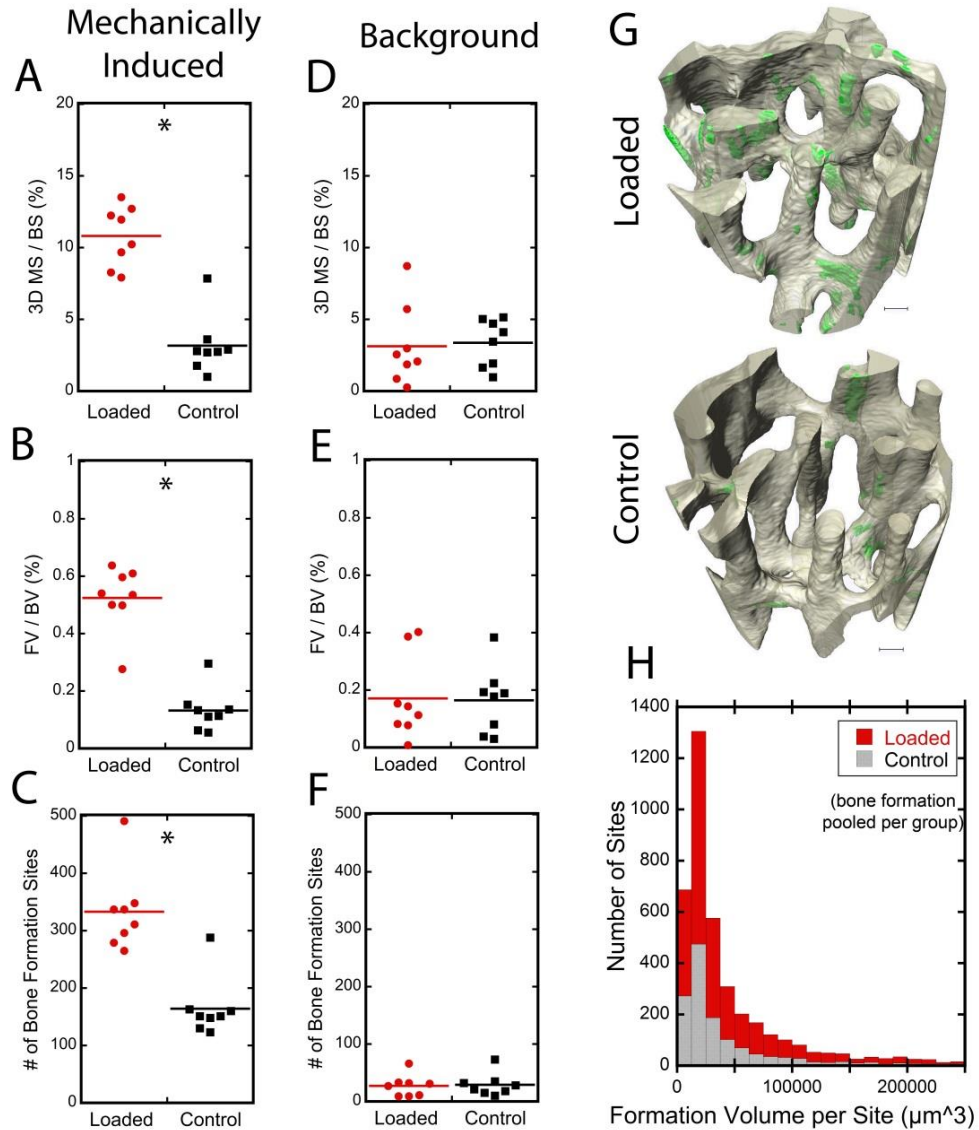


Figure 3-3: (A-C) The amount of mechanically induced bone formation was much greater in loaded bones as compared to controls. (D-F) Background bone formation (locations where bone formation was ongoing prior to applied mechanical loading) did not differ between the two groups. * $p < 0.0001$ (G) Representative regions of cancellous bone in a loaded and control specimen are shown. Scale bars represent $50\mu\text{m}$. (H) The distribution of formation event size is shown (all formation events in a group are pooled, $n=8$ animals per group). Loaded samples have more sites of bone formation, but the size of formation sites is similar in loaded and control groups.

The probability of observing mechanically induced bone formation was greater in regions with larger local mechanical stress/strain (evaluated as SED) but did not appear to be influenced by lacunar density (Fig 3-4A). Consideration of other assays of mechanical stress/strain (max principal, max shear, hydrostatic, and deviatoric stress) achieved similar results (data not shown). The probability of observing mechanically-induced bone formation did not differ across large ranges in osteocyte lacunar density (the 25th, 50th, and 75th percentiles of osteocyte density, Fig. 3-4B). The probability of observing background bone formation was much less than that for mechanically induced bone formation and was poorly correlated with tissue stress/strain and osteocyte lacunar density (Fig. 3-4C). Multiple linear regression models showed a strong effect of SED on probability of observing bone formation and only a minor synergy between SED and osteocyte lacunar density (Table 3-1). Osteocyte lacunar density by itself was not associated with the probability of observing bone formation. The average SED at surfaces where bone formed was greater than the average SED at non-forming surfaces (Fig. 3-5).

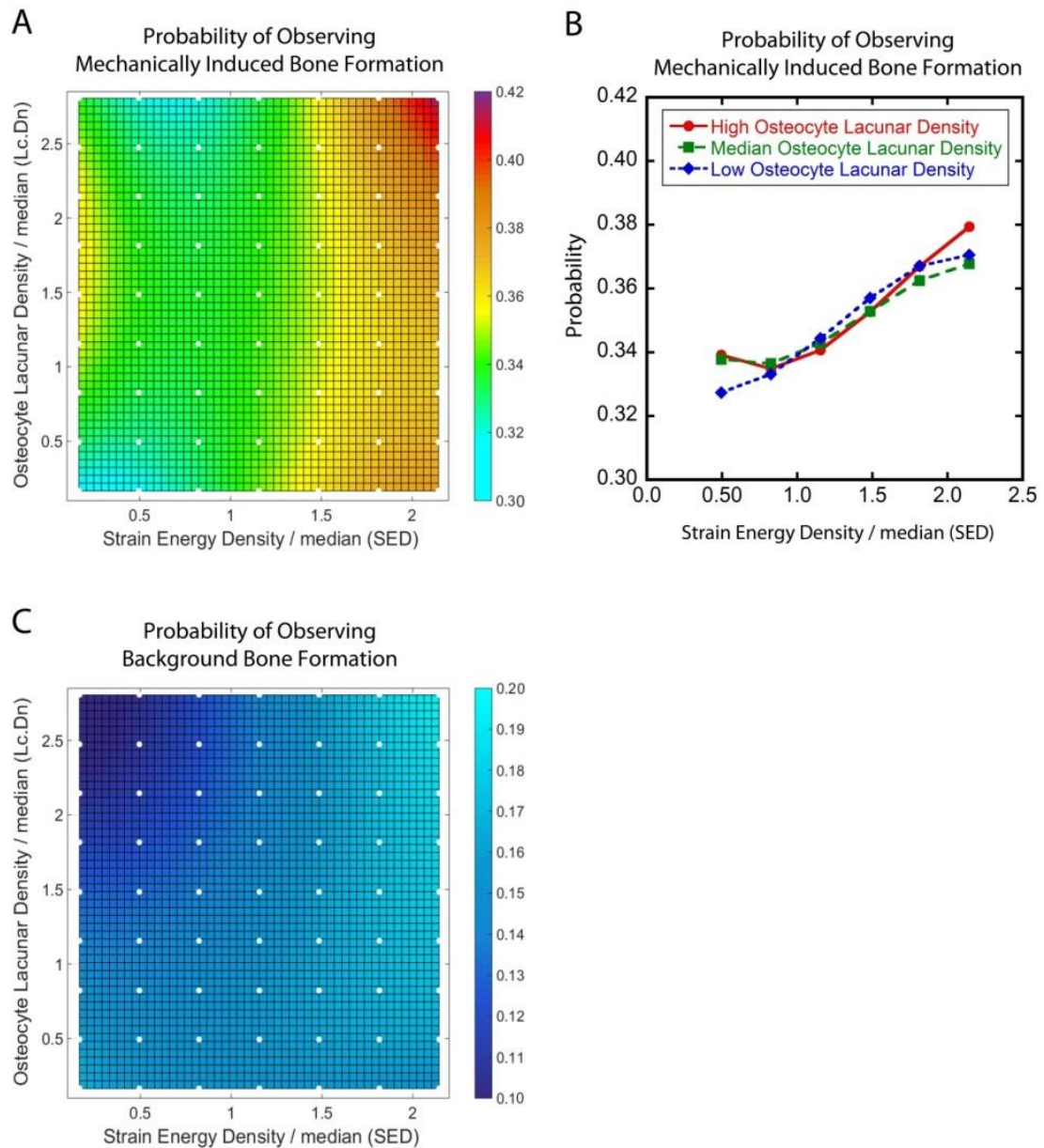


Figure 3-4: The probability of observing bone formation was determined at across the entire range of strain energy density and osteocyte lacunar density (white dots). The contour plots are generated with a spline fit to the results ($n=8$ samples at each white dot). (A) The probability of observing mechanically induced bone formation is greater when tissue strain energy density is larger and is independent of osteocyte lacunar density. (B) The probability of mechanically induced bone formation is positively correlated with SED and does not differ substantial when the calculation is limited to low (25th percentile), median (50th percentile), or high (75th percentile) osteocyte lacunar density. (C) The probability of observing background bone formation was much less than mechanically induced bone formation and was not correlated with SED.

Table 3-1: The multiple linear regression model relating the probability of observing bone formation to tissue strain energy density (SED) and lacunar density (Lc.Dn) is shown.

Term	Slope	p-value
SED	$C_1 = 0.048$	<0.0001
SED * Lc.Dn	$C_2 = 0.022$	<0.0001
Lc.Dn	$C_3 = -0.005$	0.124

$Probability = C_1 * SED + C_2 * SED * Lc.Dn + C_3 * Lc.Dn$

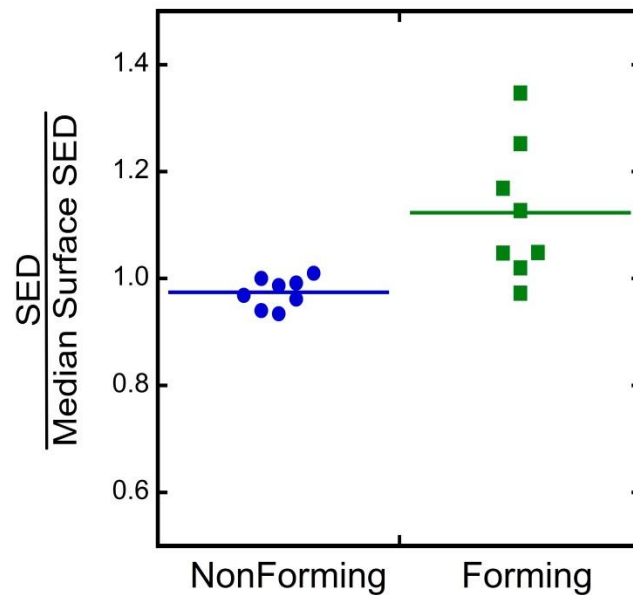


Figure 3-5: The strain energy density (SED) at non forming and forming surfaces is shown. A value greater than 1.0 indicates that SED at bone forming surfaces was greater than average SED throughout the cancellous bone structure.

Osteocyte lacunae were not uniformly distributed in cancellous bone.

Osteocyte lacunar density was larger in the center of trabeculae (depths greater than 22 μ m from the surface) than near bone surfaces (within 22 μ m of surface) (Fig. 3-6A).

The average lacunar density in newly formed bone was less than that in other regions

of cancellous bone (Table 3-2). Conversely, distributions of SED were similar on the surface and in the center of trabeculae (Fig. 3-6B).

Table 3-2. Osteocyte lacunar densities ($\times 10^3 \text{ \#/mm}^3$) in cancellous bone is shown (n=8).

Location	Mean \pm SD ($\times 10^3 \text{ \#/mm}^3$)	95% Confidence Interval
Entire Cancellous Bone Volume	71.9 \pm 16.4	(58.2, 85.6)
Near the Trabecular Surface (within 22 μm)	53.7 \pm 16.3	(40.0, 67.3)
Distant from Surface (more than 22 μm)	92.1 \pm 16.3	(78.6, 105.8)
Locations of New Bone Formation	43.6 \pm 16.0	(30.2, 56.9)

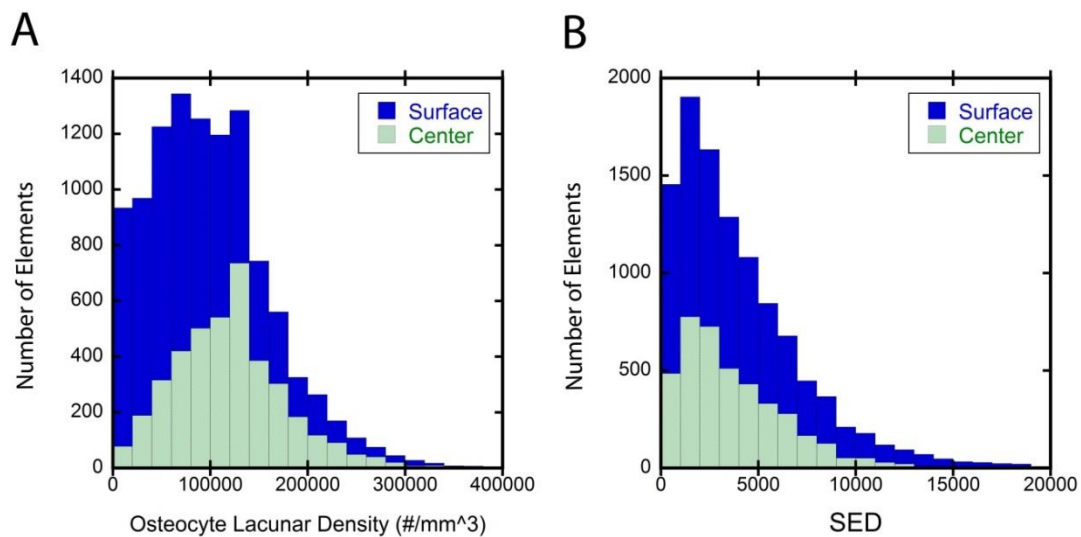


Figure 3-6: The distribution of osteocyte lacunar density and strain energy density (SED) throughout a single loaded specimen is shown. (A) The range in osteocyte lacunar density is greater on the surface of trabecular bone and includes many locations without osteocytes (density is zero). In the central regions of trabeculae, the mean osteocyte lacunar density is greater and there are few locations without osteocytes. (B) Although there are more surface regions within each specimen, the distribution of SED (median value and range) is similar on the surface and in the center of trabeculae.

3.4 Discussion

The objective of this study was to determine the influence of osteocyte density on mechanically induced bone formation and the spatial relationship between local tissue stress/strain and regions of mechanically induced bone formation. While mechanical stress and strain contributed to the prediction of locations of new bone formation, local osteocyte lacunar density was not associated with regions of new bone formation and did not influence the relationship between tissue stress and strain and the probability of observing new bone formation. Osteocyte lacunar density was reduced near trabecular surfaces and greater in the central regions of trabeculae. Hence, while local mechanical stress/strain influences the locations of mechanically-induced bone formation, the distribution of osteocytes (as measured by lacunar density) did not modulate the effect of tissue stress and strain.

Based on prior work establishing the role of osteocytes as sensors of bone tissue stress and strain we expected that regions of bone tissue with greater osteocyte density would be more sensitive to mechanical stimulation (85). We therefore expected regions of cancellous bone with greater osteocyte lacunar density to experience bone formation following more modest tissue stress/strain than other regions of cancellous bone and that accounting for osteocyte lacunar density would increase the ability to predict locations of bone formation as compared to predictions using tissue stress and strain alone. Instead we found that the locations of mechanically induced bone formation were not related to local osteocyte populations.

The current study contributes to a growing understanding of the relationship between loads on whole bones, bone tissue stress and strain and mechanically induced

bone formation. A correlation between bone formation and regions of increased tissue stress/strain was also observed in prior studies in mice (83, 84, 115, 137) and rats (138). In the current study the ability of tissue stress and strain to predict locations of bone formation did not exceed 41%, a value that is slightly larger than our prior work in rats (32%) (138) and is slightly smaller than that reported by others in mice (47%) (84). We attribute the increased predictive capacity of the current study, as compared to our prior study, to the identification of regions of bone formation that occurred after loading (mechanically induced bone formation). In comparison to prior work in mice, we attribute the small differences in probability of observing bone formation (41% as compared to 47%) to the duration of applied mechanical loading, which was only 3 days in the current study but 28-42 in the from the Müller lab.

Our finding that osteocyte density does not influence the locations of mechanically induced bone formation does not preclude the mechanosensory function of osteocytes. One possible explanation for our finding is that there is a minimum number of osteocytes necessary to initiate a new bone formation event and that there was a sufficient number of osteocytes located throughout cancellous bone in these animals. Osteocytes are known to respond to changes in interstitial fluid flow through mechanisms including fluid shear over the cell processes and cell body, deformation of tethering elements, and deflection of the primary cilia (34, 35, 38-40, 98, 139). Interstitial fluid flow occurs as a result of deformation of the surrounding bone tissue. While deformation of bone tissue drives interstitial fluid flow through the lacunar-canalicular network, the relationship between tissue stress/strain and fluid flow may not be linear and the locations of greatest tissue strain determined in the current study

may not necessarily be the locations of greatest fluid flow. A more detailed representation of the lacunar-canalicular network geometry and connectivity that accounts for the relationship between tissue strains and fluid shears would be needed to further clarify this effect. Additionally, recent computational models suggest that size and shape of the canaliculi affect fluid velocities and therefore the fluid shear stress experienced by an osteocyte (140, 141). Alignment and shape of osteocyte lacunae have also been shown to effect the stresses experienced by osteocytes(142). It is possible that these nano-scale aspects of geometry within the lacunar-canalicular system may be more influential in determining the locations of mechanically induced bone formation than the number of osteocytes alone.

In addition to the potential influence of interstitial fluid flow in the canalicular network, fluid shear and pressure in bone marrow has also been identified as a contributor to bone mechanotransduction (113). Physiologic loading leads to fluctuations in fluid pressure and shear within bone marrow. Marrow pressurization has been shown to be osteogenic even in the absence of strains in surrounding bone tissues (113). A recent analysis of regions of mechanically induced bone formation in the rodent tail found that stress/strain within the bone marrow was more strongly correlated with locations of new bone formation than stress and strain within the mineralized tissue (115). Computational models of bone marrow have estimated that fluid shear is of sufficient magnitude to induce an osteogenic response of marrow resident cells (111, 143-145).

There are several strengths to the current work. First, the current study is novel in using three-dimensional imaging to examine the spatial relationships between tissue

stress/strain, osteocyte lacunar density, and bone formation. The high resolutions of the imaging modalities made it possible to detect osteocyte lacunae and to measure newly formed bone volume soon after load application (within 7 days). Prior work examining the spatial locations of bone formation in cancellous bone has used serial in vivo micro-computed tomography imaging, which is currently limited in resolution (10.5 μ m voxels) and is therefore unable to localize osteocytes or detect small changes in bone volume, requiring the use of studies lasting 4 weeks or longer. Measures of bone formation were performed using three-dimensional images of fluorescent markers (the gold standard) an approach that made it possible to separate bone formation occurring after applied loading from bone formation that was already active before loading. Lastly, the in vivo loading model we used (the rodent tail loading model) achieves highly repeatable distributions of tissue stress and strain throughout cancellous bone (117), providing confidence regarding the co-localization of tissue stress/strain, osteocyte density, and bone formation.

There are also several limitations to consider when interpreting our results. Nano-CT was used to identify the locations of osteocyte lacunae but the technique cannot confirm that a lacuna was occupied by a viable osteocyte. However, young animals have high rates of occupancy in lacunae and given the relatively young age of the animals (6 month old rats) we expect most of the lacunae to be occupied. Indeed, the osteocyte lacunar density in this study ($71.9 \pm 16.4 \times 10^3 \text{ \#/mm}^3$) is similar to measures of osteocyte density in rats ($93.2 \pm 5.4 \times 10^3 \text{ \#/mm}^3$) (146). Second, the finite element models used in the current study were homogeneous linear elastic models and were performed at a lower resolution (finite element size of 22 μ m) than imaging of

osteocyte lacunae or bone formation. As mentioned above, this resolution is not able to characterize stress concentrations around osteocyte lacunae. However, the finite element model resolution was sufficient to achieve at least 4 elements across the width of a trabecula, which has been shown to be adequate (120, 121). Future improvements in computational power would allow for the use of higher resolution finite element models, inclusion of tissue heterogeneity, and tissue nonlinearities may further improve assessment of tissue stress/strain.

An additional limitation is that the analysis only examined osteocytes and stress/strain at the surface and did not account for osteocytes distant from the bone surface. In a theoretical model developed to test the influence of osteocytes on mechanical adaptation in cancellous bone, Huiskes and colleagues simulated bone formation based on an “osteoblast recruitment stimulus” a theoretical parameter calculated as a summation of mechanical stress/strain, osteocyte density, and the distance between osteocytes and trabecular bone surfaces. To consider osteocytes distant from the bone surface we performed an additional analysis using the “osteoblast recruitment stimulus” which incorporates all osteocytes throughout cancellous bone and found that osteoblast recruitment stimulus was not correlated with the probability of observing bone formation (see Supplementary Materials). Hence, consideration of osteocytes at locations other than the surface voxels is unlikely to influence our conclusion.

Our study supports the idea that locations of bone formation are regulated by the mechanical stimulus. The fact that local osteocyte lacunar density did not influence regions of mechanically induced bone formation highlights the potential importance of

more detailed aspects of the lacunar-canalicular system including interstitial fluid flow, osteocyte size and connectivity as well as fluid flow and pressure in the marrow space. Identification of the mechanotransduction mechanisms that are most influential in bone mechanical adaptation will help to identify the signaling mechanism most important and most attractive for treatment strategies.

3.5 Supplemental Material

3.5.1 Osteoblast Recruitment Stimulus

The osteoblast recruitment stimulus is a theoretical parameter used by Huiskes and colleagues in computational models of trabecular bone adaptation that accounted for both the distribution of strain energy density and osteocytes. The parameter was calculated as follows:

$$P(x) = \sum_{i=1}^n f_i(x) * R_i , \quad (1)$$

where $P(x)$ is the osteoblast recruitment stimulus at location x within the trabecular microstructure, n is the number of osteocytes and R_i is the strain energy density experienced by osteocyte i . An exponential decay function, f_i , models the diffusion of mechanotransduction signals away from each osteocyte.

In our study, strain energy density was used as the mechanical stimulus at every osteocyte lacuna. The decay function was modeled such that an osteocyte's effect was limited to 50 μ m from the osteocyte lacunae (a parametric analysis on the distance of signal diffusion did not change the relation between osteoblast recruitment stimulus and the probability of bone formation).

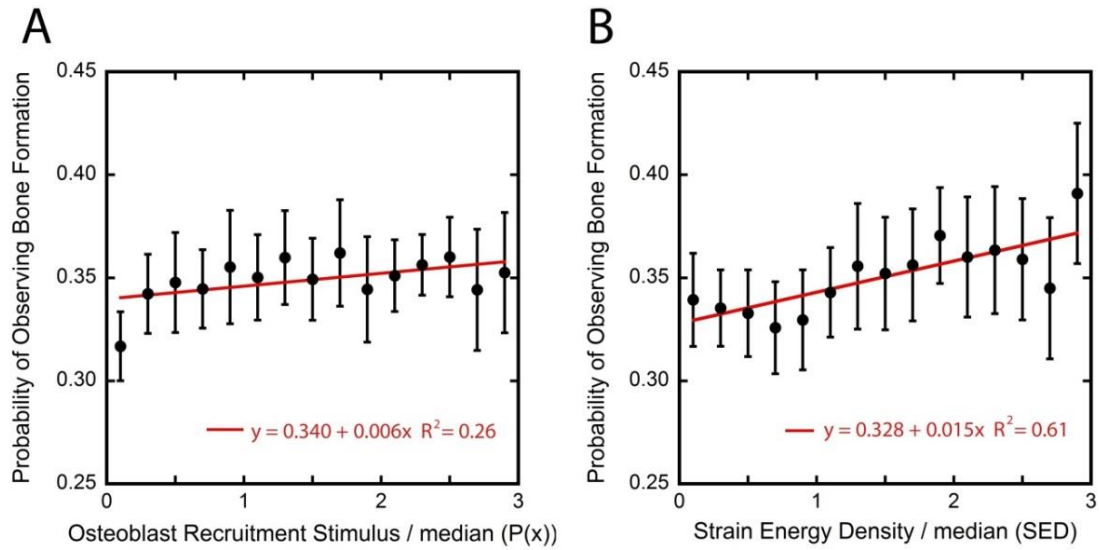


Figure 3-7: (A) The probability of bone formation does not increase with osteoblast recruitment stimulus. (B) The probability of bone formation is more strongly correlated to surface SED than osteoblast recruitment stimulus.

3.5.2 Bone Volume Fraction

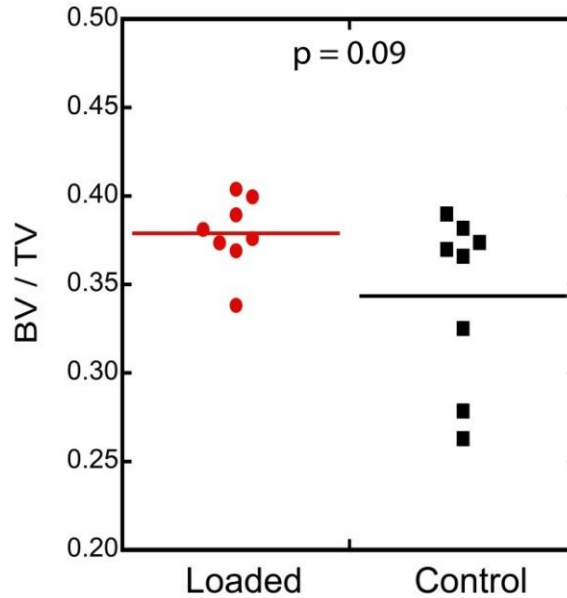


Figure 3-8: Average bone volume fraction one week after loading was slightly greater in the loaded animals as compared to controls ($p = 0.09$).

REFERENCES

10. Cowin S, editor. Bone Mechanics Handbook. 2 ed. Boca Raton: CRC Press; 2001.
20. Torrance AG, Mosley JR, Suswillo RF, Lanyon LE. Noninvasive loading of the rat ulna in vivo induces a strain-related modeling response uncomplicated by trauma or periosteal pressure. *Calcified Tissue International*. 1994;54(3):241-7.
21. Kotha SP, Hsieh YF, Strigel RM, Muller R, Silva MJ. Experimental and finite element analysis of the rat ulnar loading model-correlations between strain and bone formation following fatigue loading. *Journal of Biomechanics*. 2004;37(4):541-8.
33. Parfitt AM, editor. Bone-forming cells in clinical conditions. Boca Raton, FL: Telford Press and CRC Press; 1990.
34. Schaffler MB, Kennedy OD. Osteocyte signaling in bone. *Current osteoporosis reports*. 2012;10(2):118-25.
35. Bonewald LF. The amazing osteocyte. *Journal of Bone and Mineral Research*. 2011;26(2):229-38.
38. Temiyasathit S, Jacobs CR. The osteocyte primary cilium and its role in bone mechanotransduction. *Annals of the New York Academy of Sciences*. 2010;1192:422-8.
39. Coughlin TR, Voisin M, Schaffler MB, Niebur GL, McNamara LM. Primary Cilia Exist in a Small Fraction of Cells in Trabecular Bone and Marrow. *Calcified Tissue International*. 2015;96(1):65-72.
40. McNamara LM, Majeska RJ, Weinbaum S, Friedrich V, Schaffler MB. Attachment of Osteocyte Cell Processes to the Bone Matrix. *The Anatomical Record: Advances in Integrative Anatomy and Evolutionary Biology*. 2009;292(3):355-63.
41. McGarry JG, Klein-Nulend, Jenneke, Prendergast, Patrick J. The effect of cytoskeletal disruption on pulsatile fluid flow-induced nitric oxide and prostaglandin E2 release in osteocytes and osteoblasts. *Biochemical and Biophysical Research Communications*. 2005;330(1):341-8.

42. Ponik SM, Triplett, Jason W., Pavalko, Fredrick M. Osteoblasts and osteocytes respond differently to oscillatory and unidirectional fluid flow profiles. *Journal of Cellular Biochemistry*. 2007;100(3):794-807.
43. Vatsa A, Smit TH, Klein-Nulend J. Extracellular NO signalling from a mechanically stimulated osteocyte. *J Biomech*. 2007;40, Supplement 1:S89-S95.
44. Bacabac RG, Mizuno, Daisuke, Schmidt, Christoph F., MacKintosh, Fred C., Van Loon, Jack J. W. A., Klein-Nulend, Jenneke, Smit, Theo H. Round versus flat: Bone cell morphology, elasticity, and mechanosensing. *Journal of Biomechanics*. 2008;41(7):1590-8.
45. Li X, Zhange, Y., Kang, H., Lui, W., Lui, P., Zhang, J., Harris, S. E., Wu, D. Sclerostin Binds to LRP5/6 and Antagonizes Canonical Wnt Signaling. *Journal of Biological Chemistry*. 2005;280:19883-7.
46. Li J, Sarosi, Ildiko, Cattley, Russell C., Pretorius, James, Asuncion, Frank, Grisanti, Mario, Morony, Sean, Adamu, Stephen, Geng, Zhaopo, Qiu, Wanrong, Kostenuik, Paul, Lacey, David L., Simonet, W. Scott, Bolon, Brad, Qian, Xueming, Shalhoub, Victoria, Ominsky, Michael S., Zhu Ke, Hua, Li, Xiaodong, Richards, William G. Dkk1-mediated inhibition of Wnt signaling in bone results in osteopenia. *Bone*. 2006;39(4):754-66.
47. Robling AG, Niziolek, P. J., Baldridge, L. A., Condon, K. W., Allen, M. R., Alam, I., Mantila, S. M., Gluhak-Heinrich, J., Bellido, T. M., Harris, S. E., Turner, C. H. Mechanical Stimulation of Bone in vivo Reduces Osteocyte Expression of Sost/Sclerostin. *Journal of Biological Chemistry*. 2008;283:5866-75.
48. Plotkin LI, Bellido T. Osteocytic signalling pathways as therapeutic targets for bone fragility. *Nat Rev Endocrinol*. 2016;12(10):593-605.
54. Jones HH, Priest JD, Hayes WC, Tichenor CC, Nagel DA. Humeral hypertrophy in response to exercise. *J Bone Joint Surg*. 1977;59:204-8.
61. Goodship AE, Lanyon LE, McFie H. Functional adaptation of bone to increased stress. An experimental study. *The Journal of Bone and Joint Surgery*. 1979;61(4):539-46.
62. Lanyon LE, Goodship AE, Pye C, McFie H. Mechanically adaptive bone remodeling: a quantitative study on functional adaptation in the radius following ulna osteotomy in sheep. *Journal of Biomechanics*. 1982;15:141-54.

63. Churches AEH, C. R. . Functional Adaptation of Bone in Response to Sinusoidally Varying Controlled Compressive Loading of the Ovine Metacarpus. *Clinical Orthopaedics & Related Research*. 1982;168:265-80.
64. Rubin CT, Lanyon LE. Regulation of bone mass by mechanical strain magnitude. *Calcif Tissue Int*. 1985;37(4):411-7.
66. Goldstein SA, Matthews LS, Kuhn JL, Hollister SJ. Trabecular bone remodeling: an experimental model. *Journal of Biomechanics*. 1991;1(135):135-50.
67. van der Meulen MC, Morgan TG, Yang X, Baldini TH, Myers ER, Wright TM, et al. Cancellous bone adaptation to in vivo loading in a rabbit model. *Bone*. 2006;38(6):871-7.
68. Chambers TJ, Evans M, Gardner TN, Turner-Smith A, Chow JW. Induction of bone formation in rat tail vertebrae by mechanical loading. *Bone Miner*. 1993;20(2):167-78.
69. Chow JW, Jagger CJ, Chambers TJ. Characterization of osteogenic response to mechanical stimulation in cancellous bone of rat caudal vertebrae. *American Journal of Physiology*. 1993;265(2 Pt 1):E340-7.
70. Webster DJ, Morley PL, van Lenthe GH, Muller R. A novel in vivo mouse model for mechanically stimulated bone adaptation--a combined experimental and computational validation study. *Computer Methods in Biomechanics and Biomedical Engineering*. 2008;11(5):435-41.
72. De Souza RL, Matsuura M, Eckstein F, Rawlinson SC, Lanyon LE, Pitsillides AA. Non-invasive axial loading of mouse tibiae increases cortical bone formation and modifies trabecular organization: a new model to study cortical and cancellous compartments in a single loaded element. *Bone*. 2005;37(6):810-8.
73. Fritton JC, Myers ER, Wright TM, van der Meulen MC. Loading induces site-specific increases in mineral content assessed by microcomputed tomography of the mouse tibia. *Bone*. 2005;36(6):1030-8.
77. Hsieh Y, Turner CH. Effects of loading frequency on mechanically induced bone formation. *Journal of Bone and Mineral Research*. 2001;16(5):918-24.
78. Robling AG, Burr DB, Turner CH. Partitioning a Daily Mechanical Stimulus into Discrete Loading Bouts Improves the Osteogenic Response to Loading. *Journal of Bone and Mineral Research*. 2000;15(8):1596-602.

83. Webster D, Wirth A, van Lenthe GH, Muller R. Experimental and finite element analysis of the mouse caudal vertebrae loading model: prediction of cortical and trabecular bone adaptation. *Biomechanics and Modeling in Mechanobiology*. 2012;11(1-2):221-30.
84. Schulte FA, Ruffoni, D., Lambers, F. M., Christen, D., Webster, D. J., Kuhn, G., Muller, R. Local mechanical stimuli regulate bone formation and resorption in mice at the tissue level. *PloS one*. 2013;8(4):e62172.
85. Huiskes R, Ruimerman R, van Lenthe GH, Janssen JD. Effects of mechanical forces on maintenance and adaptation of form in trabecular bone. *Nature*. 2000;405(6787):704-6.
88. Kelly NH, Schimenti JC, Ross FP, van der Meulen MCH. Transcriptional profiling of cortical versus cancellous bone from mechanically-loaded murine tibiae reveals differential gene expression. *Bone*. 2016;86:22-9.
98. Jacobs CR, Temiyasathit S, Castillo AB. Osteocyte mechanobiology and pericellular mechanics. *Annual Review of Biomedical Engineering*. 2010;12:369-400.
111. Metzger TA, Kreipke TC, Vaughan TJ, McNamara LM, Niebur GL. The In Situ Mechanics of Trabecular Bone Marrow: The Potential for Mechanobiological Response. *Journal of Biomechanical Engineering*. 2015;137(1):011006-.
113. Kwon RY, Meays DR, Tang WJ, Frangos JA. Microfluidic enhancement of intramedullary pressure increases interstitial fluid flow and inhibits bone loss in hindlimb suspended mice. *Journal of Bone and Mineral Research* 2010;25(8):1798-807.
115. Webster D, Schulte FA, Lambers FM, Kuhn G, Müller R. Strain energy density gradients in bone marrow predict osteoblast and osteoclast activity: A finite element study. *Journal of Biomechanics*. 2015;48(5):866-74.
116. Guo XE, Eichler MJ, Takai E, Kim CH. Quantification of a rat tail vertebra model for trabecular bone adaptation studies. *Journal of Biomechanics* 2002;35(3):363-8.
117. Goff MG, Chang KL, Litts EN, Hernandez CJ. The effects of misalignment during in vivo loading of bone: techniques to detect the proximity of objects in three-dimensional models. *Journal of Biomechanics*. 2014;47(12):3156-61.

120. Guldberg RE, Hollister SJ, Charras GT. The accuracy of digital image-based finite element models. *Journal of Biomechanical Engineering*. 1998;120(4):289-95.
121. Niebur GL, Yuen JC, Hsia AC, Keaveny TM. Convergence behavior of high-resolution finite element models of trabecular bone. *Journal of Biomechanical Engineering*. 1999;121(6):629-35.
122. Elliott AM, Sarver JJ. Validation of the Mouse and Rat Disc as Mechanical Models of the Human Lumbar Disc. *SPINE*. 2004;29(7):713-22.
125. Slyfield CR, Tkachenko EV, Wilson DL, Hernandez CJ. Three-dimensional dynamic bone histomorphometry. *Journal of Bone and Mineral Research*. 2012;27(2):486-95.
134. Melville KM, Kelly NH, Surita G, Buchalter DB, Schimenti JC, Main RP, et al. Effects of Deletion of ER α in Osteoblast-Lineage Cells on Bone Mass and Adaptation to Mechanical Loading Differ in Female and Male Mice. *Journal of Bone and Mineral Research*. 2015;30(8):1468-80.
135. Fritton JC, Myers ER, Wright TM, van der Meulen MC. Bone mass is preserved and cancellous architecture altered due to cyclic loading of the mouse tibia after orchidectomy. *Journal of bone and mineral research*. 2008;23(5):663-71.
136. Hayes W, Snyder B, editors. *Towards a Quantitative Formulation of Wolff's Law in Trabecular Bone* 1981.
137. Lambers FM, Kuhn G, Weigt C, Koch KM, Schulte FA, Müller R. Bone adaptation to cyclic loading in murine caudal vertebrae is maintained with age and directly correlated to the local micromechanical environment. *Journal of Biomechanics*. 2015;48(6):1179-87.
138. Cresswell EN, Goff, M. G., Nguyen, T. M., Lee, W. X., Hernandez, C. J. Spatial relationships between bone formation and mechanical stress within cancellous bone. *Journal of Biomechanics*. 2016;49(2):222-8.
139. Klein-Nulend J, van der Plas A, Semeins CM, Ajubi NE, Frangos JA, Nijweide PJ, et al. Sensitivity of osteocytes to biomechanical stress in vitro. *FASEB J*. 1995;9(5):441-5.
140. Verbruggen SW, Vaughan TJ, McNamara LM. Fluid flow in the osteocyte mechanical environment: a fluid–structure interaction approach. *Biomechanics and Modeling in Mechanobiology*. 2014;13(1):85-97.

141. Verbruggen SW, Vaughan TJ, McNamara LM. Mechanisms of osteocyte stimulation in osteoporosis. *J Mech Behav Biomed Mater.* 2016;62:158-68.
142. McNamara LM, van der Linden JC, Weinans H, Prendergast PJ. Stress-concentrating effect of resorption lacunae in trabecular bone. *Journal of Biomechanics.* 2006;39(4):734-41.
143. McAllister TN, Du T, Frangos JA. Fluid Shear Stress Stimulates Prostaglandin and Nitric Oxide Release in Bone Marrow-Derived Preosteoclast-like Cells. *Biochemical and Biophysical Research Communications.* 2000;270(2):643-8.
144. Castillo AB, Jacobs CR. Mesenchymal Stem Cell Mechanobiology. *Current Osteoporosis Reports.* 2010;8(2):98-104.
145. Soves CP, Miller JD, Begun DL, Taichman RS, Hankenson KD, Goldstein SA. Megakaryocytes are mechanically responsive and influence osteoblast proliferation and differentiation. *Bone.* 2014;66:111-20.
146. Mullender MG, Huiskes R, Versleyen H, Buma P. Osteocyte density and histomorphometric parameters in cancellous bone of the proximal femur in five mammalian species. *Journal of Orthopaedic Research.* 1996;14(6):972-9.

CHAPTER 4

EXERCISE INDUCED MORPHOLOGICAL CHANGES IN RACEHORSES

The following chapter is preliminary data used to evaluate if difference in bone morphology could be identified using micro computed tomography. Given the significant findings in this preliminary study, a larger study will be conducted. We plan to publish the larger work in the Equine Veterinarian Journal. The preliminary data was submitted to the Orthopedic Research Society and will be presented in poster form at the 2017 annual Conference.

4.1 Introduction

Fracture of the proximal sesamoid bone is the most common fatal musculoskeletal injury in racehorses (102-104). Fracture occurs during a race, and commonly results in a fall that is lethal for the horse and dangerous for the jockey. Understanding fracture pathology will allow us to determine fracture risk, which would allow racetrack personnel to make informed decisions about training and racing, and thereby reduce the risk of fatal injury during races.

Alterations in the morphology of the proximal sesamoid bones and the adjacent third metacarpal have been associated with fracture risk. In the proximal sesamoid bone, increased bone mineral density and decreased porosity has been observed in racehorses that sustain a sesamoid bone fracture (97, 147, 148). Additionally, alterations in bone geometry, the presence of large vascular channels and osteophytes

in the sesamoid bones have also been associated with decreased fracture risk (149, 150). Abnormalities in magnetic resonance images known as bone marrow lesions have been observed in the third metacarpal bone in horses that subsequently sustain a proximal sesamoid fracture (97). These lesions appear on the surface articulating with the proximal sesamoid bones and are associated with subchondral thickening of the proximal sesamoid bones (97). Therefore, it appears that changes occur in sesamoid bones prior to fracture, however it's unclear what changes are most important for predicting fracture risk.

In racehorses, distance, speed and number of high speed training and racing workouts have been used to determine associations between exercise and fracture risk. High speed exercise is defined as galloping workouts. The time and distance of each galloping workout is recorded. Distance and running speed have been positively associated with risk of fracture, particularly when large amounts of training and racing occur within a 30-day period (105). In contrast, racehorses that sustained a variety of musculoskeletal injuries had significantly less high speed exercise in the four to eight weeks leading up to a fracture (106). A recent analysis of the proximal sesamoid bone found that the odds ratio of fracture increases with more time in active training, more high speed exercise and races, and longer accrued distances run (107).

While some details of high speed exercise and bone morphology have been associated with increased fracture risk, the link between exercise altering bone morphology to increase fracture risk has not been studied. Excessive exercise associated with race training changes bone morphology increasing bone density (90, 91). However, increased bone density has been associated with increased fracture risk

(97, 147, 148). We believe exercise influences fracture risk by altering bone morphology. To date, exercise histories have not been correlated with changes in bone morphology observed in proximal sesamoid fracture. Therefore, a better understanding of the relationship between exercise history and changes in bone morphology could explain why some animals have a higher risk of proximal sesamoid bone fracture.

Altered bone morphology, bone internal structure, and altered tissue material properties influence whole bone strength and contribute to fracture risk. Histology has indicated decreased bone porosity (95) in fractured proximal sesamoid bones, but we do not yet know how three-dimensional architecture and geometry is altered in fractured sesamoid bones. To date, no studies of bone tissue material properties exist in animals that experienced a fracture. Changes in bone tissue material properties such as excessive tissue degree of mineralization promote bone fragility and increase fracture risk (151). Radiographs of proximal sesamoid bones have been used, but are not a reliable measure of bone mineral content of the entire bone and do not differentiate between increased bone volume and alterations in tissue degree of mineralization. It remains unclear how changes in bone morphology and material properties are related to exercise history.

The long-term goal of this line of investigation is to identify methods of preventing catastrophic proximal sesamoid bone fracture in racehorses. In this study, we determined: 1) the changes in bone internal and external morphology that are associated with fracture and 2) differences in exercise history between racehorses that experience fracture and non-fractured controls.

4.2 Methods

4.2.1 Sample Data

Proximal sesamoid bones were collected from Thoroughbred racehorses following necropsy as required by the New York State Gaming Commission. Animal age ranged from 3-8 years and included males and females (see Table 4-1 for age and weight). Horses in the fracture group had experienced a fracture of one or both proximal sesamoid bones in one forelimb while bones in the contralateral limb remained intact (n=4, 3 left limb fractures, 1 right limb fracture). Bones were harvested from both forelimbs. In the four fractured limbs, 3 horses sustained fracture to both the medial and lateral proximal sesamoid bones, while 1 horse fractured only the lateral proximal sesamoid bone, therefore providing 7 fractured sesamoid bones, 1 intact sesamoid in a limb that fractured, and 8 intact sesamoid bones from contralateral limbs. Within the sesamoids, fractures occurred primarily in the basilar region (4 of the 7 fractured proximal sesamoid bones), with 2 observed mid-body fractures, and 1 apical fracture.

Proximal sesamoid bones were also harvested from four racehorses that were euthanized due to disease or injury not pertaining to proximal sesamoid bones to serve as sex-and age-matched controls. Causes of death included cervical fracture, suspensory ligament failure, cardiovascular collapse, and infection. Where available, two proximal sesamoid bones were collected from each limb, yielding 14 proximal sesamoid bones.

Table 4-1. Thoroughbred racehorse demographics

Group	Age (years)	Sex	Weight (kg)	Racing Career Duration (weeks)	Age at Start of Career (years)
Fractured	4	Gelding	488	84	2
Fractured	7	Gelding	538	231	2
Fractured	8	Mare	400	194	4
Fractured	4	Mare	492	138	2
Control	7	Stallion	476	240	2
Control	3	Mare	516	67	2
Control	4	Mare	470	104	3
Control	5	Mare	414	134	2

4.2.2 Image Acquisition and Processing

Images of proximal sesamoid bones (n = 30) were collected using high resolution micro-computed tomography at a voxel size of 50 μ m (GE scanner, 720 projection, 20ms exposure time, 100kV, 50mA, representative micro-CT images for each group are shown in Fig 4-1). Scans were acquired with a calibration phantom of known density, to allow determination of average tissue mineral density (TMD). Local adaptive thresholding techniques were used to segment bone (identified voxels as bone if the intensity was greater than 0.75 standard deviations below the mean in a local window of 2.5mm, Fig 4-2).

apical, mid-body, basilar, subchondral, medullary, and flexor (a total of 9 different sub-regions, Fig 4-3B). Fractured proximal sesamoid bones caused alterations in bone morphology limiting analysis of sub-regions to the contralateral limbs. Contralateral limbs provided a within-individual assay of loading history and therefore would have similar morphological changes as fractured bones. Tissue mineral density (TMD) was calculated in the whole bone, and in the nine sub-regions. Measurements of internal structure, trabecular thickness (Tb.Th) and degree of anisotropy (DA), were measured using BoneJ. Degree of anisotropy ranges from isotropic (0) to anisotropic (1). To isolate the internal bone structure, 2.5mm thick of the outer shell was removed. From three-dimensional renderings of the whole bone, the presence of osteophytes at the apical and basilar subchondral margin were counted.

4.2.3 History of Training and Racing Exercise

The history of training and racing exercise in each racehorse was determined using information provided by the New York State Gaming Commission. Exercise history reports include documentation of every high speed training and racing exercise. High speed exercise is defined as any exercise session in which an animal runs a distance of one furlong in 14 seconds or faster (~14.3 m/s or faster). Distance run during high speed exercise, number of races, average training/racing distance, and average training/racing time were compared between animals that sustained a proximal sesamoid bone fracture and sex/age matched controls. In addition to recording workouts, exercise history reports also include weeks of rest. The work-to-rest ratio is a measure of activity that is determined as the total number of weeks in

which any high speed exercise was performed divided by the number of rest weeks (weeks in which no high speed exercise were performed). The work-to-rest ratio was reported for the entire career of the racehorse as well as the 12 weeks prior to death. Additionally, the number of consecutive weeks with or without high speed exercise was determined. Lastly, the work-to-race ratio was determined as the total distance run in training divided by the total distance raced over the 12 week period prior to death.

4.2.4 Statistics

As no differences in bone internal or external morphology were observed between medial and lateral sesamoid bones within a limb or between left and right limbs, bones were pooled into fracture and control groups for statistical analysis. Mean differences in bone volume fraction (BV/TV) and tissue mineral density (TMD) per region are reported. A t-test with unequal variance was used to determine significant changes between groups. Data reported is mean \pm SD. Statistical significance was $p < 0.05$.

4.3 Results

4.3.1 Morphological Changes

Bone volume fraction was greater in the proximal sesamoid bones of the fracture group ($91.24 \pm 2.56\%$) than sesamoid bones from controls ($87.04 \pm 1.74\%$, Fig 4-3A). Regional differences in BV/TV were also observed; the bone volume fraction within each region was greater in the fracture group. The basilar region (the region

where fracture was most often observed) showed the greatest difference in bone volume fraction from control bones (Fig 4-3C).

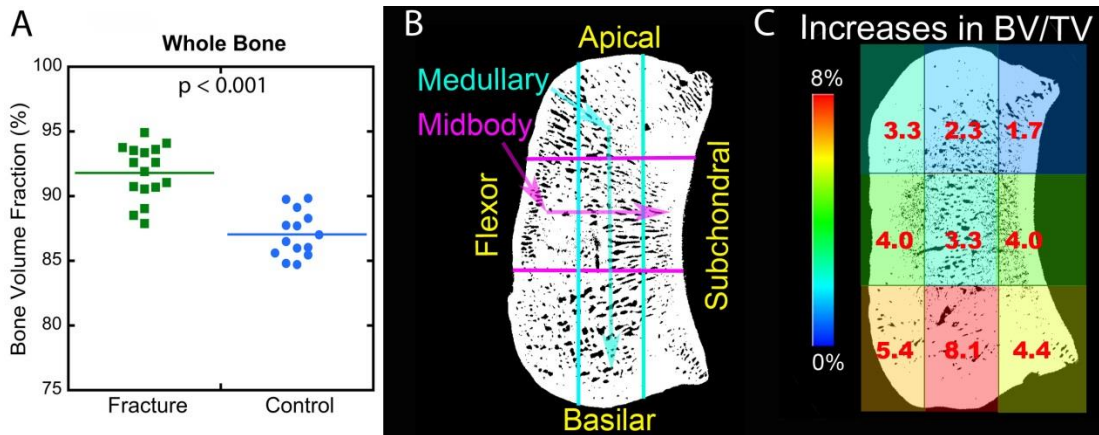


Figure 4-3: (A) The bone volume fraction was greater in the fracture group. (B) Nine sub-regions within the bone were defined. (C) Bone volume fraction within sub-regions was greater in the fracture group than controls. The greatest increase in bone volume fraction occurred in the basilar region.

Tissue mineral density (TMD) measured throughout the whole bone was not different between the fracture ($1027.4 \pm 64.0 \text{ mg/cm}^3$) and control groups ($1027.2 \pm 127.1 \text{ mg/cm}^3$). No differences were observed in the regional TMD between groups at any sub-region. Trabecular thickness was greater in racehorses that sustained a fracture ($819.0 \pm 85.7 \text{ } \mu\text{m}$) than the control group ($657.1 \pm 74.0 \text{ } \mu\text{m}$, $p=0.0006$). There was a trend toward differences in the degree of anisotropy ($p=0.06$) with the fractured group slightly more isotropic than controls (0.33 ± 0.11 vs. 0.43 ± 0.07).

More osteophytes were observed in the fracture than control group (Table 4-2, Fig. 4-4) The fractured group had visible osteophytes at the apical margin in 15 out of

16 proximal sesamoid bones, and 9 out of 16 at the basilar margin. Controls had only 5 bones out of 14 with apical osteophytes and 0 at basilar osteophytes.

Table 4-2. The number of osteophytes observed.

Group	Number of Bones with Apical Osteophytes (#)	Number of Bones with Basilar Osteophytes (#)
Fracture	15/16	9/16
Control	5/14	0/14

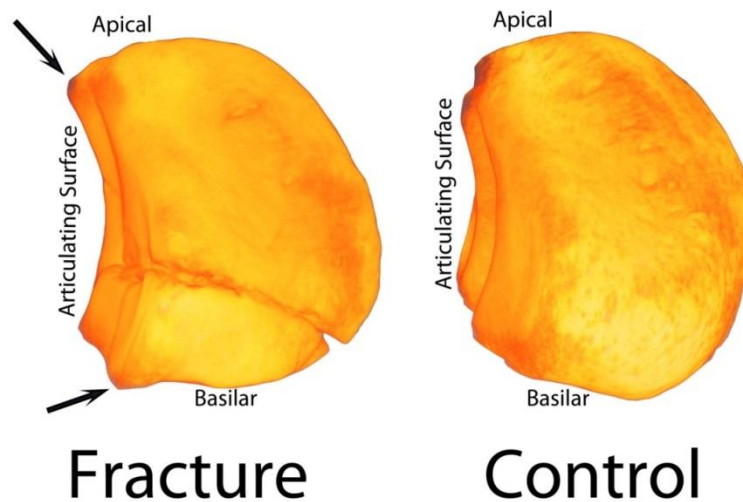


Figure 4-4: Osteophytes (black arrows) were seen at the apical and basilar regions of the articulating surface on the proximal sesamoid bones of the fracture group.

4.3.1 Exercise History

The work-to-rest ratio for the entire career (Fig 4-5A) and the 12 weeks prior to euthanasia (Fig 4-5B) was less in the fracture group than controls indicating that the fracture group received more rest and less work than the controls. The bone volume fraction of the sesamoid bones was correlated with the work-to-rest ratio (Fig 4-5C).

Work-to-rest ratio was approximately 1.0 in control animals, and less than 1.0 in three

of the four animals in the fracture group. Hence, the fracture group ran more distance in races than in training while controls ran similar distances in races and training (Fig 4-5D).

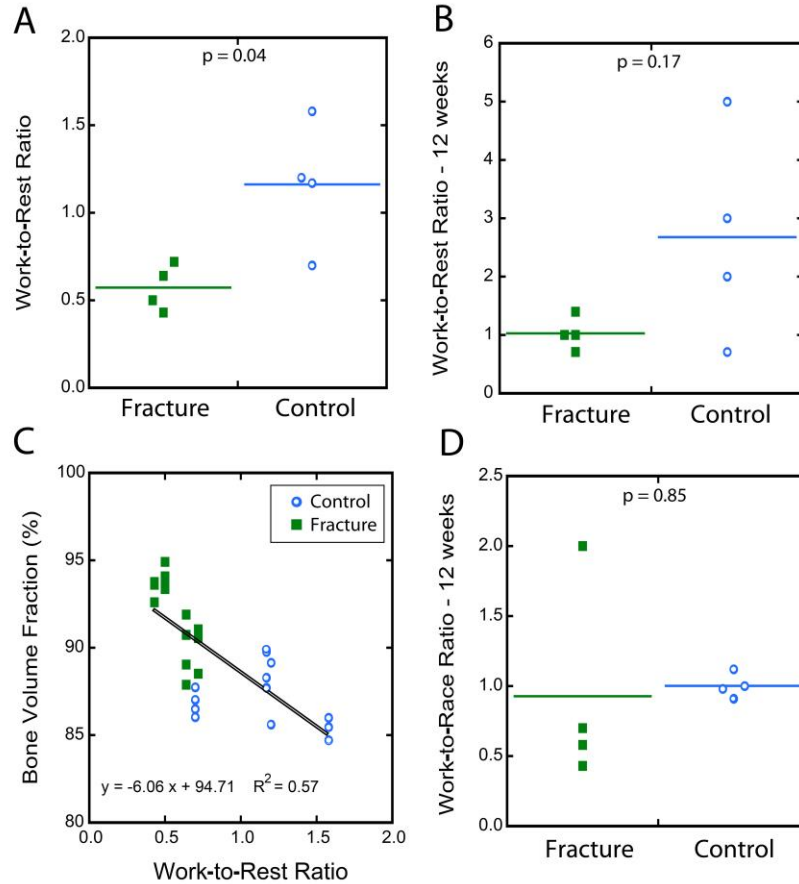


Figure 4-5: (A) The work-to-rest ratio over the entire racing career was significantly less in the fracture group than controls. A work-to-rest ratio of 0.5 indicates that for every one week of work, the animals had 2 weeks of rest. (B) In the 12 weeks prior to fracture/ethanasia, the fracture group work-to-rest ratio was approximately 1.0, meaning equal amounts of work and rest. Control animals however were working much more than resting. (C) Bone volume fraction is negatively correlated with the work-to-rest ratio over the entire career. (D) The work-to-race ratio in the 12 weeks prior to fracture/ethanasia shows that control animals had equal amounts of distance run in races and training, while the majority of fractured animals ran less distance in training than in races.

Horses in both groups had long periods without high speed exercise (measured as consecutive weeks of rest, Fig 4-6A). None of the animals exceeded 9 weeks of consecutive work (Fig 4-6A). In the fracture group, the number of consecutive weeks worked was less than the number of consecutive weeks of rest while in the control group, the number of consecutive weeks worked was greater (Fig 4-6B). The range of consecutive weeks worked in control animals (1-3 weeks) was similar to the range of consecutive weeks of rest in the animals that sustained a fracture (1-3 weeks). Similarly, the range of consecutive weeks of rest in the control animals (1-2 weeks) was similar to the range of consecutive weeks of work in the fracture group (1-2 weeks).

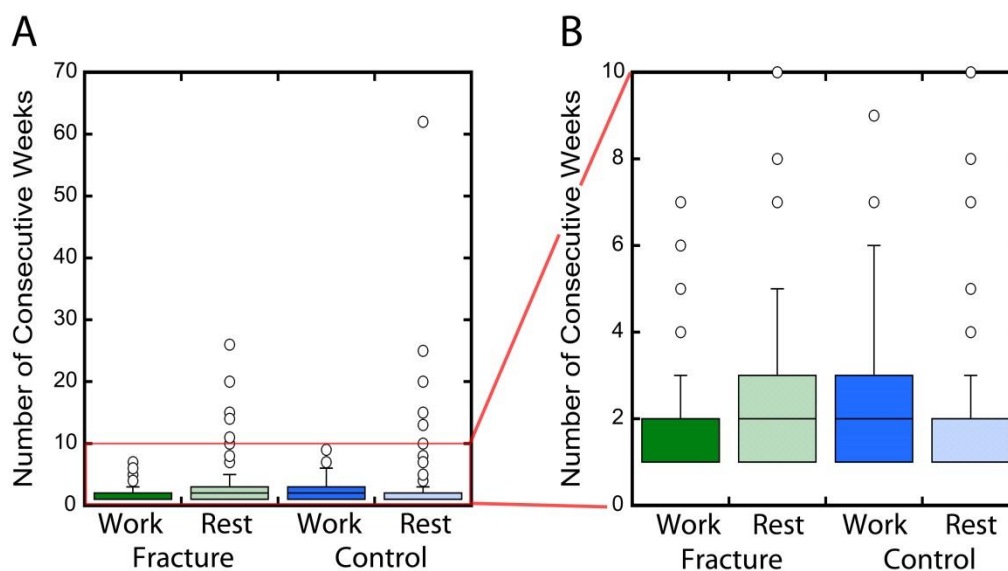


Figure 4-6: The number of consecutive weeks of work and of rest across the animal's career is shown. (A) Occasionally long periods of rest lasted longer than 10 weeks in both fractured and control animals, however consecutive weeks of work never exceeded nine weeks. (B) The fracture group would commonly work for 1-2 consecutive weeks and rest for 1-3 weeks, while control animals would work for 1-3 consecutive weeks and rest for 1-2 weeks.

No differences in total furlongs run, number of races, average workout distance or average workout time was found between groups. Total furlongs run and number of races was correlated with age of the animal at euthanasia; older animals had run in more races and further total distances over the course of their life (data not shown, see Appendix F).

4.4 Discussion

The goal of this study was to determine differences in proximal sesamoid bone morphology, bone volume fraction, tissue mineral density, and exercise history associated with catastrophic fracture of the proximal sesamoid bone. Bone volume fraction was greater in the sesamoid bones of horses that sustained a fracture as compared to controls. Horses with smaller work-to-rest ratios had increased bone volume fraction. We also found that horses that fractured the proximal sesamoid bone had more weeks of consecutive rest and fewer weeks of consecutive work than controls.

Our finding that bone volume fraction is greater in fractured bones is consistent with prior studies. Prior studies using post mortem analysis also reported increased bone volume fraction of fractured proximal sesamoid bones as compared to control racehorses (97, 147) as well as controls living in pasture (91). Increases in bone volume fraction of the third metacarpal and carpal bones have been associated with galloping exercise compared to jogging exercise (90). The current study is novel in using micro-computed tomography to provide three-dimensional analysis of bones. Our data indicated that the region of the proximal sesamoid bone that was most likely

to fracture (the basilar region) was also the region with the greatest increase in bone volume fraction, further highlighting the association between increased bone volume fraction and fracture pathology.

In this study, we also analyzed changes in tissue mineral density. Greater tissue mineral density leads to increased tissue strength (152) but also increased tissue brittleness (153). Whole bone tissue mineral density and regional bone tissue mineral density did not differ among groups. There were minor decreases in regional tissue mineral density in the apical subchondral and basilar subchondral regions of bones from the fracture group, however they were not significantly different. We attribute the minor difference in tissue mineral density in these sub-regions to the presence of osteophytes. The apical subchondral and basilar subchondral regions are the most common location for osteophytes to form as these regions are on the edge of the bone at the articulating surface (149). Osteophytes were visible at these two regions in fractured proximal sesamoid bones in the current study (Fig 4-4), while no osteophytes were visible at the basilar margin and only a few apical osteophytes were present in the control group (Table 4-2). Our finding differs from a prior report that suggested that fracture was less likely to occur in bones without osteophytes (149). A possible explanation for the contradictory findings is that the current study used micro-CT imaging (a more accurate technique) while prior work used two-dimensional radiographs. Radiographs are less sensitive to features such as osteophytes or vascular channels. In a study of 100 horses with lameness resulting from proximal sesamoid bone pain, radiographs showed poor specificity in identifying vascular channels from incomplete fractures (154).

Our study found that an exercise history including longer rest periods was associated with fracture. When interpreting our results, it is important to remember that only high speed exercise was recorded. High speed exercise causes the greatest loads on bones and joints as well as the greatest bone tissue strain and strain rate (155, 156). Mechanical adaptation of bone is most sensitive to the greatest tissue strain and strain rate experienced by the bone (63, 64, 77, 157-159). Therefore, exercise at high speeds is more influential on bone density than lower speed activities. No differences in the average distance or time per logged high speed exercise event were observed between animals with fractures and controls. Hence, the differences between groups appeared to be the weeks of consecutive exercise rather than differences in the intensity of each exercise event. Decreased total work-to-rest ratio and decreased number of consecutive weeks of work were found in fractured versus control animals, indicating that the fracture group may be in less strenuous training programs. An important limitation to this interpretation is that the exercise history data does not include full medical history; it is possible that more rest and less work was prescribed to treat or manage some underlying injury or condition that influenced fracture risk independent of bone volume fraction.

A possible explanation for increased bone density in fractured bones could be osteoarthritis in the joint. We observed evidence of arthritis in the proximal sesamoid bones. Osteoarthritis is associated with increased subchondral bone thickening (160), bone marrow lesions (161) and osteophytes. Subchondral thickening in proximal sesamoid bones and bone marrow lesions in the third metacarpal have both been associated with fracture of the proximal sesamoid (97). Osteoarthritis and bone

marrow lesions are associated with pain (162) that can cause subtle changes in gait that alter stresses on bones potentially contributing to fracture risk. It is interesting to note that greater osteoarthritic changes were observed in the contralateral limb as compared to the fractured limb of racehorses, and may indicate overloading of the limb that fractures (97). Although we did observe signs of osteoarthritis in fractured and contralateral limbs, osteophytes were also common in the control group and is a limitation to this explanation that arthritis increases fracture risk.

Increased bone density and bone volume fraction are typically associated with increased bone strength, raising the question of why increased bone volume fraction would be associated with fracture. Fractures in the proximal sesamoid bones of racehorses, however, occur by the creation of a linear smooth fracture plane transverse to the bone (95). Such a fracture plane is more consistent with rapid unstable crack growth than a single excessive load (a single excessive load would be expected to have an irregular and jagged fracture plane). Fracture toughness is the material property that describes brittle failure due to rapid unstable crack growth. We propose that the increase in bone density in the proximal sesamoid reduced fracture toughness of the tissue within the sesamoid to the point where rapid crack growth becomes more likely. The proximal sesamoid bones are often characterized as cancellous bone with a thin outer shell. In cancellous bone, void space helps to prevent rapid crack growth because as the crack reaches a void, the crack tip and the stress concentration in front of the crack tip are eliminated, and a new crack must initiate for crack growth to continue (163). The fracture toughness of a foam-like material is related to volume fraction. When the volume fraction ranges from 0-50% (which includes most

cancellous bone), fracture toughness is positively correlated with bone volume fraction (164). However, in porous ceramics, fracture toughness is positively correlated with volume fraction across a range from 70-90%, but at volume fractions exceeding 90% fracture toughness is reduced (165). The sesamoid bones range in bone volume fraction of the proximal sesamoid in this study was 85-95%, suggesting that the increase in volume fraction of the sesamoid bones from the fracture group may have reduced fracture toughness.

A strength of this study is the use of micro-computed tomography to characterize bone tissue. Micro-CT is a three-dimensional technique that can identify and segment bone from other soft tissues. Magnetic resonance imaging has also been used to show a densification of proximal sesamoid bones that sustain a fracture (97). However, contrast in magnetic resonance imaging is dependent upon water content. Bone has a much lower water content than the surrounding joint and soft tissue and, therefore, has relatively low contrast compared to neighboring soft tissues. While images of proximal sesamoid bones used in this study were not acquired in vivo, new technology has produced a high-resolution-CT system for use on the standing horse (voxel size 150 x 150 x 150 μ m). Standing high-resolution-CT does not require anesthesia and is faster than MRI making it advantageous to use in the field. In the near future, CT images will be acquired in live horses and could be used to track morphological changes over time, and inform patient-specific fracture risk based on bone morphology. The current study supports the use of micro-CT to detect changes in the proximal sesamoid internal architecture that are associated with fracture risk.

This study is not without limitations. The total number of horses per group is small; although the total number of sesamoids is more reasonable (n=30). While we showed that bone volume fraction was greater in animals that sustained a fracture, we do not know how often increased bone volume fraction leads to fracture. A larger clinical study monitoring bone volume fraction would be required to determine fracture risk from bone volume fraction.

Based on our analysis, we suggest greater amounts of rest are associated with greater bone volume fraction and increased risk of proximal sesamoid bone fracture. Additionally, changes in bone density and increased fracture risk may be influenced by osteoarthritic changes in the joint. We propose that when bone volume fraction exceeds 90%, fracture toughness is reduced. To our knowledge, this study is the first to associate morphological changes in the proximal sesamoid with exercise history. Adapting training routines could prevent proximal sesamoid bones from becoming sclerotic. New high-resolution computed tomography systems specifically designed for use on a standing horse make it possible to monitor bone density in vivo.

REFERENCES

63. Churches AEH, C. R. . Functional Adaptation of Bone in Response to Sinusoidally Varying Controlled Compressive Loading of the Ovine Metacarpus. *Clinical Orthopaedics & Related Research*. 1982;168:265-80.
64. Rubin CT, Lanyon LE. Regulation of bone mass by mechanical strain magnitude. *Calcif Tissue Int*. 1985;37(4):411-7.
77. Hsieh Y, Turner CH. Effects of loading frequency on mechanically induced bone formation. *Journal of Bone and Mineral Research*. 2001;16(5):918-24.
90. Firth EC, Delahunt J, Wichtel JW, Birch HL, Goodship AE. Galloping exercise induces regional changes in bone density within the third and radial carpal bones of Thoroughbred horses. *Equine Veterinary Journal*. 1999;31(2):111-5.
91. Young DR, Nunamaker DM, Markel MD. Quantitative evaluation of the remodeling response of the proximal sesamoid bones to training-related stimuli in Thoroughbreds. *Am J Vet Res*. 1991;52:1350.
95. Anthenill LA, Gardner IA, Pool RR. Comparison of macrostructural and microstructural bone features in Thoroughbred racehorses with and without midbody fracture of the proximal sesamoid bone. *Am J Vet Res*. 2010;71:755.
97. Peloso JG, Vogler Iii JB, Cohen ND, Marquis P, Hilt L. Association of catastrophic biaxial fracture of the proximal sesamoid bones with bony changes of the metacarpophalangeal joint identified by standing magnetic resonance imaging in cadaveric forelimbs of Thoroughbred racehorses. *Journal of the American Veterinary Medical Association*. 2015;246(6):661-73.
102. Johnson BJ, Stover SM, Daft BM, Kinde H, Read DH, Barr BC, et al. Causes of death in racehorses over a 2 year period. *Equine Veterinary Journal*. 1994;26(4):327-30.
103. Stover SM, Murray A. The California Postmortem Program: Leading the Way. *Veterinary Clinics of North America: Equine Practice*. 2008;24(1):21-36.
104. Sarrafian TL, Case JT, Kinde H, Daft BM, Read DH, Moore JD, et al. Fatal musculoskeletal injuries of Quarter Horse racehorses: 314 cases (1990–2007). *Journal of the American Veterinary Medical Association*. 2012;241(7):935-42.

105. Verheyen K, Price J, Lanyon L, Wood J. Exercise distance and speed affect the risk of fracture in racehorses. *Bone*. 2006;39(6):1322-30.
106. Cohen ND, Berry SM, Peloso JG, Mundy GD, Howard IC. Association of high-speed exercise with racing injury in thoroughbreds. *J Am Vet Med Assoc*. 2000;216(8):1273-8.
107. Anthenill LA, Stover SM, Gardner IA. Risk factors for proximal sesamoid bone fractures associated with exercise history and horseshoe characteristics in Thoroughbred racehorses. *Am J Vet Res*. 2007;68:760.
147. Anthenill LA, Gardner IA, Pool RR, Garcia TC, Stover SM. Comparison of Macrostructural and Microstructural Bone Features in Thoroughbred Racehorses with and without Midbody Fracture of the Proximal Sesamoid Bone. *American Journal of Veterinary Research*. 2010;71(7):755-65.
148. Shi L, Wang D, Riggs CM, Qin L, Griffith JF. Statistical analysis of bone mineral density using voxel-based morphometry—an application on proximal sesamoid bones in racehorses. *Journal of Orthopaedic Research*. 2011;29(8):1230-6.
149. Anthenill LA, Stover SM, Gardner IA, Hill AE, Lee CM, Anderson ML, et al. Association between findings on palmarodorsal radiographic images and detection of a fracture in the proximal sesamoid bones of forelimbs obtained from cadavers of racing Thoroughbreds. *American Journal of Veterinary Research*. 2006;67(5):858-68.
150. Wang D, Shi L, Griffith JF, Qin L, Yew DTW, Riggs CM. Comprehensive surface-based morphometry reveals the association of fracture risk and bone geometry. *Journal of Orthopaedic Research*. 2012;30(8):1277-84.
151. Boskey AL. Bone composition: relationship to bone fragility and antiosteoporotic drug effects. *BoneKEy Rep*. 2013;2.
152. Hernandez CJ, Beaupre GS, Keller TS, Carter DR. The influence of bone volume fraction and ash fraction on bone strength and modulus. *Bone*. 2001;29(1):74-8.
153. Currey JD. Tensile yield in compact bone is determined by strain, post-yield behaviour by mineral content. *Journal of Biomechanics*. 2004;37(4):549-56.
154. O'Brien TR, Morgan JP, Wheat JD. Sesamoiditis in the Thoroughbred: a radiographic study. *J Am Vet Radiol Soc*. 1971;12:75.

155. Rubin CT, Seeherman H, Qin Y-X, Gross TS. The mechanical consequences of load bearing in the equine third metacarpal across speed and gait: the nonuniform distributions of normal strain, shear strain, and strain energy density. *The FASEB Journal*. 2013;27(5):1887-94.
156. Rubin CT, Lanyon LE. Limb mechanics as a function of speed and gait: a study of functional strains in the radius and tibia of horse and dog. *Journal of Experimental Biology*. 1982;101:187-211.
157. Goodship AE, Lanyon LE, McFie H. Functional adaptation of bone to increased stress. An experimental study. *The Journal of Bone & Joint Surgery*. 1979;61(4):539-46.
158. Warden SJ, Turner CH. Mechanotransduction in the cortical bone is most efficient at loading frequencies of 5–10 Hz. *Bone*. 2004;34(2):261-70.
159. O'Connor JA, Lanyon LE, MacFie H. The influence of strain rate on adaptive bone remodelling. *Journal of Biomechanics*. 1982;15(10):767-81.
160. Li G, Yin J, Gao J, Cheng TS, Pavlos NJ, Zhang C, et al. Subchondral bone in osteoarthritis: insight into risk factors and microstructural changes. *Arthritis Research & Therapy*. 2013;15(6):223-.
161. Hunter DJ, Gerstenfeld L, Bishop G, Davis AD, Mason ZD, Einhorn TA, et al. Bone marrow lesions from osteoarthritis knees are characterized by sclerotic bone that is less well mineralized. *Arthritis Research & Therapy*. 2009;11(1):R11-R.
162. Sowers MF, Hayes C, Jamadar D, Capul D, Lachance L, Jannausch M, et al. Magnetic resonance-detected subchondral bone marrow and cartilage defect characteristics associated with pain and X-ray-defined knee osteoarthritis. *Osteoarthritis and Cartilage*. 2003;11(6):387-93.
163. Cook RB, Zioupos P. The fracture toughness of cancellous bone. *Journal of Biomechanics*. 2009;42(13):2054-60.
164. Gibson LJ, Ashby MF. *Cellular solids: structures & properties*. Second Edition ed. Oxford: Pergamon Press; 1997.
165. Rice RW. Grain size and porosity dependence of ceramic fracture energy and toughness at 22 °C. *Journal of Materials Science*. 1996;31(8):1969-83.

CHAPTER 5

CONCLUSIONS AND FUTURE DIRECTIONS

5.1 Summary

Mechanical loading is a powerful anabolic stimulus that regulates bone formation, bone geometry, and bone density. The goal of this dissertation was to understand how applied loading altered bone geometry at the microscopic scale. In this dissertation, I have demonstrated for the first time the spatial association of bone formation and the local tissue stress and strain in cancellous bone after short-term loading. Additionally, I have assessed the influence of osteocyte density on locations of bone formation. Lastly, in a model of intense exercise, I found the bone volume fraction of a bone submitted to large loads during exercise was correlated with the amount of exercise an animal performed over the course of their life as indicated by the work-to-rest ratio. Interestingly, lower work-to-rest ratios correlated with greater bone volume fraction, which was also associated with increased fracture risk.

5.1.1 Aim 1 - Local Tissue Strain Regulates Bone Formation

Bone adapts to mechanical stimuli. While in vivo mechanical loading can lead to increased density of the whole bone, theory suggests that the relationship between tissue stress/strain and subsequent bone formation occurs in cancellous bone at the scale of individual trabeculae. Here we examine bone formation one week following mechanical stimulus. Three bouts of cyclic loading (300 cycles/day on 3 consecutive

days) were applied to caudal vertebrae of female rats (n=7). Bone formation was determined using three-dimensional images of fluorescent markers of bone formation (0.7x0.7x5.0 μ m) and local tissue stress/strain was determined using high-resolution finite element models. Three days of mechanical stimuli resulted in an increase in bone formation in the following week. Mineralizing surface and volume of bone formed was greater in loaded bones as compared to unloaded controls. The number of bone formation sites was greater in loaded animals than controls. The additional bone formation sites occurred at locations of greatest local tissue strain energy density (SED). In addition, the probability of observing bone formation was greater at locations of the microstructure experiencing greatest SED, but did not exceed 32%. Our findings demonstrate that bone formation in the week following a short-term mechanical stimulus occurs near regions of bone tissue experiencing high tissue SED. However, the ability of tissue stress/strain to predict the locations of bone formation remains modest. Further improvements may require accounting for additional factors such as osteocyte distribution or fluid flow.

5.1.2 Aim 2 – Osteocytes' Role in Mechanotransduction

Osteocytes play an integral role in bone by sensing mechanical stimuli and releasing signaling factors that direct bone formation. One consequence of the role of osteocytes in mechanotransduction is that the size of osteocyte populations influences bone functional adaptation i.e. regions of bone tissue with greater osteocyte populations are expected to be more responsive to mechanical stimuli. To determine the effects of the osteocyte population on bone functional adaptation we applied

mechanical loads to the 8th caudal vertebra of skeletally mature female rats (6 months of age, n=8 loaded, n=8 sham controls). The distribution of tissue stress and strain within cancellous bone was determined using high resolution finite element models, the osteocyte distribution was determined using nano-computed tomography, and locations of bone formation were determined using three-dimensional images of fluorescent bone formation markers. Loading increased bone formation with increase in 3D mineralizing surface, formation volume, and number of bone formation sites. Bone formation occurred at regions of cancellous bone experiencing greater tissue stress and strain, but stress and strain was only a modest predictor of bone formation; even at locations of greatest stress the probability of observing bone formation did not exceed 41%. The local osteocyte population was not correlated with locations of new bone formation. Osteocyte lacunar density was reduced near trabecular surfaces as compared to regions near the center of trabeculae. This investigation supports the idea that local tissue stress and strain influence the locations of bone formation in cancellous bone, but suggests that the size of the osteocyte population itself does not influence locations of bone formation. We conclude that other aspects of osteocytes such as osteocyte connectivity, lacunocanicular nano-geometry and/or fluid pressure/shear distributions within the marrow space may be more influential in regulating bone mechanotransduction than the number of osteocytes.

5.1.3 Aim 3 – Exercise Induced Morphological Changes in Racehorses

Fracture of the proximal sesamoid bones is the most common musculoskeletal injury that leads to death in racehorses. Increases in bone density in the proximal

sesamoid bones have been associated with fracture. Determining why bone volume increase could lead to the development of preventive approaches to limit bone volume and decrease fracture risk. In this study, we examined the proximal sesamoid bones of Thoroughbred racehorses that suffered fracture in a proximal sesamoid bone in the forelimb, and compared the bones to those from sex and age matched controls (n=4 animals per group). Both sesamoid bones were collected from the fractured and contralateral limb of the fracture group (total of 16 bones) and medial and lateral sesamoid bones from both forelimbs were collected from controls (total of 14 bones). Micro-computed tomography images of all proximal sesamoid bones (voxel size 50 x 50 x 50 μ m) were used to determine bone volume fraction and tissue mineral density. The relationship between proximal sesamoid morphology and exercise history in terms of high speed training and racing was determined. Bone volume fraction was greater in the proximal sesamoid bones of the fracture group (91.24 \pm 2.56%, mean \pm SD) than controls (87.04 \pm 1.74%, mean \pm SD). The exercise history in horses that sustained a fracture had longer periods of rest interrupted by shorter periods of high speed exercise compared to controls. The ratio of the total number of weeks with high speed exercise to the number of weeks of rest (work-to-rest ratio) was decreased in animals that had greater bone volume fraction. To our knowledge this is the first time morphological changes have been correlated to exercise history. Our study suggests exercise routines with excessively long rest periods may contribute to changes in sesamoid bones that are associated with fracture.

5.1.4 Synthesis

Increased mechanical loading causes bone formation at locations of greatest tissue stress/strain, represented in this work as strain energy density. However, the ability of tissue stress/strain to predict locations of bone formation remains low (32% in aim 1 and 41% in aim 2). In aim 1, 3-month-old rats were used as younger animals are more responsive to mechanical loading. The number of bone formation sites in loaded animals doubled in loaded animals compared to unloaded controls. Nearly half of the bone formation sites in loaded specimens were near locations of high strain energy density. Therefore, I conclude that half of the bone formation was due to background growth or remodeling (sites not near bone formation) and half were in response to the mechanical environment. However, there was no way to determine if a specific location of bone formation was associated with background remodeling or mechanically induced bone formation.

Therefore, in aim 2 methods were adapted to differentiate between background and mechanically induced bone formation. In aim 2, I used older animals, 6 months of age. This older animal is skeletally mature and therefore we expected to see less bone formation due to growth. By adding an additional bone formation marker administered prior to loading, I was also able to identify background bone formation from mechanically induced bone formation. I attribute the increased probability of observing bone formation seen in aim 2 as compared to aim 1 to the ability to isolate sites of mechanically induced bone formation. Even after incorporating osteocyte density and isolating only mechanically induced bone formation, the maximum predictive ability on locations of bone formation remained below 50%. I therefore conclude that factors other than tissue stress and strain direct the locations of bone

formation and suggest that mechanical stimulation of bone marrow, osteocyte connectivity, or lacunar shape influence the mechanical stimulation of osteocytes.

High intensity exercise applies large loads to bone and influences bone formation. The bone volume fraction of the proximal sesamoid bones in racehorses was correlated with the work-to-rest ratio of an animal's exercise history. Animals with a smaller work-to-rest ratio (less than 1.0 indicating fewer weeks of work than weeks of rest) showed higher bone density in sesamoid bones. Fracture in proximal sesamoid bones was associated with higher bone volume fraction, and is hypothesized to occur because of reduced fracture toughness. Understanding the influence of the exercise schedule on bone density would allow for training routines to be altered to regulate bone formation and bone volume fraction to reduce fracture risk in racehorses.

5.1.5 Strengths and Limitations

Aim 1 and 2 in this dissertation are novel for evaluating bone formation in three-dimensions using fluorescent bone formation markers (the gold standard). Serial milling made it possible to identify small volumes of bone formation in three-dimension which is critical for evaluating the spatial association between locations of bone formation and the tissue mechanical stimuli. In my work, the distribution of stress and strain were calculated from linear homogeneous finite element models. However, bone is not a homogenous material, and therefore, modeling bone as homogenous is a limitation to this work. High resolution micro computed tomography made it possible to identify the locations of osteocyte lacunae. However, I was only

able to identify osteocyte lacunae and it is possible that not all lacunae housed a viable osteocyte. However, given the young age of our animals it is unlikely that osteocyte lacunae would be empty. Therefore, it was a safe assumption that local lacunar density represented local osteocyte density. Local lacunar density was incorporated into spatial correlation methods for the first time, to further explore the role of osteocytes in mechanotransduction.

High resolution micro computed tomography also strengthened the morphological measures made in the proximal sesamoid bones of racehorses. Previous measures of the proximal sesamoid bones of horses used two-dimensional techniques such as histology and radiographs which cannot capture the same level of detail as three-dimensional imaging. Racehorses also provide a unique model for exercise, as all high-speed running is recorded. Therefore, the ability to associate bone morphology to exercise history over many years is novel. However, medical records were not available, and it's possible that rest was prescribed to manage other musculoskeletal injury or symptoms of arthritis. If other musculoskeletal injuries or arthritis were present, those conditions could predispose the animal to increased fracture risk. A limitation in this work is the lack of access to information about other medical conditions in the animal, and no knowledge of when rest was required verses planned.

5.2 Future Directions

The findings presented in this dissertation identify many new hypotheses and directions for future studies. Regarding the locations of mechanically induced bone

formation, future investigations into the role of marrow pressurization and fluid flow would determine the contribution of mechanical stimuli from marrow on locations of bone formation. It is also possible that the lacunar-canalicular network influenced the stimulation of osteocytes. Investigating osteocyte connectivity and lacunar-canalicular geometry would enhance our understanding of mechanotransduction. Determining the most influential pathway directing locations of bone formation could lead to therapeutic interventions to direct bone formation to locations that increase mechanical strength in bone.

Bone volume fraction in proximal sesamoid bones was influenced by exercise loading histories. Increased bone volume fraction was associated with fracture. While I hypothesized that fracture occurs due to a reduced fracture toughness associated with high bone volume fraction, proving the hypothesis would require experimental testing. Bone volume fraction could also be influenced by the magnitude of the tissue strain experienced in an animal. Due to variations in bone geometry and joint confirmation it is likely that the tissue strains experienced is not the same in all racehorses. Further investigations into the mechanical environment of the proximal sesamoid bone would enhance our understanding of mechanical adaptation. Here I discuss advancements in the current line of investigation as well as new research areas.

5.2.1 Continued Research Areas

5.2.1.1 The Effect of Marrow Pressure on Bone Functional Adaptation

The results in this dissertation have shown that stresses and strains in bone tissue had a limited ability to predict locations of bone formation. One possible

explanation for this finding is that there are other stimuli that can cause bone formation. A candidate for future investigation is fluid shear and pressure in the bone marrow. Determining the most influential stimuli for enhancing bone formation would lead to the development of therapies to influence bone adaptation.

When external loads are applied to bone, bone marrow is pressurized. Marrow pressurization has been shown to inhibit bone loss independently of bone tissue strain (112-114). Marrow pressurization could stimulate marrow resident cells and induce bone formation. In fact, in vitro studies have shown that many marrow resident cells respond to fluid shear (143-145, 166), and computational models predict that fluid shears that occur in bone marrow are comparable to the fluid shears applied in vitro (111). Additionally, an analysis of bone formation in the rodent tail loading model determined that stress and strains in bone marrow were more strongly correlated to bone formation than stress and strain in mineralized tissue (115). However, finite element models of bone marrow used in these correlations with bone formation were extremely simplified treating marrow as a solid and not a fluid (115). More accurate finite modeling methods of bone marrow are available (111) and could provide better representation of the bone marrow fluid shear strains. Therefore, I suggest modeling marrow fluid shear strains and using the spatial correlation techniques developed in this dissertation to determine the influence of marrow on locations of bone formation. Understanding the influence of marrow strains versus tissue strain on locations of bone formation would identify marrow resident cells or osteocytes as the key cell line to target to enhance functional adaptation in cancellous bone.

5.2.1.2 The Effect of the Lacunar Canalicular Network on Functional Adaptation

In Chapter 3, we concluded that osteocyte lacunar density did not influence the locations of mechanically induced bone formation. However, osteocytes serve a mechanosensory role in bone and are crucial for mechanotransduction (35). Bone tissue strains cause interstitial flow through the lacunar canalicular network, however, the relationship between bone tissue strain and fluid shear may be nonlinear. Gradients in marrow pressure can also cause interstitial fluid flow (98). As osteocytes are more sensitive to fluid shear than substrate deformation (37) It is possible that fluid shear in the lacunar-canalicular space is a better indicator of bone functional adaptation. Recent high resolution finite element modeling of bone tissue, extracellular matrix, and osteocytes have shown that lacunar and canalicular shape and geometry affect the fluid shears acting on the osteocyte's cell body and processes (121, 140, 141). Images of rat tail vertebrae in this dissertation were not collected at a high enough resolution to detect canaliculi, or accurately describe lacunar shape. There are however many imaging modalities that can be used in bone at a high enough resolution to identify the lacunar-canalicular network and its geometry (for a review of imaging techniques see (167)). In chapter 3, several image techniques were used to identify locations of bone formation, locations of osteocyte lacunae, and to determine the stress/strain distribution throughout bone. I suggest in future work additional images are collected at a higher resolution than performed in this dissertation to identify the lacunar-canalicular network and its geometry. Imaging of the lacunar-canalicular network, would isolate the effect of connectivity and lacunar-canalicular geometry on fluid flow stimulating osteocytes. Connectivity and lacunar-canalicular geometry can be altered

with age or disease. Understanding the importance of connectivity and lacunar-canalicular geometry on regulating bone formation would identify important pathways to enhance mechanotransduction in bone.

5.2.1.3 Fracture Toughness in Proximal Sesamoid Bones

Proximal sesamoid bones in racehorses that experience a fracture are denser than those of sex and age matched controls. Increased bone density is normally related to increased bone strength. The pathology that causes fracture in bones with increased density is not understood. It is possible that changes in material properties could explain why the dense bones experience fracture. For example, increased mineral content makes bone more brittle and therefore more susceptible to fracture.

Interestingly, changes in material properties of proximal sesamoid bones have not been investigated. In chapter 4, I examined changes in material properties by evaluating the tissue mineral density in proximal sesamoid bones that fractured, and in controls. However, no changes in tissue mineral density were found. The fracture plane tends to be smooth (95), suggesting that unstable crack growth is a likely failure process. Fracture of proximal sesamoid bones also occurs very quickly, normally within a stride or two during high speed running. Hence, both the fracture plane and loading mechanism are consistent with the idea of unstable crack growth and reduced fracture toughness. Therefore I propose that fracture is caused by a reduction in fracture toughness due to the increased bone volume fraction. Fracture toughness testing of cancellous bone has suggested that voids in bone act as a toughening mechanism slowing crack growth and controlling it to a stable rate (163). When the

crack tip reaches a void, the crack tip is eliminated and as the load is redistributed; a new crack would have to initiate before the fracture could propagate further. In a material with no void space, the crack tip is always present, and the stress concentration that forms in front of the crack tip encourages crack growth which can become unstable. The fracture toughness of porous ceramics has found that at low porosities(10-15%), fracture toughness can increase compared to solid ceramics with 0% porosity (165). The best way to test our hypothesis is to perform mechanical testing. I suggest using the sesamoid bones from the contralateral limb of animals that sustained a fracture, and sesamoid bones from controls to evaluate fracture toughness as it relates to bone density.

5.2.2 New Research Areas

5.2.2.1 Finite Element Modeling of Proximal Sesamoid Bones

While loading applied to proximal sesamoid bones has been generalized as bending, the distribution of stress and strain throughout the bone is unknown. Proximal sesamoid bones are generally considered to be in tension from the forces applied by the ligaments combined with bending caused by contact with the third metacarpal. This loading would generally lead to tensile stress/strain in the flexor region and local compressive stress/strain perpendicular to the third metacarpal in the subchondral bone. However, proximal sesamoid bones are also very short, and therefore transverse shear caused by bending should not be ignored. The medial proximal bone is commonly smaller than the lateral proximal bone (150) and fracture is observed more often in the medial proximal sesamoid bone (96). Therefore, size

and geometry could contribute to the stresses experienced and influence fracture risk. Given the complicated shape of proximal sesamoid bones, analytical approximation of the stress and strain distribution is limited and computational techniques are required. Finite element modeling is a powerful tool that can be used to determine the stress and strain distribution within proximal sesamoid bones. In chapter 4, locations of fracture were associated with the locations of greatest regional bone volume fraction. Regional bone volume fraction would influence the tissue stress and strain. Regions with high density should reduce the tissue strain, which would support the proposal that fracture does not occur due to tissue yield or reduced strength. However, if a defect or crack was present on the flexor surface in the region, fracture could occur from crack propagation, and reduced fracture toughness due to higher bone density. Therefore, correlating the tissue stress and strain with locations of fracture would enhance our understanding of fracture pathology. Osteophytes were observed in the proximal sesamoid bones. Osteophytes forming at the site of ligament insertion change the bone geometry which could influence the distribution of stress and strain within the bone. Understanding how osteophytes affect the stress and strain would allow us to determine if osteophytes increase or decrease the risk of fracture. The loading placed on a proximal sesamoid bone is variable throughout a single stride. As the joint flexes the ligaments apply greater forces and bending moment increases. Fracture of the proximal sesamoid bones commonly occurs at the end of a race when animals' muscles are fatigued and therefore hyperflexion of the joint occurs. Increased stress and strain during hyperflexion could explain why fracture occurs at this time. However, it is unclear how much stress and strain would increase due to hyperflexion.

Ultimately finite element modeling could be used to understand the mechanical environment of proximal sesamoid bones and enhance understanding of fracture pathology.

5.2.2.2 The Effect of Exercise Schedule on Bone Formation

It is known that a long period of rest increases the anabolic effect of mechanical loading (79). The results of chapter 4 showed greater bone volume fraction of the proximal sesamoid bones was associated with more weeks of consecutive rest and fewer consecutive weeks of exercise. Animals with greater bone volume fraction also had lower work-to-rest ratios, indicating that over their racing career, they had fewer high speed workouts and therefore fewer loading cycles than control animals. Since greater bone volume fraction was associated with proximal sesamoid fracture, it is important to understand how exercise schedules influence the amount of bone formation. Animal models studying the effect of applied loading to bone formation show that over weeks of loading bone becomes accustomed to the applied loading and the amount of bone formation returns to normal levels (79, 168). In vivo loading for 5 weeks followed by 5 weeks of rest is sufficient to increase bones' response to loading when loading resumes (79). However, racehorses were commonly resting only 2-3 weeks. Additionally, racehorses are only performing high speed running for 1-3 consecutive weeks, which is shorter than the 5 weeks that has been investigated (79). I propose that in vivo loading studies be performed to determine how many weeks of rest are required to increase the bone formation response. Determining the effect of shorter periods of loading and rest would enhance our understanding of functional

adaptation that occurs in racehorses. Finding a loading schedule that decreases the bone formation response would inform how training schedules should be modified to prevent bone volume fraction from reaching densities associated with fracture risk.

REFERENCES

35. Bonewald LF. The amazing osteocyte. *Journal of Bone and Mineral Research*. 2011;26(2):229-38.
37. You J, Yellowley CE, Donahue HJ, Zhang Y, Chen Q, Jacobs CR. Substrate deformation levels associated with routine physical activity are less stimulatory to bone cells relative to load-induced oscillatory fluid flow. *Journal of Biomechanical Engineering*. 2000;122:387-93.
79. Saxon LK, Robling AG, Alam I, Turner CH. Mechanosensitivity of the rat skeleton decreases after a long period of loading, but is improved with time off. *Bone*. 2005;36(3):454-64.
95. Anthenill LA, Gardner IA, Pool RR. Comparison of macrostructural and microstructural bone features in Thoroughbred racehorses with and without midbody fracture of the proximal sesamoid bone. *Am J Vet Res*. 2010;71:755.
96. Anthenill LA, Stover SM, Gardner IA. Association between findings on palmarodorsal radiographic images and detection of a fracture in the proximal sesamoid bones of forelimbs obtained from cadavers of racing Thoroughbreds. *Am J Vet Res*. 2006;67:858.
98. Jacobs CR, Temiyasathit S, Castillo AB. Osteocyte mechanobiology and pericellular mechanics. *Annual Review of Biomedical Engineering*. 2010;12:369-400.
111. Metzger TA, Kreipke TC, Vaughan TJ, McNamara LM, Niebur GL. The In Situ Mechanics of Trabecular Bone Marrow: The Potential for Mechanobiological Response. *Journal of Biomechanical Engineering*. 2015;137(1):011006-.
112. Qin Y-X, Kaplan T, Saldanha A, Rubin C. Fluid pressure gradients, arising from oscillations in intramedullary pressure, is correlated with the formation of bone and inhibition of intracortical porosity. *Journal of Biomechanics*. 2003;36(10):1427-37.
113. Kwon RY, Meays DR, Tang WJ, Frangos JA. Microfluidic enhancement of intramedullary pressure increases interstitial fluid flow and inhibits bone loss in hindlimb suspended mice. *Journal of Bone and Mineral Research* 2010;25(8):1798-807.

114. Hu M, Cheng J, Qin Y-X. Dynamic hydraulic flow stimulation on mitigation of trabecular bone loss in a rat functional disuse model. *Bone*. 2012;51(4):819-25.
115. Webster D, Schulte FA, Lambers FM, Kuhn G, Müller R. Strain energy density gradients in bone marrow predict osteoblast and osteoclast activity: A finite element study. *Journal of Biomechanics*. 2015;48(5):866-74.
121. Niebur GL, Yuen JC, Hsia AC, Keaveny TM. Convergence behavior of high-resolution finite element models of trabecular bone. *Journal of Biomechanical Engineering*. 1999;121(6):629-35.
140. Verbruggen SW, Vaughan TJ, McNamara LM. Fluid flow in the osteocyte mechanical environment: a fluid–structure interaction approach. *Biomechanics and Modeling in Mechanobiology*. 2014;13(1):85-97.
141. Verbruggen SW, Vaughan TJ, McNamara LM. Mechanisms of osteocyte stimulation in osteoporosis. *J Mech Behav Biomed Mater*. 2016;62:158-68.
143. McAllister TN, Du T, Frangos JA. Fluid Shear Stress Stimulates Prostaglandin and Nitric Oxide Release in Bone Marrow-Derived Preosteoclast-like Cells. *Biochemical and Biophysical Research Communications*. 2000;270(2):643-8.
144. Castillo AB, Jacobs CR. Mesenchymal Stem Cell Mechanobiology. *Current Osteoporosis Reports*. 2010;8(2):98-104.
145. Soves CP, Miller JD, Begun DL, Taichman RS, Hankenson KD, Goldstein SA. Megakaryocytes are mechanically responsive and influence osteoblast proliferation and differentiation. *Bone*. 2014;66:111-20.
150. Wang D, Shi L, Griffith JF, Qin L, Yew DTW, Riggs CM. Comprehensive surface-based morphometry reveals the association of fracture risk and bone geometry. *Journal of Orthopaedic Research*. 2012;30(8):1277-84.
163. Cook RB, Zioupos P. The fracture toughness of cancellous bone. *Journal of Biomechanics*. 2009;42(13):2054-60.
165. Rice RW. Grain size and porosity dependence of ceramic fracture energy and toughness at 22 °C. *Journal of Materials Science*. 1996;31(8):1969-83.
166. Li YJ, Batra NN, You L, Meier SC, Coe IA, Yellowley CE, et al. Oscillatory fluid flow affects human marrow stromal cell proliferation and differentiation. *Journal of Orthopaedic Research*. 2004;22(6):1283-9.

167. Cardoso L, Fritton SP, Gailani G, Benalla M, Cowin SC. Advances in assessment of bone porosity, permeability and interstitial fluid flow. *Journal of Biomechanics*. 2013;46(2):253-65.
168. Lambers FM, Koch K, Kuhn G, Ruffoni D, Weigt C, Schulte FA, et al. Trabecular bone adapts to long-term cyclic loading by increasing stiffness and normalization of dynamic morphometric rates. *Bone*. 2013;55(2):325-34.

APPENDIX A: PRELIMINARY LOADING STUDIES PRIOR TO CHAPTER 2

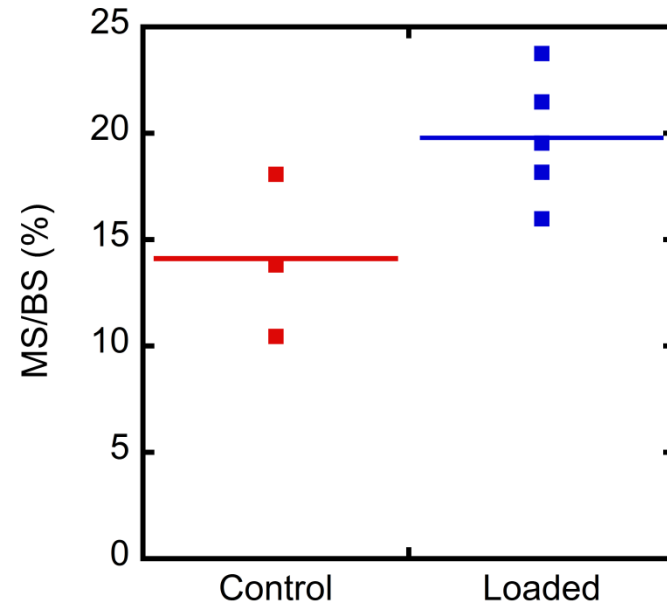
Rat Tail Loading Study #	Rat ID #	Group	Time Between Pin Insertion and Loading (Days)	Days of Loading / Sham	Result	MS/BS (%)	Notes
1	1	Loaded	0	1	successful completion of study		
1	2	Pinned Not Loaded	0	1	successful completion of study	13.81	
1	3	Loaded	0	1	successful completion of study		
1	4	Pinned Not Loaded	0	1	successful completion of study	18.08	
1	5	Unpinned control	NA	0	successful completion of study		
1	6	Unpinned control	NA	0	successful completion of study		
2	7	Loaded	0	3	Euthanized before study completion	NA	Pin-Bone interface failure
2	8	Loaded	0	3	Euthanized before study completion	NA	Pin-Bone interface failure
2	9	Loaded	0	3	successful completion of study		
2	10	Pinned Not Loaded	0	3	successful completion of study	10.45	
2	11	Loaded	0	3	Euthanized before study completion	NA	Pin-Bone interface failure
2	12	Loaded	0	3	Euthanized before study completion	NA	Pin-Bone interface failure
2	13	Loaded	0	3	Euthanized before study completion	NA	Tail infected
3	14	Loaded	21	3	successful completion of study	21.48	
3	15	Loaded	21	3	successful completion of study	19.54	
3	16	Loaded	21	3	successful completion of study	23.75	
3	17	Loaded	21	3	successful completion of study	15.98	
3	18	Loaded	21	3	successful completion of study	18.17	

Rat ID #	Group	MS/BS
2	Unloaded	13.81
4	Unloaded	18.08
0	Unloaded	10.45

14.12 Mean
3.12 STD

Rat ID #	Group	MS/BS
14	Loaded 3 days, 21 days after surgery	21.48
15	Loaded 3 days, 21 days after surgery	19.54
16	Loaded 3 days, 21 days after surgery	23.75
17	Loaded 3 days, 21 days after surgery	15.98
18	Loaded 3 days, 21 days after surgery	18.17

19.78 Mean
2.68 STD

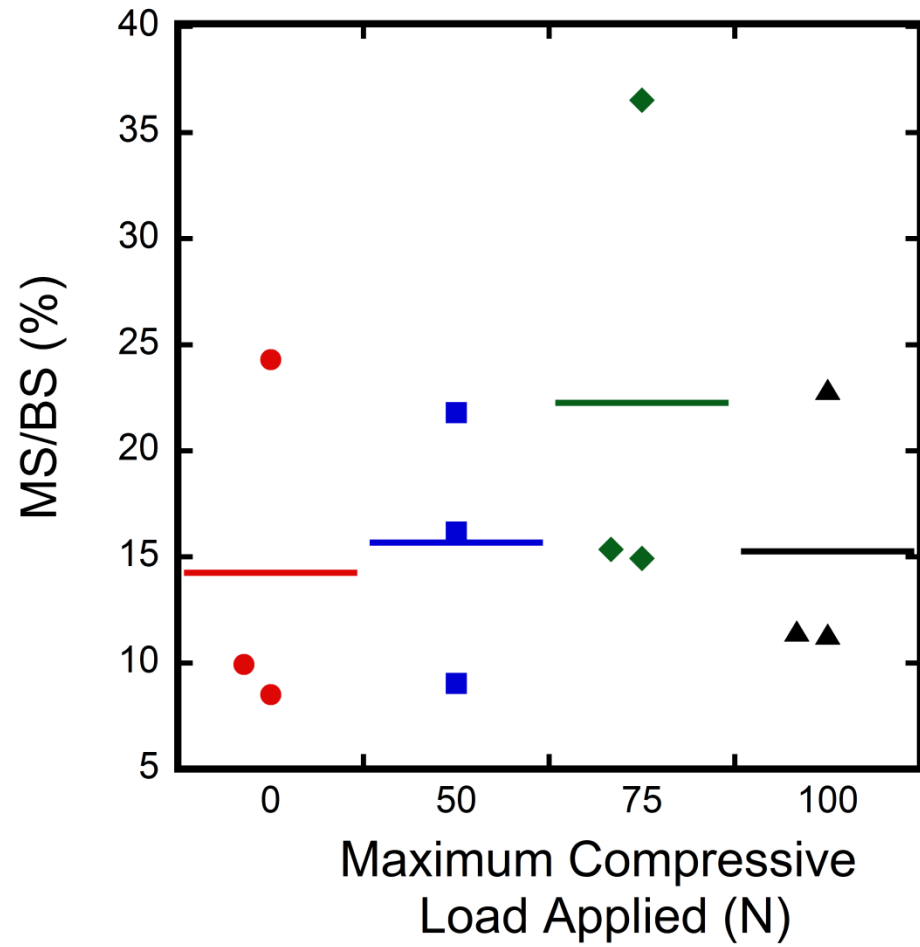


APPENDIX B: PRELIMINARY LOADING STUDIES PRIOR TO CHAPTER 3

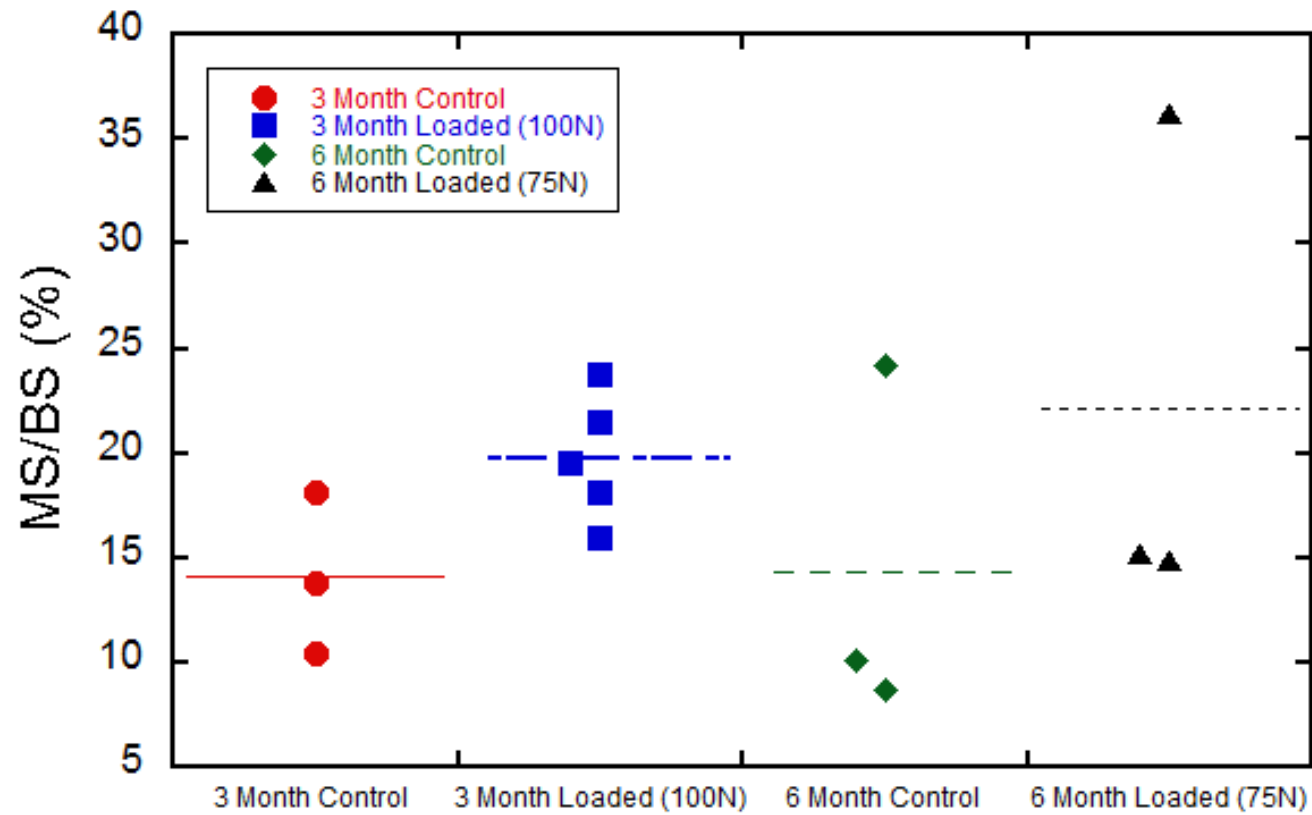
Rat Tail Loading Study #	Rat ID #	Group	Animal Age at Loading (months)	Time Between Pin Insertion and Loading (Days)	Days of Loading/ Sham	Maximum Compressive Load (N)	Result	MS/BS (%)	Notes
5	35	Loaded	6	21	3	75	successful completion of study	15.35	
5	36	Loaded	6	21	3	50	successful completion of study	9.04	
5	37	Pinned Not Loaded	6	21	3	0	successful completion of study	9.94	
5	38	Pinned Not Loaded	6	21	3	0	successful completion of study	8.52	
5	39	Loaded	6	21	3	75	successful completion of study	14.93	
5	40	Loaded	6	21	3	100	successful completion of study	22.89	
5	41	Loaded	6	21	3	50	successful completion of study	21.80	
5	42	Loaded	6	21	3	50	successful completion of study	16.17	
5	43	Loaded	6	21	3	75	successful completion of study	36.53	

5	44	Pinned Not Loaded	6	21	3	0	successful completion of study	24.30	
5	45	Loaded	6	21	3	100	successful completion of study	11.51	
5	46	Loaded	6	21	3	100	successful completion of study	11.36	
5	47	Loaded	3	21	3	75	successful completion of study	NA	woven bone on periosteum
5	48	Loaded	3	21	3	75	successful completion of study	NA	woven bone on periosteum
5	49	Loaded	3	21	3	50	successful completion of study	NA	woven bone on periosteum
5	50	Loaded	3	21	3	50	successful completion of study	NA	woven bone on periosteum
5	51	Loaded	3	21	3	75	successful completion of study	NA	woven bone on periosteum
5	52	Loaded	3	21	3	50	successful completion of study	NA	woven bone on periosteum

6th Month Rats Loading Titration Study



2D Histology Measures of Bone Formation in Young vs Old



APPENDIX C: STANDARD OPERATING PROCEDURES

Rat Surgery Material Preparation
Cornell University
Biomedical Mechanics and Materials Laboratory
Standard Operating Procedure
Rat Surgery Material Preparation
Version #2
Edited by: Erin Litts
Author: Matt Goff
Date: 07/16/2012

Summary: This protocol describes the method for preparing rat surgery materials.

Key Words: Rat surgery material preparation

Materials: Sterilization pouch (Henry Schein 1124853), k-wires (threaded rod 2mm Zimmer), drill bits 3/64" (McMaster-Carr 29315A115), drill sleeves (custom made)

Equipment: Autoclave, k-wire cutters, permanent marker, ruler

I. INTRODUCTION

The following procedure describes the method for preparing rat surgery materials.

II. METHODS

1. Preparation K-wires for surgeries
 - 1.1. Cut k-wire to the length of 45 mm using the k-wire cutter
 - 1.2. If neither end is sharpened, sharpen one end to a point using the sanding belt in the Rhodes Machine shop (you must receive training to use the machine shop) (figure 1)
 - 1.3. Mark 45 mm long k-wire at 4 mm, 34 mm and 40 mm from the sharpened end (figure 1)
 - 1.3.1. (Note: 40 mm mark is for power drill while 4 mm and 34 mm marks are for final cuts after surgery)
2. Put 2 prepared k-wires, 2 drill bits, and 2 drill sleeves into each sterilization pouch and seal.
 - 2.1. Autoclave the pouches less than one week prior to surgery in one of the available autoclaves in the Weill Animal Facility.

2.2. Store in a clean area.



Figure 1: Sharpened and marked k-wire

Surgery Technique
Cornell University
Biomedical Mechanics and Materials Laboratory
Standard Operating Procedure
Live surgery on Rat Tails - Installing K-wires through C7 and C9
Vertebra
Version 5
01/13/2015
Edited by: Erin Cresswell
Author: Matthew Goff
Principle Investigator: Dr. Christopher J. Hernandez

Summary: This protocol describes the steps involved with inserting k-wires through the caudal 7 (Cd7) and caudal 9 (Cd9) vertebrae.

Key Words: K-wire installation, rat tail, surgery on live rats

Materials: Sterilized Surgery Materials (see SOP Rat Surgery Material Preparation, k wire, drill bit, sleeves), meloxicam or approved pain medication, Gauge 22 needles, 3ml syringes, Novisan, 70% ethanol, sterile gloves (sizes 7, 7.5 and 8), Non-sterile gloves (sizes small, medium and larger), surgical masks, sterile cloth/drapes, sterile gauze, surgical coats (large and extra-large), surgical cap, liquid band aid (new-skin liquid bandage), peroxide, q-tips, drilling fixture (custom made), external fixators (custom made), sterile permanent marker, isofluorane, rat eye ointment

Equipment: power drill, dremel, extension cord (8-15 ft), anesthesia machine, digital dental x-ray/fluoroscope

I. INTRODUCTION

The following procedure describes the steps involved with inserting k-wires through the caudal 7 (Cd7) and caudal 9 (Cd9) vertebrae.

II. METHODS

1. Surgery for the installation of k-wires
 - 1.1. Transport the rats from receiving location to fluoroscope or digital dental x-ray room in a rat transporting unit
 - 1.2. Subdivide the surgical area so that there are specific places for rats in the four stages
 - 1.2.1. Rats awaiting surgery
 - 1.2.2. Rats being prepared for surgery
 - 1.2.3. Rats undergoing surgery/loading
 - 1.2.4. Rats recovering from surgery
 - 1.3. Put on surgical attire
 - 1.3.1. Disposable cap
 - 1.3.2. Mask
 - 1.3.3. Lab coat
 - 1.3.4. Non-sterile gloves

Note for rest of surgery

Person I: The person doing the main surgery

Person II: Sterile person assisting with surgery, monitor anesthesia depth, assist Person I in handling the rat

Person I:

- 1.4. Clean and sanitize the table, drilling fixtures, marker, external fixators and table with 70% ethanol (contact time required is 15 minutes).

Person II:

- 1.5. Weigh the animal and record the measurement in grams.
- 1.6. Put the rat in the anesthesia chamber
- 1.7. Turn on anesthesia chamber
- 1.8. Leave rat in chamber until obvious signs of anesthesia
- 1.9. Take the rat out of the box and place it on the table on top of the heating table or a heating pad covered with a cloth
- 1.10. Place the isofluorane gas mask over the rat's nose and mouth
- 1.11. Place a small amount of rat eye ointment at the corner of each eye.
Move the top lid in a blinking motion to spread the ointment over the surface of the eye.
(Note: Follow SOPs for specific isofluorane machine and take to the veterinarian)

- 1.12. Can give the shot of pain killer now (see step 3.1 for dosing) to give time to set in before they wake.

Person I:

- 1.13. Pinch the toe or tail or ear to check anesthesia depth. Make sure you don't see any reactions from the rat.
- 1.14. With the rat on its side, palpate for the posterior elements on Cd5 vertebra (C5 would be the last bone with large wings on its proximal end).
- 1.15. Palpate and count vertebrae distal to Cd5 until Cd7 is located.
- 1.16. Put marks on the Cd7/Cd8 and Cd8/Cd9 vertebral disks using permanent marker
- 1.17. Clean the tail with alternative scrubs with Novisan and 70% ethanol 3 times each. On the last scrub with ethanol, make sure you can get out most of the Novisan.
- 1.18. Put a sterile cloth under the tail.
- 1.19. Place the tail in the bottom piece of the drilling fixture based on the position of the marks. Try to place the tail so that the C8 is centered about the drilling holes.
- 1.20. Position the rat on its side so that the dorsal side is towards the chamfered edge of the drilling fixture.
- 1.21. Place the top half of the drilling fixture in alignment with bottom half via pins and secure it by tightening the thumb screws. Person II should hold the tail in place while the top is being secured.
- 1.22. Position rat and drilling fixture on side and check the positioning using the fluoroscope or digital dental x-ray. If tail not properly position in fixture, remove the top of the fixture and adjust the tail accordingly and repeat steps 1.17-1.20
- 1.23. Once positioned along the length of the tail centered on the Cd7 and Cd9 adjust the dorsal ventral slide until centered.
- 1.24. Confirm positioning with fluoroscope or digital dental x-ray.

Person II:

- 1.25. Open one sterilized pouch with non sterile gloves. Make sure you do not touch any sterilized item with non-sterile gloves. Open in a way to prevent contamination of the items and surgical pack.
- 1.26. Put on sterile gloves.
- 1.27. Drop the sleeves into the holes on the drilling fixture
- 1.28. Person I should hold onto the dremel while person II picks a drill bit and place the drill bit holder without touching it. At same time person I should tighten the drill bit holder without touching the drill bit.

Person I:

- 1.29. Place drill bit in sleeve and drill holes using the stainless steel bushings as guides. Drill Cd7 first. Use speed setting 10.
 - 1.29.1. Note: Make sure you are drilling sideways not from top to bottom
 - 1.30. Change the drill bit and drill Cd9
 - 1.31. Person I should hold a power drill and Person II should insert k-wires into the power drill. Insert k-wire up to the 3rd mark.
 - 1.32. Screw the k-wires into Cd7 and Cd9 holes
 - 1.32.1. Note: If tendons begin to wrap around the k wire (the distal end of the tail will begin to curl/move), back out a little and proceed with drilling.
 - 1.32.2.
 - 1.33. Open the drilling fixture and careful remove tail by slowly pulling the k-wires from the drilling fixture (they might be slightly stuck in sleeves)
 - 1.34. Cut k-wires at 1st and 2nd markings
 - 1.35. Place k-wires in external fixators
 - 1.36. Use fixators as a guide and center the k-wires by slowly rotating but not pushing the k-wires
 - 1.37. Clean wound site with peroxide and q-tip.
 - 1.38. A liquid bandage around the pin sites.
 - 1.39. Place rat in a new clean cage in the recovery area with the heating pad under a corner of the cage.
2. Surgery on additional rats
 - 2.1. Clean and sanitize the table, drilling fixtures, marker and place new cloth over heating pad.
 - 2.2. Repeat steps 1.5-1.37
 3. Post operative care
 - 3.1. Give Diluted Meloxicam (concentration 0.5 mg/ml) subcutaneously (SC) (1-1.2 ml/Rat) on the day of surgery (dose 2mg/kg)
 - 3.2. Give Diluted Meloxicam (concentration 0.5 mg/ml) subcutaneously (SC) (0.5 – 0.6 ml/Rat) for the next 2 days with 24 hours gap between the doses.
 - 3.2.1. Note: Make sure you do not apply any force on the tail while injecting the rats.
 - 3.3. Apply peroxide around the pins with Q-tip, then apply liquid band aid around pin-insertion sites weekly after the surgery until loading begins.

Rat Tail Loading Technique
Cornell University
Biomedical Mechanics and Materials Laboratory
Standard Operating Procedure
Live loading to the Cd8 Vertebra through K-wires in the Cd7& Cd9
Vertebra
Version 1
02/03/2015
Author: Erin Cresswell
Principle Investigator: Dr. Christopher J. Hernandez

Summary: This protocol describes the steps involved with securing the animal in the loading device and running the Wintest loading software.

Key Words: Wintest Loading Protocol, rat tail, loading on live rats

Materials: Meloxicam , Gauge 22 needles, 3ml syringes, 70% ethanol , Non-sterile gloves, lab coats, liquid band aid (new-skin liquid bandage), peroxide, q-tips, loading fixture (custom made), screw drivers that fix loading fixture screws, external fixators (custom made) with set screws matching allen wrench, isofluorane, rat eye ointment, k wire cutters, small towels, hand warmers, heating pad

Equipment: Bose Loading device, Computer with Wintest, extension cord (8-15 ft), anesthesia machine with chamber and nose cone

I. INTRODUCTION

The following procedure describes the steps involved with loading the caudal 8 (Cd8) vertebrae.

II. METHODS

4. Prep the animal and room
 - 4.1. Transport the rats from housing location to the surgical suite with the bosc loading device set up on the cart in a rat transporting unit
 - 4.2. Subdivide the surgical area so that there are specific places for rats in the 3 stages
 - 4.2.1. Rats awaiting loading
 - 4.2.2. Rats undergoing loading
 - 4.2.3. Rats recovering from loading
 - 4.3. Put on surgical attire
 - 4.3.1. Lab coat
 - 4.3.2. Non-sterile gloves

- 4.4. Clean and sanitize the loading table, loading fixtures with 70% ethanol (contact time required is 15 minutes).
- 4.5. Place towels and heating pads on the loading table where the animal's body will lay.
- 4.6. Weigh the animal and record the measurement in grams.
- 4.7. Put the rat in the anesthesia chamber
- 4.8. Turn on anesthesia chamber
- 4.9. Leave rat in chamber until obvious signs of anesthesia
- 4.10. Take the rat out of the box and place it on the table on top of the loading table where the heating pad covered with a cloth are positioned.
- 4.11. Place the isofluorane gas mask over the rat's nose and mouth
- 4.12. Place a small amount of rat eye ointment at the corner of each eye. Move the top lid in a blinking motion to spread the ointment over the surface of the eye.
(Note: Follow SOPs for specific isofluorane machine and take to the veterinarian)
- 4.13. Can give the shot of pain killer now (see step 3.1 for dosing) to give time to set in before they wake.
- 4.14. Pinch the toe or tail or ear to check anesthesia depth. Make sure you don't see any reactions from the rat.
- 4.15. Remove the external fixator at this time and soak in 70% ETOH for cleaning.
- 4.16. With the rat on its belly weave the tail under the actuator and place the k wires into the two channels adjusting the distance between the wires as necessary for no stretching or compression of the tail between the k wires.
- 4.17. Place the bottom pieces of the loading fixture under each k wire. Place the small cube in its channel on the top piece with beveled edges perpendicular to the tail, align the top of the fixture with the bottom.
- 4.18. Start tightening the piece over the Cd9.
- 4.19. Start tightening the fixture by adjusting the screw over the k wire making sure the wings do not touch the top of the plastic in this process. Once the screw on the k wire is tight, pull the plastic body of the fixture away from the Cd8, now tighten the wings. Then tighten the screws on the outside, jumping back and forth from the two pins frequently to make it even.
- 4.20. Now go to the fixator piece over the Cd7 and repeat step 1.19
- 4.21. Now tighten the center screws of both pieces, finger tight, do not over tighten.

5. Operating Wintest

- 5.1. Turn on the computer and the two power supplies of the Bose machine.
- 5.2. Administrator has no password.
- 5.3. Open Wintest, and open one of the Rat_Tail>Loading_##N.prj files (where the number in the file name indicates the maximum load applied) that is appropriate for the load that will be applied to this animal.
- 5.4. Click on waveform and double check that the loading protocol is accurate (ramp, load magnitudes, frequency, number of cycles, etc.)
- 5.5. Click setup, channels, and then set load 2 and displacement to tare.
- 5.6. At this point you are about to start loading, double check the animal is under with a tail pinch.
- 5.7. Set the local to high, wait to see it turn on, then close.
- 5.8. Click on the floppy drive icon and wait for it to turn yellow, this starts the recording of the data channels displayed in the probes window.
- 5.9. Hit run, that then zero start to begin loading.
- 5.10. Monitor the displacement throughout loading and if it becomes increasing large and threatens to exceed the limit of the Bose machine (6mm) consider stopping early with stop level. (this is not ideal and will result in removal of the animal from the study, emergency stop is also an option in extreme cases.) Ideally the displacement remains small, and upon completion of the loading protocol click stop level to end the protocol.
- 5.11. Now click the floppy again and follow the prompts to save the collected load and displacement curves. Name with the date and animal number.
- 5.12. Now un strap the animal from the loading fixture by working in the reverse order, start by loosening the inside screw, then the outsides, then the wings, lastly the screws with the wings.
- 5.13. Gently remove the k wires from the channels and move the animal away from the loading device.
- 5.14. Only once the animal has been freed of the loading device, hit local off.

6. Post operative care

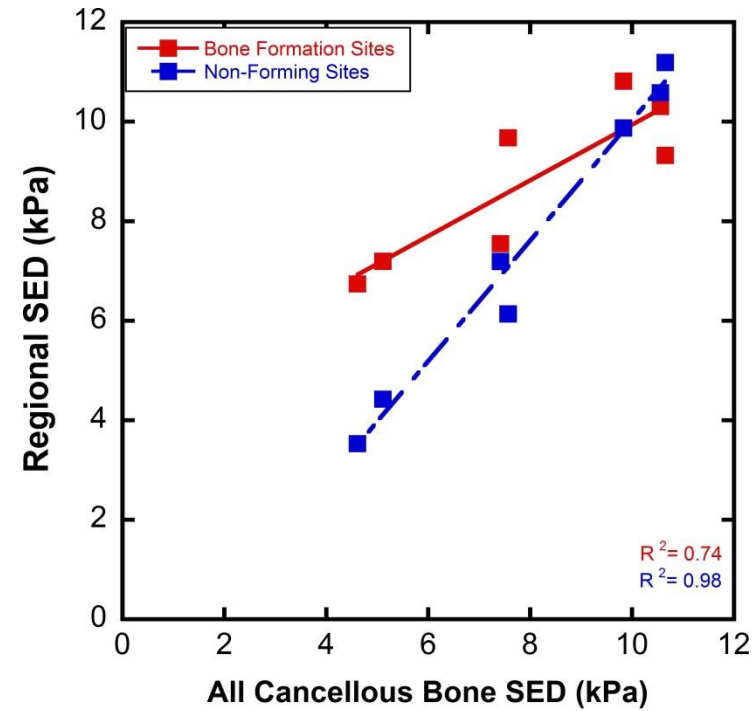
- 6.1. Give Diluted Meloxicam (concentration 0.5 mg/ml) subcutaneously (SC) (0.5ml for 250g BW – 0.6 ml for 300g BW) for each day of loading and 24 hours after the last loading session.
 - 6.1.1. Note: Make sure you do not apply any force on the tail while injecting the rats.
- 6.2. Apply peroxide around the pins with Q-tip, then apply liquid band aid around pin-insertion sites.

- 6.3. Put the external fixator back on, and write the animal number on the external fixator.
 - 6.4. Remove the animal from isoflourane and put in a clean cage with the heating pad under half of it. Monitor for the next half hour for signs of pain.
7. Repeat for as many animals as needed in a day
 - 7.1. Remember to clean the loading table and loading fixtures between animals.

APPENDIX D: CHAPTER 2 ADDITIONAL DATA

'Specimen'	Group	Measured Data					Calculated Data			
		Mineralizing Surface' (# of voxels)	Bone Surface' (# of voxels)	Bone Volume' (# of voxels)	Tissue Volume' (# of voxels)	Bone Formation Volume' (# of voxels)	MS/BS' (%)	BV/TV' (%)	BS/BV' (%)	FV/BV' (%)
'21'	Control	67957	996026	9191954	52811964	97083	6.82	17.41	10.84	1.06
'23'	Control	113175	1445948	15978945	55190914	179460	7.83	28.95	9.05	1.12
'25'	Control	130789	1024186	10472596	42177262	223810	12.77	24.83	9.78	2.14
'27'	Control	91907	1477716	18344652	52127931	372931	6.22	35.19	8.06	2.03
'29'	Control	128033	1501682	15388649	59985768	194873	8.53	25.65	9.76	1.27
'31'	Control	79415	1504981	17457496	60882009	149634	5.28	28.67	8.62	0.86
'33'	Control	195504	1494605	19980320	60512567	318456	13.08	33.02	7.48	1.59
'20'	Loaded	328613	1896369	23639549	69202686	1396242	17.33	34.16	8.02	5.91
'22'	Loaded	288855	1922269	19773160	64602609	1071121	15.03	30.61	9.72	5.42
'24'	Loaded	389559	2102440	26461068	76948829	1925029	18.53	34.39	7.95	7.27
'26'	Loaded	366765	1685780	18488887	63941293	2084602	21.76	28.92	9.12	11.27
'28'	Loaded	339966	1881554	27524429	64677678	1977777	18.07	42.56	6.84	7.19
'30'	Loaded	261662	1523321	17463774	68101507	1162626	17.18	25.64	8.72	6.66
'34'	Loaded	293068	1846481	17479235	62755973	1032046	15.87	27.85	10.56	5.90

Table: The amount of bone formation, measured as mineralizing surface and formation volume, and bone volume fraction and bone surface per bone volume is shown.



The SED at regions of bone formation and in regions of bone that did not experience new bone formation is shown relative to the SED throughout the cancellous bone region (geometric mean of the SED is shown).

Group	Specimen ID #	Cancellous Region	Connectivity	SMI	DA	Trabecular Thickness mean (um)	Trabecular Thickness Std (um)
Loaded	30	Proximal	200.50	2.231	0.660	107.05	33.98
Loaded	30	Distal	213.00	2.124	0.710	105.63	30.30
Loaded	34	Proximal	217.50	1.899	0.507	110.48	29.63
Loaded	34	Distal	224.50	1.888	0.667	108.95	32.33
Loaded	28	Proximal	246.00	2.079	0.527	107.48	31.90
Loaded	28	Distal	202.50	2.282	0.641	108.78	33.30
Loaded	26	Proximal	173.00	2.476	0.457	100.53	32.83
Loaded	26	Distal	197.50	2.494	0.671	100.73	31.00
Loaded	24	Proximal	164.50	2.559	0.558	103.38	31.48
Loaded	24	Distal	131.50	2.418	0.619	101.85	25.95
Loaded	22	Proximal	149.50	1.972	0.658	108.18	30.33
Loaded	22	Distal	150.00	2.019	0.584	104.88	25.25
Loaded	20	Proximal	245.00	2.375	0.446	105.45	35.75
Loaded	20	Distal	303.00	2.232	0.535	102.35	31.98
Control	21	Proximal	211.50	2.240	0.336	110.20	41.65
Control	21	Distal	176.50	2.063	0.477	113.38	41.63
Control	23	Proximal	96.00	2.026	0.563	118.23	37.05
Control	23	Distal	187.00	1.944	0.620	112.63	31.68
Control	25	Proximal	108.00	2.041	0.550	116.13	33.50
Control	25	Distal	60.50	2.264	0.649	105.85	28.03
Control	27	Proximal	85.50	1.931	0.458	121.23	38.78
Control	27	Distal	183.00	1.902	0.618	114.78	36.28
Control	29	Proximal	288.50	1.999	0.381	100.58	34.85
Control	29	Distal	242.00	2.009	0.329	109.10	39.43
Control	31	Proximal	310.00	1.795	0.375	103.40	34.38

Control	31	Distal	185.00	2.341	0.522	97.95	32.98
Control	33	Proximal	120.50	1.908	0.605	122.28	37.45
Control	33	Distal	145.50	1.983	0.630	115.58	32.35

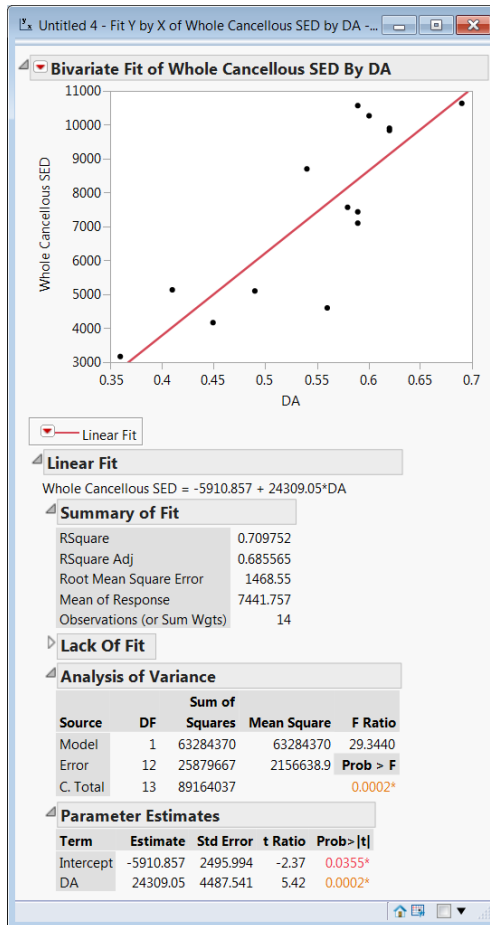
Table: Morphological measures of connectivity, structural modulus index, degree of anisotropy, and trabecular thickness were determined for both cancellous bone regions of interest in all specimens.

Group	Specimen ID #	Geometric Mean of Cancellous SED	Connectivity	SMI	DA	Trabecular Thickness mean (um)
Loaded	20	5111.02	548.00	2.30	0.49	103.90
Loaded	22	9827.52	299.50	2.00	0.62	106.53
Loaded	24	7416.84	296.00	2.49	0.59	102.61
Loaded	26	4611.40	370.50	2.49	0.56	100.63
Loaded	28	7566.71	448.50	2.18	0.58	108.13
Loaded	30	10649.87	413.50	2.18	0.69	106.34
Loaded	34	10557.27	442.00	1.89	0.59	109.71
Control	21	5130.94	388.00	2.15	0.41	111.79
Control	23	7091.87	283.00	1.99	0.59	115.43
Control	25	10278.21	168.50	2.15	0.60	110.99
Control	27	8695.56	268.50	1.92	0.54	118.00
Control	29	3178.59	530.50	2.00	0.36	104.84
Control	31	4168.41	495.00	2.07	0.45	100.68
Control	33	9900.84	266.00	1.95	0.62	118.93

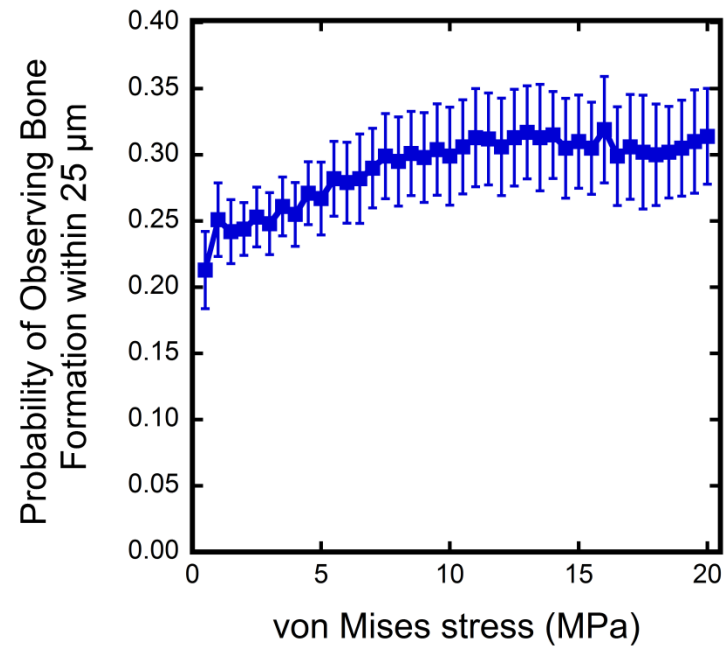
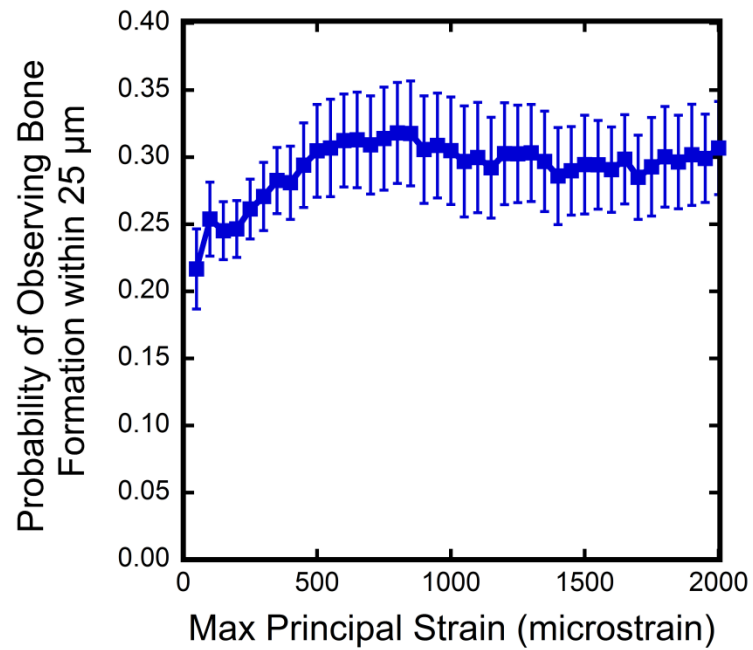
Correlate Bone Morphology with the Geometric Mean of the Cancellous Bone SED

R ² value	0.347	0.113	0.710	0.243
p-value	0.0267	0.2397	0.0002	0.0732

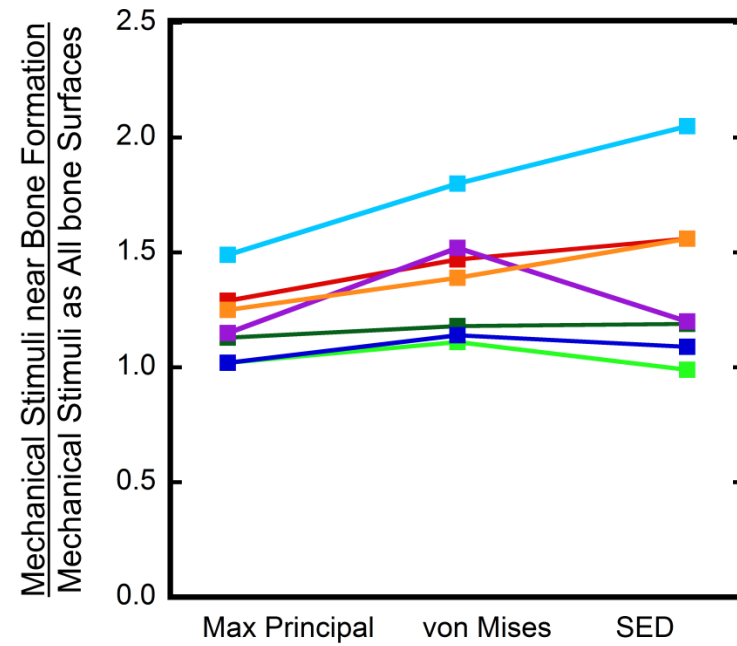
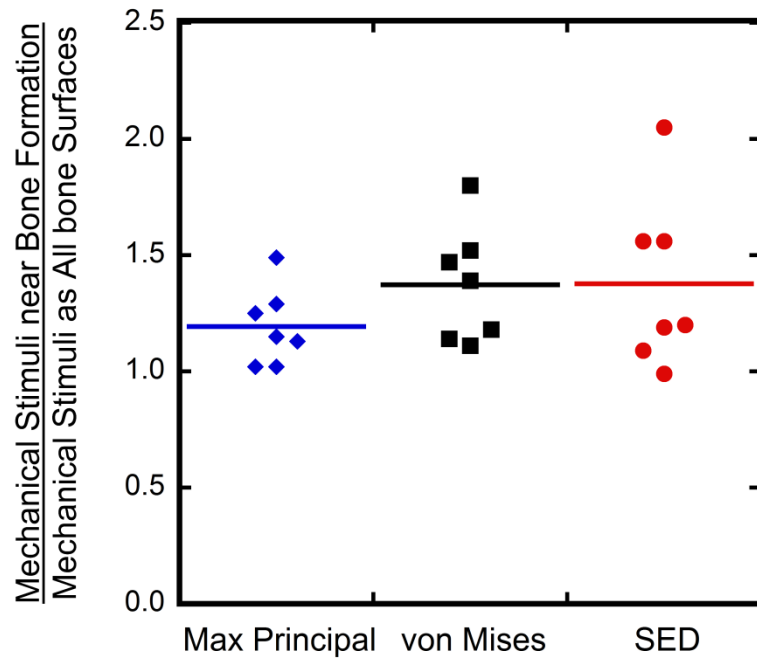
Table: Morphological data was averaged from the proximal and distal cancellous regions and correlated to the SED of cancellous bone per specimen. The most significant influence of SED in the cancellous region was the degree of anisotropy.



Degree of anisotropy was highly correlated with the SED experienced in the cancellous bone.



The probability of observing bone formation was also determined with maximum principal strain and von Mises stress as the mechanical stimuli. For the loaded specimen shown here, the curve is similar to SED as was reported in Chapter 2.



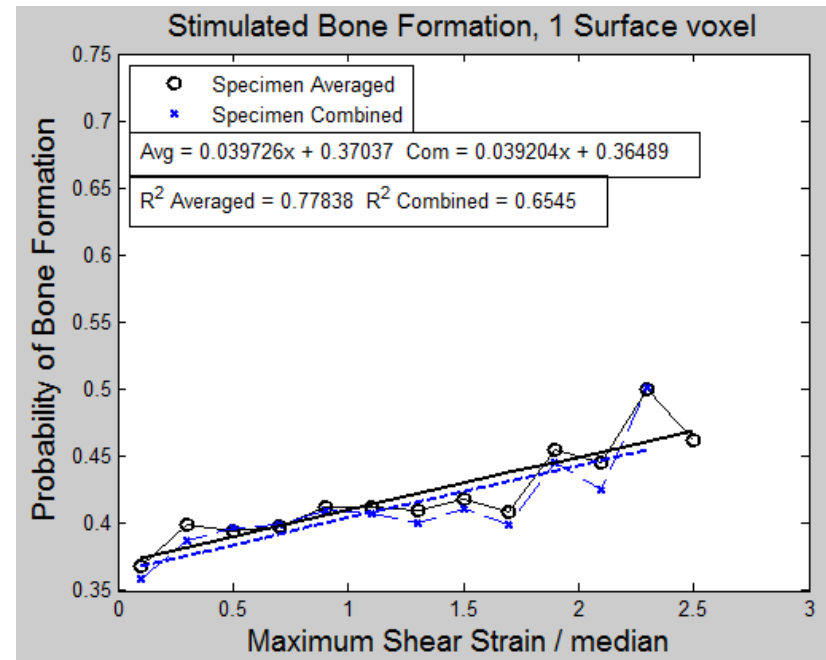
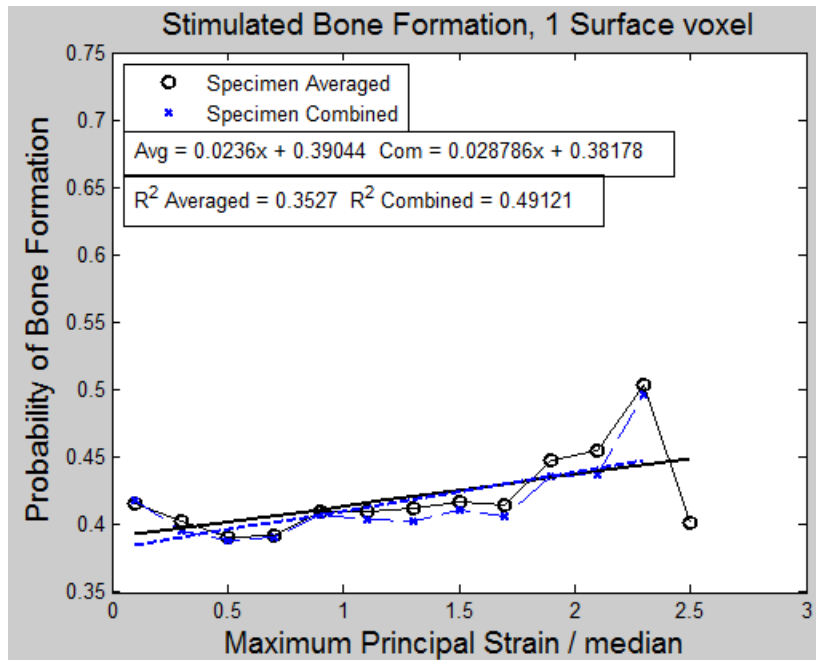
(Left) Maximum principal strain, von Mises stress, and SED all showed ratios of bone formation to all bone surfaces higher than 1.0 indicating that based on all 3 measures of stress/strain bone formation had occurred at locations of higher mechanical stimuli. (Right) Data is the same as seen on the left but lines connect the data for each specimen.

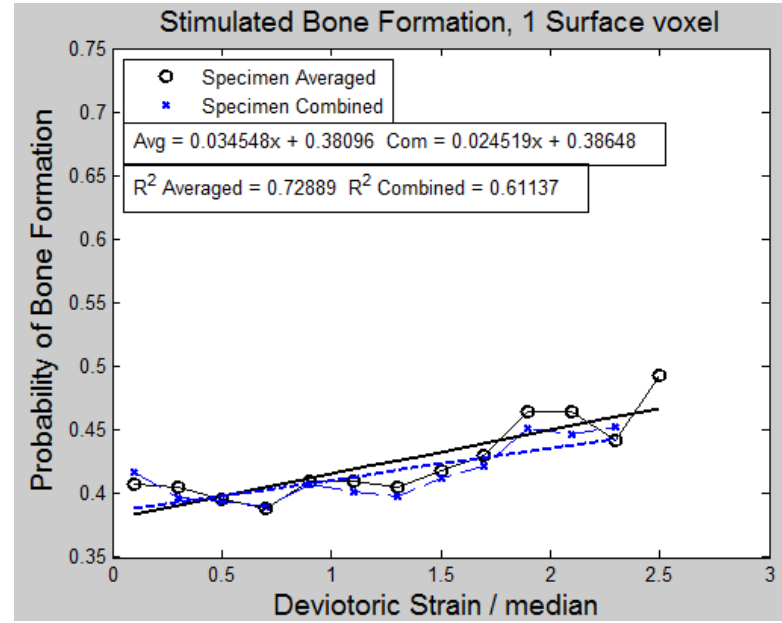
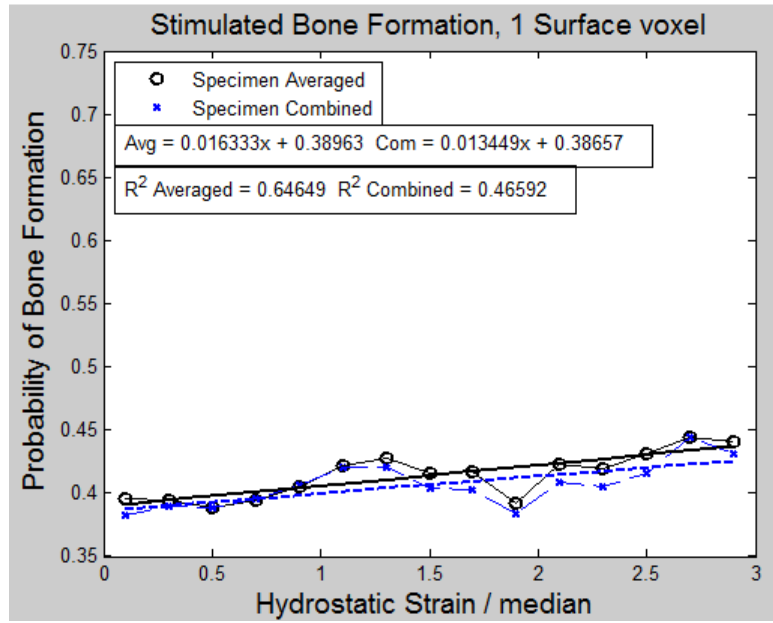
APPENDIX E: CHAPTER 3 ADDITIONAL DATA

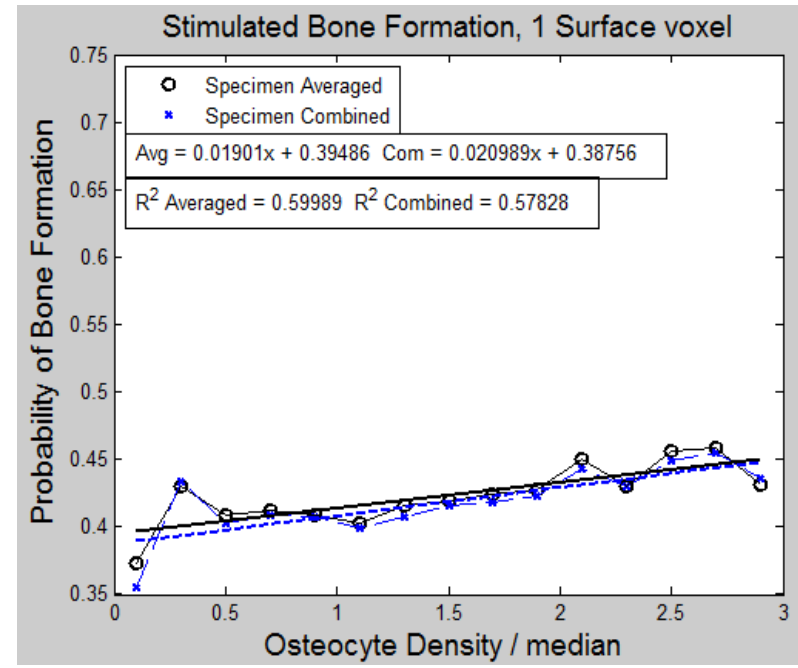
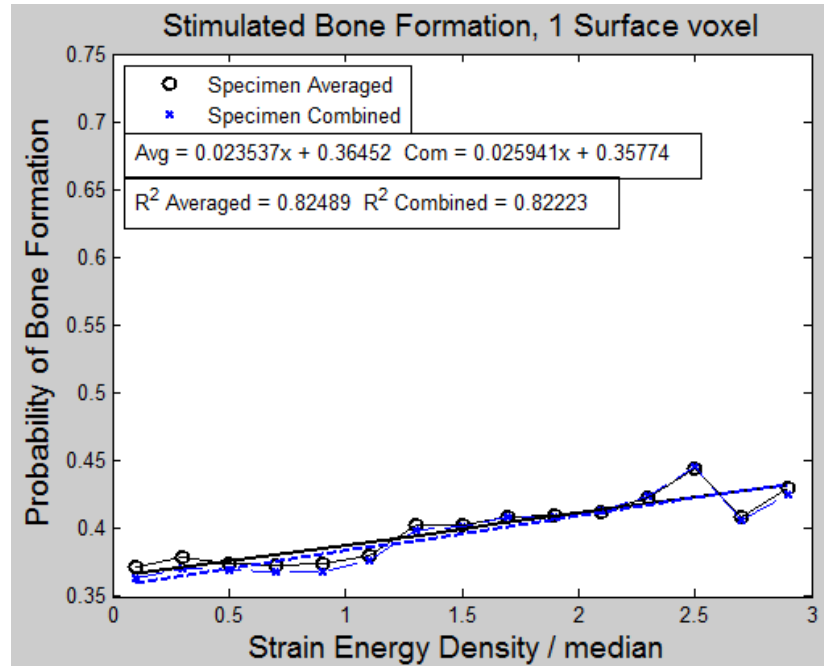
Group	Specimen ID #'	Mechanically Induced MS/BS	Background Bone Formation MS/BS	Pre-existing Bone Formation MS/BS	Mechanically Induced FV/BV	Background Bone Formation FV/BV	Pre-existing Bone Formation FV/BV	# of Mechanically Induced sites	# of Background Bone Formation sites	# of Pre-existing Bone Formation sites	BV/TV	BS/BV
Loaded	53	12.708	1.860	0.240	0.597	0.082	0.004	491	27	37	0.369	0.050
Loaded	54	11.951	2.984	0.705	0.610	0.144	0.007	337	33	30	0.374	0.048
Loaded	57	13.517	5.720	0.082	0.638	0.387	0.003	279	9	6	0.338	0.046
Loaded	58	8.275	0.865	0.379	0.499	0.078	0.007	265	9	34	0.400	0.039
Loaded	62	7.916	8.719	1.027	0.277	0.402	0.025	296	66	37	0.389	0.049
Loaded	65	12.239	0.264	0.345	0.535	0.008	0.008	337	11	25	0.404	0.044
Loaded	70	10.234	2.558	0.265	0.501	0.153	0.003	311	32	11	0.381	0.042
Loaded	71	9.681	2.073	0.265	0.541	0.113	0.010	348	31	45	0.376	0.046
	Mean	10.82	3.13	0.41	0.52	0.17	0.01	333.00	27.25	28.13	0.38	0.05
	STD	2.09	2.79	0.31	0.11	0.15	0.01	70.32	18.90	13.48	0.02	0.00
Control	55	2.789	1.929	0.599	0.136	0.080	0.010	148	10	25	0.325	0.039
Control	66	1.763	4.106	0.809	0.063	0.224	0.005	130	32	41	0.366	0.042
Control	69	2.699	5.025	1.370	0.133	0.383	0.030	123	21	47	0.278	0.045
Control	56	2.741	0.966	0.429	0.113	0.030	0.012	163	18	42	0.382	0.040
Control	59	0.993	3.445	3.310	0.055	0.189	0.093	151	35	121	0.370	0.051
Control	60	7.853	1.641	0.949	0.296	0.038	0.017	288	15	54	0.374	0.044
Control	63	3.608	4.706	2.990	0.152	0.193	0.044	160	28	71	0.263	0.048
Control	68	2.892	5.138	2.219	0.111	0.178	0.045	151	73	98	0.390	0.048
	Mean	3.17	3.37	1.58	0.13	0.16	0.03	164.25	29.00	62.38	0.34	0.04
	STD	2.05	1.65	1.12	0.07	0.12	0.03	51.86	19.73	32.42	0.05	0.00
Ratio of Average Loaded / Control		3.41	0.93	0.26	3.96	1.04	0.26	2.03	0.94	0.45	1.10	1.02
between Loaded and Control		<0.0001	0.84		<0.0001	0.92		<0.0001	0.8588	1.86	2.86	3.86

Table: Bone formation was classified as mechanically induced, background bone formation (existed prior to loading and continued after loading) and pre-existing bone formation (occurring only before loading).

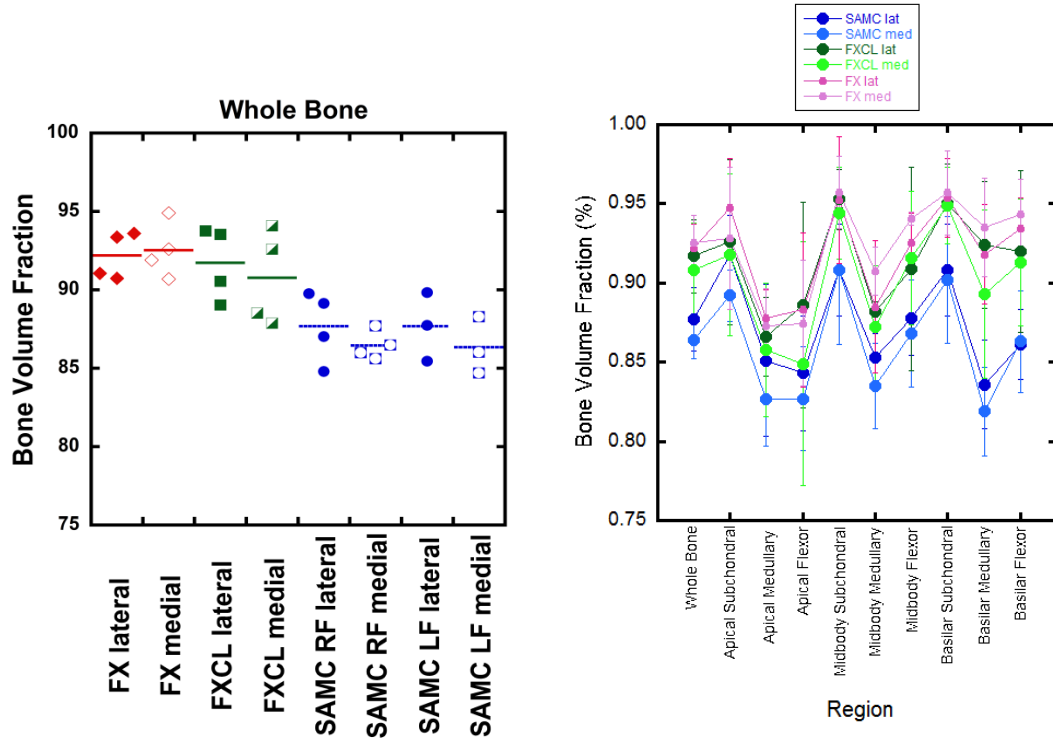
The probability of observing bone formation was calculated against several possible mechanical stimuli. SED had the highest R² values, however maximum shear strain had the largest slope.



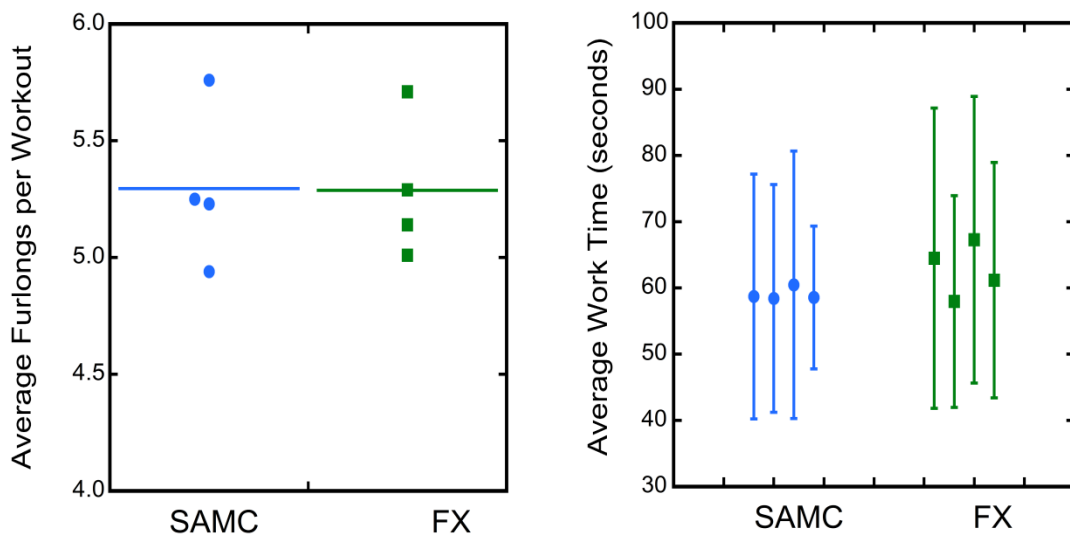




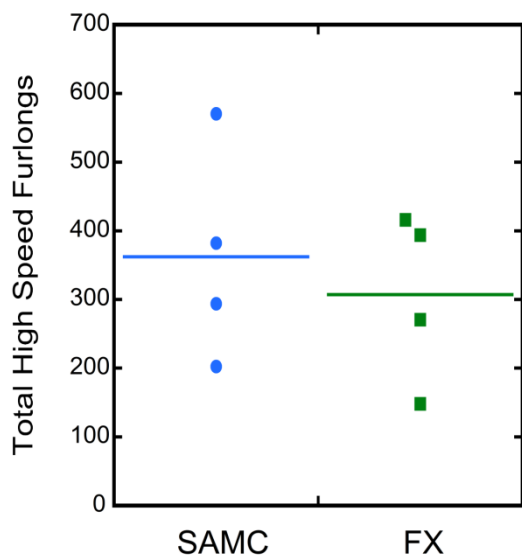
APPENDIX F: CHAPTER 4 ADDITIONAL DATA



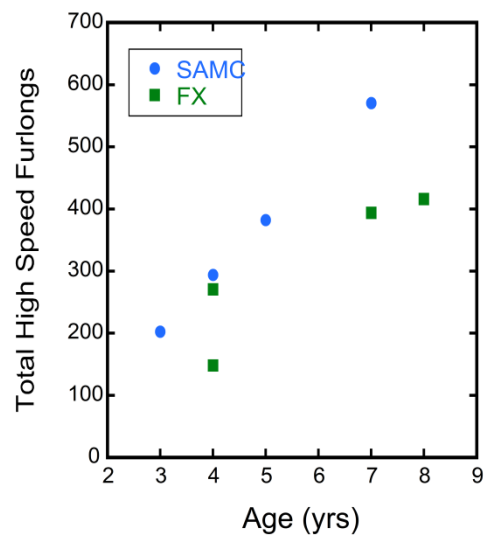
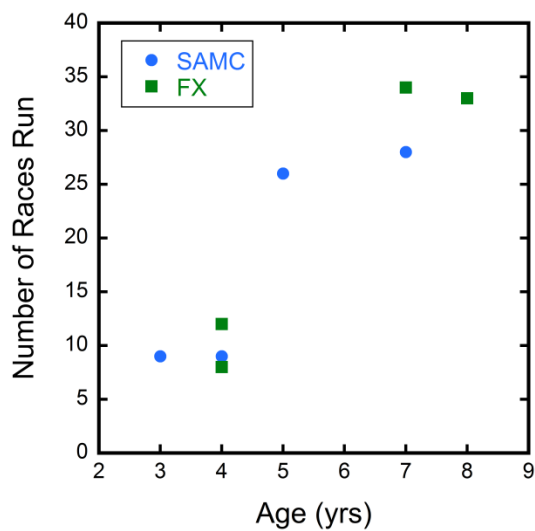
Bone volume fraction did not vary between the two front limbs per group.



The average distance and time per workout did not vary between groups.



There were no differences in total accrued high speed running distances between groups.



There were no differences in the total number of races run or the total distance run between fractured and control groups. Both the number of races and total distance run correlated to animal age.

